A MACHINING STABILITY MODEL WITH PROCESS DAMPING FOR HARD-TO-MACHINE MATERIALS

by

Christopher Tyler

A dissertation submitted to the faculty of
The University of North Carolina at Charlotte
in partial fulfillment of the requirements
for the degree of Doctor of Philosophy in
Mechanical Engineering

Charlotte

2015

Approved by:

_____
Dr. Tony Schmitz

_____
Dr. John Ziegert

_____
Dr. Peter Schmidt

_____
Dr. Abasifreke Ebong

ABSTRACT

CHRISTOPHER TYLER. A machining stability model with process damping for hard-to-machine materials. (Under the direction of DR. TONY SCHMITZ)

A substantial fraction of current machining research is directed towards increased productivity. A fundamental limitation is unstable vibration, or chatter, during cutting. Stability lobe diagrams, which relate the allowable chip width to spindle speed, may be used to select stable cutting conditions based on the system dynamics. However, at lower cutting speeds the stability limit asymptotically approaches a nearly constant chip width (using standard stability analyses) and variations in spindle speed do not have a significant effect. Thermal and hardness characteristics limit hard-to-machine metals, such as titanium and nickel alloys, to lower spindle speeds to avoid prohibitive tool wear. At these speeds, the allowable chip width can be larger due to an effect known as process damping.

This work develops an analytical stability model that includes process damping effects in turning and milling for single and multiple degree of freedom (DOF) dynamic systems. This model includes contributions from the system frequency response functions, as well as a process damping force normal to the cut surface, which is a function of the depth of cut, cutting speed, and an empirical process damping coefficient, *C*.

Stability testing was completed using a parallelogram, leaf-type flexure to identify the process damping behavior for low-speed single DOF milling. A representative database of process modeling coefficients was established for the workpiece materials: AISI 1018 steel, 6Al-4V titanium, 304 stainless steel, and Inconel 718. Two inserted cutting tools were used with relief angles of 11° and 15°; the rake and helix angles were zero for both

single-insert cutters. It was demonstrated that a reduction in the relief angle and an increase in flank wear on the cutting edge results in an increased process damping effect.

Multi-DOF (MDOF) systems for turning and milling were also modeled. Stability experiments were performed using a custom double-parallelogram notch-hinge flexure and a finned 6061-T6 aluminum workpiece for milling. Similarly, orthogonal stability testing was completed for turning using a custom parallelogram notch hinge flexible cutting tool. Tubular 6061-T6 aluminum workpieces were machined to validate the MDOF turning algorithm. The results indicate that the multiple degree of freedom model is able to predict a stability boundary that best represents the cutting test outcomes using a single process damping coefficient.

Finally, the versatility of the experimentally identified process damping coefficients was examined. To accomplish this, the coefficient identification for 6061-T6 aluminum using the single DOF parallelogram milling setup was first performed. Secondly, the same 11° relief angle milling insert was mounted to the MDOF turning flexure and the orthogonal turning tests were repeated on the same composition aluminum alloy.

The effects of changes in system dynamics on the process damping coefficient was observed to be minimal for a reduction of approximately 32% in the system's natural frequency. The process coefficients were similarly identified for much larger changes in dynamics, i.e., a 200-300% increase in the system's natural frequency. It was found that the identified process damping coefficients remained relatively consistent for the dynamic systems tested.

ACKNOWLEDGEMENTS

I would like to thank my academic advisor, Dr. Tony Schmitz, for mentoring me throughout my graduate experience and for allowing me the academic freedom to explore research areas of my own personal interest, for which I am extremely grateful.

I am very grateful to my committee members, Dr. John Ziegert, Dr. Peter Schmidt, and Dr. Abasifreke Ebong for their guidance and advice.

I would like to thank my colleagues at the Center for Precision Metrology (CPM) at the University of North Carolina at Charlotte and at the Machine Tool Research Center (MTRC) at the University of Florida for all the assistance.

I would like to thank my parents and friends for their continuous support and encouragement.

TABLE OF CONTENTS

LIST OF FIGURES ix

LIST OF TABLES xvii

CHAPTER 1: INTRODUCTION 1

1.1 Machining Stability 1

1.2 Hard-to-machine Materials 4

1.3 Process Damping 5

CHAPTER 2: LITERATURE REVIEW 10

CHAPTER 3: ANALYTICAL STABILITY ANALYSIS PART 1: TURNING 14

3.1 Linear Stability Analysis for Turning: An Overview 14

3.2 Stability Analysis Including Process Damping 18

3.2.1 Single DOF Turning 18

3.2.2 Single DOF Turning in Two Directions 22

3.2.3 Multiple DOF Turning in Two Directions 26

CHAPTER 4: ANALYTICAL STABILITY ALGORITHM PART 2: MILLING 33

4.1 Stability Analysis Including Process Damping 33

4.1.1 Single DOF Milling in Two Directions 36

4.1.2 Multi-Degree-of-Freedom Milling in Two Directions 42

CHAPTER 5: EXPERIMENTAL PROCEDURE 48

5.1 Specific Cutting Force Identification 48

5.1.1 Specific Cutting Force Identification for Turning 49

5.1.2 Specific Cutting Force Identification for Milling 51

5.2 Tool-Life Prediction and Modeling 53

5.3 Process Damping Coefficient Identification 56

5.3.1 Least RSS Method for Process Damping Coefficient Identification 57

5.3.2 Process Damping Coefficient Identification for Turning Setup 59

5.3.2.1 Vibration Measurements for Turning 62

5.3.2.2 Surface Roughness and Chip Morphology for Turning 65

5.3.3 Process Damping Coefficient Milling Setup 67

5.3.3.1 Single Degree of Freedom Experimental Setup 67

5.3.3.2 Multi-DOF Experimental Setup 74

CHAPTER 6: EXPERIMENTAL RESULTS AND DISCUSSION 76

6.1 Experimental Identification of the Process Coefficients for SDOF Milling 76

6.1.1 AISI 1018 Steel Process Coefficients for SDOF 77

6.1.1.1 AISI 1018 Steel Cutting Force Coefficients 77

6.1.1.2 AISI 1018 Steel Process Damping Coefficients 78

6.1.2 Creating a Process Coefficient Database 86

6.2 Experimental Identification of Process Coefficients in MDOF Milling 89

6.3 Experimental Identification of Process Coefficients in MDOF Turning 91

6.4 Process Damping Coefficient Versatility 93

CHAPTER 7: CONCLUSIONS & FUTURE WORK 101

7.1 Conclusions 101

7.2 Future Work 104

REFERENCES 106

APPENDIX A: ANALYTICAL SOLUTION FOR RADIAL IMMERSION PROCESS DAMPING 109

A.1: Radial Depth Analytical Solution. 109

A.2: Experimental Results for Radial Immersion Testing 113

A.3: Radial Immersion Tests Conclusions 122

APPENDIX B: SUPPLIMENTARY PROCESS DAMPING MODEL 123

LIST OF FIGURES

FIGURE 1.1:	Chip thickness variation resulting from vibrating flexible cutting tool, where $y(t-\tau)$ is the cut surface from the previous pass of the cutter, $y(t)$ is the cut surface from the current pass, and h_m is the commanded chip thickness.	2
FIGURE 1.2:	Significant chip thickness variation resulting from out of phase machining, where $y(t-\tau)$ is the cut surface from the previous pass of the cutter, $y(t)$ is the cut surface from the current pass, and h_m is the commanded chip thickness.	3
FIGURE 1.3:	Example stability lobe diagram using traditional linear analysis.	4
FIGURE 1.4:	Waves left on workpiece surface at elevated surface cutting speeds.	6
FIGURE 1.5:	Waves left on workpiece surface at lower surface cutting speeds have a shorter wavelength.	6
FIGURE 1.6:	Depiction of tool interfering short wavelength undulations imparted on workpiece surface, thought to be the underlying cause of process damping.	7
FIGURE 1.7:	The clearance angle varies with the instantaneous surface tangent as the cutter removes material on the sinusoidal surface.	8
FIGURE 1.8:	Stability lobe boundary including process damping effects.	8
FIGURE 3.1:	Control block diagram for a turning operation.	15
FIGURE 3.2:	Single degree of freedom turning model.	16
FIGURE 3.3:	Example stability lobe diagram. The stability boundary separates stable (chip width, spindle speed) pairs (denoted by 'o') and unstable pairs (denoted by '×').	17
FIGURE 3.4:	Stability diagram for the single DOF model from Figure 3.2, with no process damping.	21
FIGURE 3.5:	Convergence demonstration (N = 20 for 10 iterations) for the single degree-of-freedom model from Figure 3.2 with $\mathrm{C} = 6.11 \times 10^5 \mathrm{N/m}$.	22
FIGURE 3.6:	Stability diagram for the single degree-of-freedom turning model	22

from Figure 3.6 with $C = 6.11 \times 105\text{Nm}$.

FIGURE 3.7: Turning model with a single DOF in two orthogonal directions. 23

FIGURE 3.8: The analytical stability limit for turning model with a single DOF in two orthogonal directions. 27

FIGURE 3.9: Two DOF in two orthogonal directions turning model. 28

FIGURE 3.10: Analytical stability limit results for turning model with two DOF in two orthogonal directions. 32

FIGURE 4.1: Milling model for up/conventional milling. The vector *n* defines the average surface normal direction and *x* is the feed direction. 34

FIGURE 4.2: Milling model for down/climb milling. The vector *n* defines the average surface normal direction and *x* is the feed direction. 35

FIGURE 4.3: Analytical stability limit results for milling model with a single DOF in the *x* and *y* directions. 41

FIGURE 4.4: Analytical stability limit results for milling model with two DOF in the *x* and *y* directions. 47

FIGURE 5.1: Force measurement setup for turning experiments using the Kistler 9257B dynamometer. The tangential and normal forces are measured during the cutting of a cylindrical workpiece in an orthogonal cut. 51

FIGURE 5.2: Normal and tangential cutting forces measured during orthogonal test cut. 50

FIGURE 5.3: Cutting force measurement setup using a three component force dynamometer. 51

FIGURE 5.4: Example of cutting forces decoupled into *x* and *y*-directions for a 25% radial immersion test cut using a single-tooth endmill. 52

FIGURE 5.5: Linear regression results for mean *x* and *y* forces versus a range of feed per tooth values. 53

FIGURE 5.6: Sample measurements of the maximum FWW progression during wear tests. 54

FIGURE 5.7: Setup for interrupted FWW measurements. 54

FIGURE 5.8: Increase in FWW with cutting time at three spindle speeds for Ti 6Al-4V. 55

FIGURE 5.9: Taylor tool life model fit for Ti 6Al-4V. 56

FIGURE 5.10: Stability lobe validation for the single DOF milling (f_n = 228 Hz) milling setup. Stable cuts (o) and unstable cuts (×) are identified. 57

FIGURE 5.11: Description of variables for RSS estimate of process damping coefficient. 58

FIGURE 5.12: Sweep of process damping coefficients used to select final stability boundary 59

FIGURE 5.13: Experimental setup for turning stability tests. A cutting force dynamometer and accelerometer (not shown) were used to monitor the tool vibration during cutting. 60

FIGURE 5.14: Frequency response function of flexible cutting tool in tangential and feed directions. 61

FIGURE 5.15: Stability boundary for the multi-degree of freedom system with the grid of stable (o) and unstable (x) cutting tests identified. 62

FIGURE 5.16: Cutting force and accelerometer time domain signals in the feed direction for the stable point A {300 rpm, 3.0 mm} with corresponding frequency content below. 63

FIGURE 5.17: Cutting force and accelerometer time domain signals in the feed direction for the unstable point B {400 rpm, 3.0 mm}, with corresponding frequency content below. The chatter frequency is approximately 310 Hz. 64

FIGURE 5.18: Cutting force and accelerometer time domain signals in the feed direction for the unstable point B {1000 rpm, 2.0 mm} with corresponding frequency content below. The chatter frequency is approximately 1493 Hz. 65

FIGURE 5.19: Surface roughness and chip morphology of stable test cut. 66

FIGURE 5.20: Surface roughness and chip morphology of unstable test cut. 66

FIGURE 5.21: Single degree of freedom setup for milling stability tests and process damping coefficient identification. 68

FIGURE 5.22: Frequency response function comparison of single DOF flexure and 69

cutting tool in machine spindle (*x* and *y* directions were similar).

FIGURE 5.23: Time domain acceleration signal of a stable cut. 71

FIGURE 5.24: Frequency domain signal of a stable cut performed by a single-tooth cutter at 300 rpm (5 cps). 71

FIGURE 5.25: Time domain signal of an unstable cutting performance. 72

FIGURE 5.26: Frequency domain signal of an unstable cutting performance. Strong frequency content is observed at the flexure's 228 Hz natural frequency for the test completed at 700 rpm (11.7 cps). 72

FIGURE 5.27: Surface finish of workpiece after a stable cut. 73

FIGURE 5.28: Surface finish of workpiece after an unstable cut. 73

FIGURE 5.29: Experimental setup for two DOF milling stability tests. An accelerometer was used to monitor the flexure vibration during machining. 74

FIGURE 5.30: Frequency response function of flexible system in feed (*x*) and tangential (*y*) directions. 75

FIGURE 6.1: Stability lobe validation for the 228 Hz setup. Stable cuts (o) and unstable cuts (×) are identified. 79

FIGURE 6.2: Stability lobe validation for the 156 Hz setup. Stable cuts (o) and unstable cuts (×) are identified. 79

FIGURE 6.3: Up milling stability boundary for 50% radial immersion, 15° relief angle, low wear milling tests using the 228 Hz flexure setup ($C = 1.25\times10^5$ N/m). 80

FIGURE 6.4: Tool wear measurement of: a) new 15° relief angle insert; and b) moderately worn 11° insert. 81

FIGURE 6.5: Up milling stability boundary for 50% radial immersion, 15° relief angle, low wear milling tests using the 156 Hz flexure setup ($C = 1.30\times10^5$ N/m). 82

FIGURE 6.6: Up milling stability boundary for 50% radial immersion, 11° relief angle, low wear milling tests using the 228 Hz flexure setup ($C = 1.65\times10^5$ N/m). 82

FIGURE 6.7: Up milling stability boundary for 50% radial immersion, 11° relief 83

angle, low wear milling tests using the 156 Hz flexure setup (C = 1.65×10^5 N/m).

FIGURE 6.8: Comparison of analytical stability boundary for steel between the 15° relief angle process damping coefficient (C = 1.25×10^5 N/m - red) and the 11° relief angle process damping coefficient (C = 1.65×10^5 N/m - green). The blue stability boundary, C = 0.0×10^5 N/m, is used as a reference. 84

FIGURE 6.9: Up milling stability confidence region for 50% radial immersion, 11° relief angle milling tests using the 228 Hz flexure setup with an unworn cutting edge (C = $(1.60 \pm 0.15)\times10^5$ N/m). 85

FIGURE 6.10: Stability boundary comparison for Inconel 718 for the low insert wear conditions. 87

FIGURE 6.11: Stability boundary for the MDOF system. Stable (o) and unstable (x) experiments are identified. 89

FIGURE 6.12: Accelerometer measurements of stable cut at 1000 rpm, b = 7.0 mm. 90

FIGURE 6.13: Accelerometer measurements of unstable cut at 1800 rpm, b = 7.0 mm. 91

FIGURE 6.14: Stability boundary for the MDOF system with the grid of stable (o) and unstable (x) cutting tests identified (C = 2.6×10^5 N/m) for aluminum. 92

FIGURE 6.15: SDOF parallelogram leaf-type flexure for orthogaonal stability testing with 6061-T6 aluminum finned workpieces. 94

FIGURE 6.16: Accelerometer time domain signals of stable (top-left) and unstable (bottom-left) cutting parameters and the accompanied frequency domain stable (top-right) and unstable (bottom-right) signals. 95

FIGURE 6.17: Grid of stable ('o'), unstable ('x'), and marginally stable ('square') test points with the final stability boundary corresponding to C = 1.80×10^5 N/m. 95

FIGURE 6.18: SDOF milling setup with system's natural frequency approximately f_n = 815 Hz. A schematic of the flexure is shown in the top-right of the image. 96

FIGURE 6.19: Accelerometer time domain signals of stable (top-left) and unstable (bottom-left) cutting parameters and the accompanied frequency domain stable (top-right) and unstable (bottom-right) signals for the 97

f_n = 815 Hz system.

FIGURE 6.20 Grid of stable ('o') and unstable ('x') test points with the final stability boundary corresponding to C = 1.70×10^5 N/m. 97

FIGURE 6.21: 11 degree milling insert mounted to MDOF flexible turning tool for orthogonal stability tests. 98

FIGURE 6.22: Grid of stable ('o') and unstable ('x') test points with the final stability boundary corresponding to C = 1.70×10^5 N/m for turning tests with 11° relief angle insert. 100

FIGURE A.1: Limiting axial depth of cut versus spindle speed for a 25% radial immersion. 111

FIGURE A.2: Axial depth stability limit for a 25% radial immersion. 111

FIGURE A.3: Axial depth stability limit for a 25% radial immersion with the *b* = 3 mm spindle speeds identified (circles). 112

FIGURE A.4: Axial depth stability limit for a 50% radial immersion with the *b* = 3 mm spindle speeds identified (circles). 112

FIGURE A.5: Limiting radial depth of cut, a_{lim}, versus spindle speed for an axial depth of 3 mm. 113

FIGURE A.6: Limiting radial depth of cut versus spindle speed for an axial depth of 5 mm. 113

FIGURE A.7: Photograph of milling setup. The test coupon was bolted to the flexure. An accelerometer was used to measure the vibration during *x*-direction cutting and identify stable and unstable conditions. 114

FIGURE A.8: Images of surfaces for unstable (left) and stable (right) cutting conditions. 115

FIGURE A.9: Limiting radial depth of cut versus spindle speed for the flexure setup with a 3 mm axial depth. 116

FIGURE A.10: Frequency content for a stable cut at a spindle speed of 3600 rpm, a radial depth of 5 mm, and an axial depth of 3 mm. 117

FIGURE A.11: Frequency content for an unstable cut at a spindle speed of 2675 rpm, a radial depth of 4 mm, and an axial depth of 3 mm. 117

FIGURE A.12: Frequency content for a stable cut at a spindle speed of 300 rpm, a radial depth of 10 mm, and an axial depth of 3 mm. 118

FIGURE A.13: Frequency content for an unstable cut at a spindle speed of 500 rpm, a radial depth of 10 mm, and an axial depth of 3 mm. Note the change in vertical scale relative to Figures A.10-A.12. 118

FIGURE A.14: Limiting radial depth of cut versus spindle speed for the flexure setup with a 5 mm axial depth. 119

FIGURE A.15: Frequency content for a stable cut at a spindle speed of 3500 rpm, a radial depth of 3 mm, and an axial depth of 5 mm. 120

FIGURE A.16: Frequency content for an unstable cut at a spindle speed of 3250 rpm, a radial depth of 3 mm, and an axial depth of 3 mm. 120

FIGURE A.17: Frequency content for a stable cut at a spindle speed of 300 rpm, a radial depth of 6 mm, and an axial depth of 5 mm. 121

FIGURE A.18: Frequency content for an unstable cut at a spindle speed of 500 rpm, a radial depth of 6 mm, and an axial depth of 5 mm. Note the change in vertical scale relative to Figs. A.15-A.17. 121

FIGURE B.1: Stability boundary for 50% radial immersion, 15° relief angle, low wear up milling tests in 1018 steel (C = 1.3×10^5 N/m) with multiplier, Λ ($\lambda = 2.2\times10^{-3}$ m). 124

FIGURE B.2: Change in λ as a function of modal stiffness, k. 126

FIGURE B.3: Trend in λ as a function of natural frequency f_n. 127

FIGURE B.4: Initial Stability boundary for 50% radial immersion, milling for 1018 steel (C = 1.3×10^5 N/m) with multiplier, Λ ($\lambda = 5.00\times10^{-3}$ m) and f_n = 100 Hz. 128

FIGURE B.5: Final Stability boundary for 50% radial immersion, milling for 1018 steel (C = 1.3×10^5 N/m) with multiplier, Λ ($\lambda = 0.57\times10^{-3}$ m) and fn = 900 Hz. 128

FIGURE B.6: Low cutting speed process damping effects with varying system natural frequency for mild steel, Tlusty [2]. 129

FIGURE B.7: Augmented stability boundary b_{lim} (mm) versus V (m/min) for f_n = 100, 200, 500, and 1000 Hz. 130

FIGURE B.8: Trend in λ as a function of damping ratio, ζ. 131

LIST OF TABLES

TABLE 5.1:	Modal parameters for flexible cutting tool setup	61
TABLE 5.2:	Modal parameters for single DOF flexure with and without mass.	70
TABLE 5.3:	Modal parameters for two DOF flexible workpiece setup.	75
TABLE 6.1:	Cutting force parameters for the 18.54 mm diameter -15° relief cutter with low insert wear (FWW <100 μm).	77
TABLE 6.2:	Cutting force parameters for the 19.05mm diameter -11° relief cutter with low insert wear (FWW <100 μm).	78
TABLE 6.3:	Comparison of process damping coefficients for low insert wear tests (FWW < 100 μm).	83
TABLE 6.4:	Comparison of process damping coefficients for moderate wear tests (150 μm < FWW < 250 μm).	85
TABLE 6.5:	Process damping coefficients for the 11° relief angle tool geometry.	87
TABLE 6.6:	Process damping coefficients for the 15° relief angle tool geometry.	87
TABLE 6.7:	Specific cutting force coefficients for the 11° relief angle tool geometry.	88
TABLE 6.8:	Comparison of process coefficients for the 15° relief angle tool geometry.	88
TABLE 6.9:	Taylor tool-life model parameters.	89
TABLE 6.10:	Feed direction modal parameters for 7° and 11° relief angle setups.	99
TABLE B.1:	Process damping parameters, λ, for the 11° relief angle tool geometry.	125
TABLE B.2:	Process damping parameters, λ, for the 15° relief angle tool geometry.	125
TABLE B. 3:	Process parameters for determining process damping parameter, λ, sensitivity.	125
TABLE B.4:	Range of modal parameters for λ sensitivity study.	126

CHAPTER 1: INTRODUCTION

1.1 Machining Stability

Subtractive processes such as milling and turning play a significant role in modern discrete part production. The desire to produce parts accurately and efficiently has increased with part complexity. Since its development in the late 1960s, the computer numerically-controlled (CNC) machine has facilitated this increase in complexity. However, productivity in machining processes is often limited by self-exited vibrations between the cutting tool and workpiece, referred to as chatter. These self-excited vibrations arise due to the regeneration of surface waviness that occurs as the tool removes the chip of commanded thickness, h_m, from the surface, $y(t)$, that was created during the previous pass, $y(t-\tau)$, where τ is the time for one revolution; see Figure 1.1. In turning operations, this is developed after successive rotations of the workpiece. In milling, a rotating cutter is moved relative to the workpiece in order to remove material, so the delay is between teeth.

Prior to research in the 1950s and 60s, the primary chatter mechanisms were unknown. Pioneering research led by Tobias, Tlusty, and Merritt [1-3] established that stability of the cutting process depended on the relative stiffness and damping between the tool and workpiece. They realized that the phase between undulations left on the workpiece surface after each pass of the cutting tool dictated the stability.

Figure 1.1 illustrates the case where the wavy surfaces between two passes of the cutting tool are in phase. While vibration is still present for this in-phase condition, the chip thickness variation is small, leading to a stable cutting operation. Understanding the structural dynamics of the system allows for this in-phase condition to be selected and enables stable cutting at much larger chip widths. Figure 1.2, presents the condition when the wavy surfaces are out of phase. This leads to much larger variation in chip thickness and, subsequently, cutting forces.

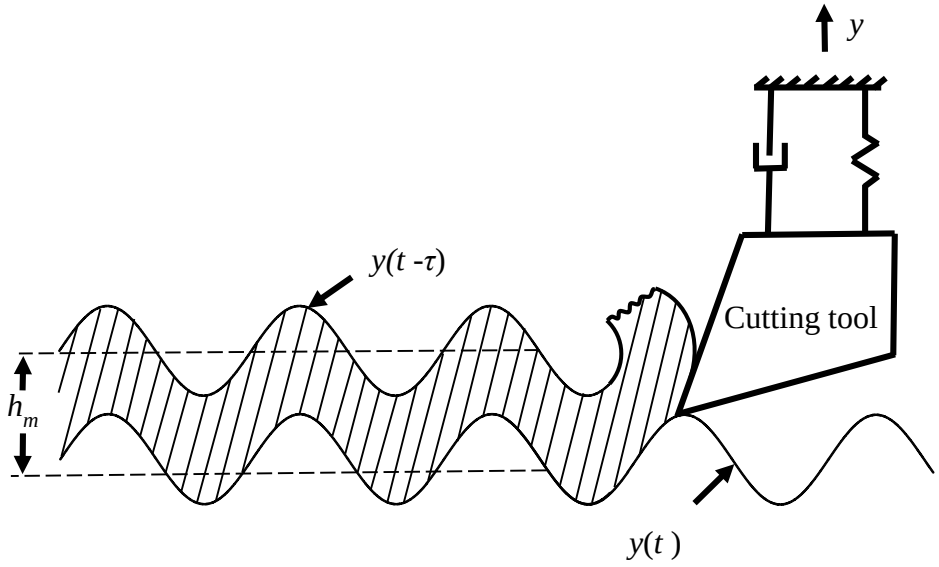

Figure 1.1: Chip thickness variation resulting from vibrating flexible cutting tool, where $y(t-\tau)$ is the cut surface from the previous pass of the cutter, $y(t)$ is the cut surface from the current pass, and h_m is the commanded chip thickness.

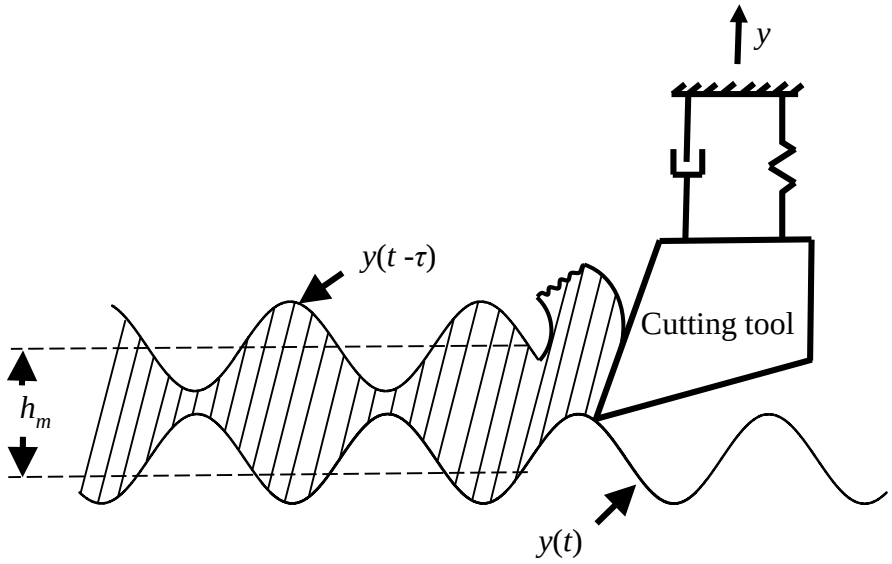

Figure 1.2: Significant chip thickness variation resulting from out of phase machining, where $y(t-\tau)$ is the cut surface from the previous pass of the cutter, $y(t)$ is the cut surface from the current pass, and h_m is the commanded chip thickness.

The work by Tobias, Tlusty, and Merritt [1-3] helped to develop an analytical model to estimate stability based on the natural vibratory modes of the cutting tool with respect to the direction of the cutting force. This, in turn, led to several effective methods for predicting chatter, including the stability lobe diagram. The stability lobe diagram offers a predictive capability for selecting stable chip width-spindle speed combinations in machining operations. These diagrams require knowledge of the system dynamics (in the form of the system's frequency response function, or FRF) and the process (cutting force coefficients, radial immersion, and geometric tool specifications). These diagrams depict regions of stable cutting with respect to spindle speed and chip width. Stable and unstable zones are segregated by a stability boundary as illustrated in Figure 1.3.

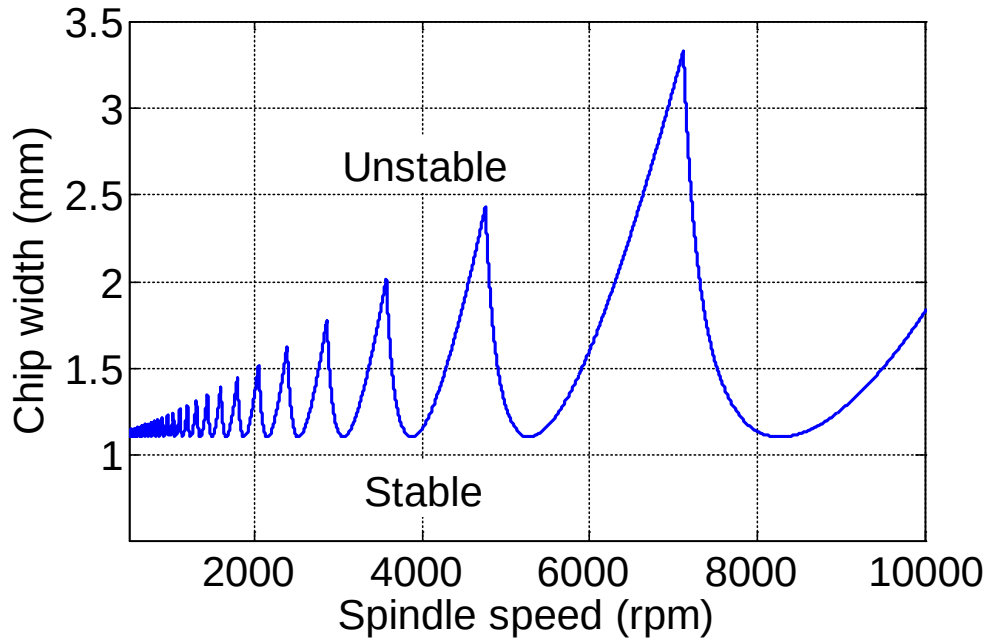

Figure 1.3: Example stability lobe diagram using traditional linear analysis.

1.2 Hard-to-machine Materials

At high spindle speeds, more efficient cutting is possible. Consequently, the popularity of aluminum alloys in the aerospace industry has shifted much of the machining dynamics research in the high speed machining direction, where tool wear resulting from high surface speeds is less of a concern. Recently, that focus has shifted to lower spindle speed regions because hard-to-machine materials cannot take advantage of higher speed stability zones due to prohibitive tool wear.

For example, nickel-based super alloys serve as important materials in the aerospace, gas turbine, and nuclear industries. These alloys are highly regarded for superior corrosion, creep, and thermal fatigue resistance. In particular, Inconel 718 is widely used within the combustion regions of gas turbines where temperatures exceed 1100ºC for several thousand hours. It derives its unique mechanical properties from a high composition

percentage of solid-solution elements including: Ni-55%, Cr-21%, Fe-18%, and Mo-3%. The desired mechanical properties also contribute to its poor machinability. The characteristics of its machinability can be summarized as follows [4-8]:

- rapid work hardening during machining operations
- abrasive tool wear due to carbides within the material
- poor thermal conductivity/diffusivity causes heat to remain at the cutting tool tip which yields high cutting edge temperatures
- excessive diffusive wear due to high cutting edge temperatures and chemical interactions
- chip adhesion that leads to notch wear and/or chipping along the cutting edge.

Other materials, such as titanium, stainless steels, and other high carbon steel alloys are also now commonly used in the medical, defense, and energy manufacturing sectors. However, achieving high material removal rates with acceptable tool life is challenging. To address the challenges associated with the machining these types of materials, companies invest in expensive tooling centers that are extremely stiff and equipped with elaborate cooling systems in order to meet production requirements.

1.3 Process Damping

In order to maintain productivity and prevent excessive tool wear, hard-to-machine materials must be processed at low spindle (surface) speeds that reside in what is referred to as the process damping regime. As the tool vibrates during cutting, there are several waves that are left on surface of the workpiece due to this vibration. A cutting process operating at a high surface speed imparts a long wavelength vibration as illustrated in Figure 1.4.

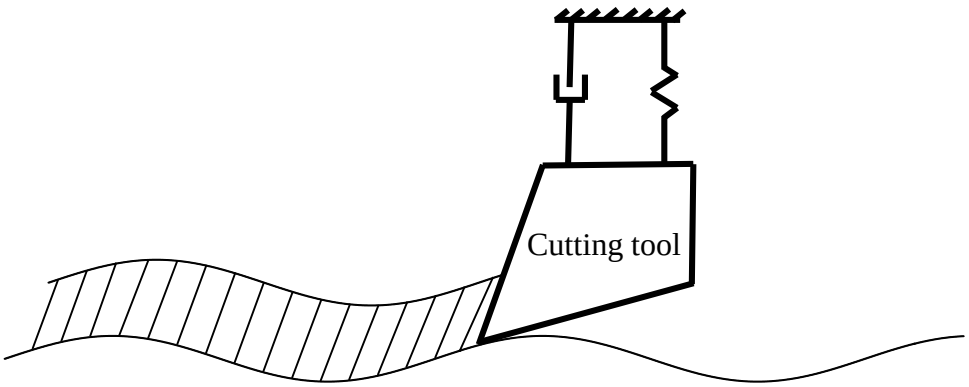

Figure 1.4: Waves left on workpiece surface at elevated surface cutting speeds.

If the flexible tool vibrates at the same frequency and the cutting speed is reduced, the frequency of wave generation remains unchanged. However, the wavelength left on the surface of the workpiece reduces. Process damping is a phenomenon that is thought to occur when there is interference between the cutting tool's flank, or relief, face and the undulations left behind on the cut surface, as depicted in Figure 1.6.

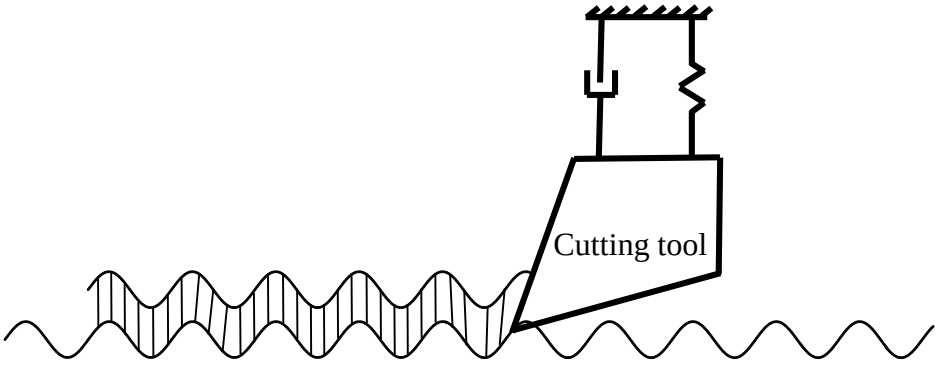

Figure 1.5: Waves left on workpiece surface at lower surface cutting speeds have a shorter wavelength.

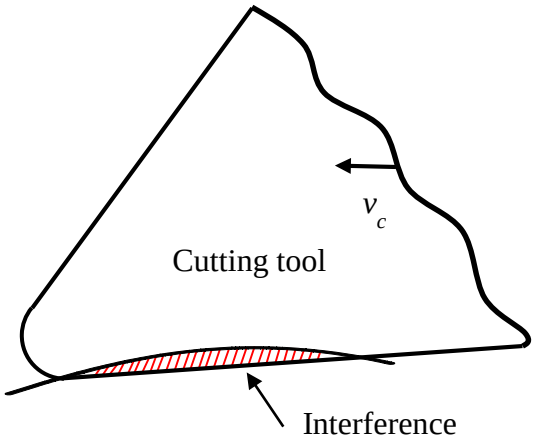

Figure 1.6: Depiction of tool interfering short wavelength undulations imparted on workpiece surface, thought to be the underlying cause of process damping.

The interaction between the flank of the cutting tool and the wavy surface serves as an energy dissipation, or damping, mechanism and has been observed to increase the process stability. The result is the ability to cut at much higher chip widths at low spindle speeds. This increases the material removal rate which is otherwise low due to the low cutting speeds required to limit tool wear.

To further describe the mechanism for process damping, consider the tool tip moving along a wavy surface while shearing away the chip; see Figure 1.7. Four locations are identified: 1) the clearance angle, γ, between the flank face and the work surface tangent is equal to the nominal relief angle of the tool; 2) there is a greater potential for the tool/surface interference; 3) the relief angle returns to the original nominal value; and 4) γ is significantly larger than the nominal value.

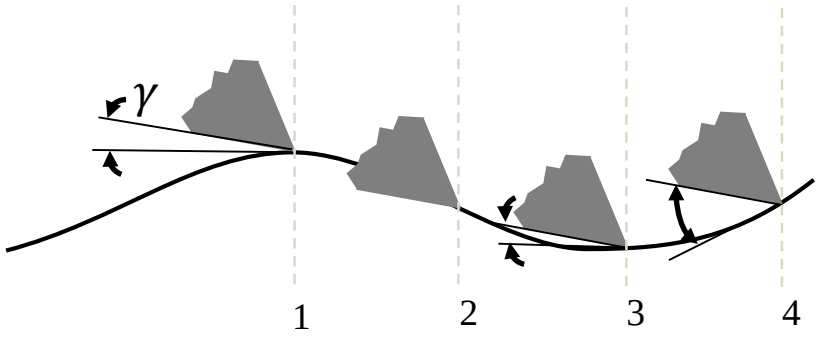

Figure 1.7: The clearance angle varies with the instantaneous surface tangent as the cutter removes material on the sinusoidal surface.

The damping effect is larger for the shorter vibration wavelengths because the slope of the sinusoidal surface increased and, subsequently the variation in clearance angle increases. Therefore, lower cutting speeds or higher vibrating frequencies give shorter wavelengths and, consequently, increase process damping. The result is a transformation of the traditional, linear stability lobes to stability lobes that include a process damping regime; see Figure 1.8.

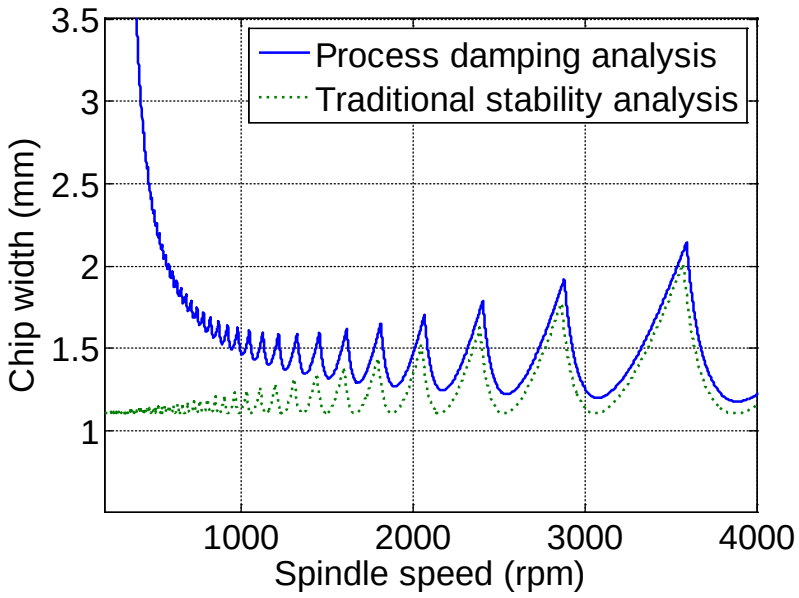

Figure 1.8: Stability lobe boundary including process damping effects.

Identifying and verifying a model that can predict these process damping conditions is becoming more important in today's manufacturing industry. This research provides an analytical solution for machining stability that includes process damping effects for single and multiple degree of freedom (DOF) dynamic systems. A velocity-dependent process damping force model, which relies on a single process damping coefficient, the cutting depth, the cutter velocity, and the cutting speed, is applied here. The intent of this study is to establish a machining model database for hard-to-machine materials. Included in the proposed database is cutting force coefficients, tool life parameters, and the process damping coefficients, all of which provide valuable information for parameter selection in a modern industrial setting. The materials that are considered include: AISI 1018 steel, Ti 6Al-4V, AISI 304 stainless steel, Inconel 718, and 6061-T6 aluminum.

CHAPTER 2: LITERATURE REVIEW

Process damping can be described as the energy dissipation due to relative velocity and interference between the relief angle of a cutting tool and the existing vibrations on the machined workpiece surface. Modeling the process damping mechanism in metal cutting has been the subject of many research efforts, especially as the use of exotic hard-to-machine materials has increased. This chapter summarizes prior process damping research.

Many researchers have investigated process damping in turning and milling operations. Underestimations in stability behavior at low cutting velocities motivated early studies by Sisson and Kegg [9], Wallace and Andrew [10] and Tlusty and Ismail [11]. In their studies, they established that contact between the cutter flank and the vibrations imprinted on the machined surface influenced the dynamic cutting forces and lead to “process damping”. Tlusty and Ismail [11] concluded that the stability increase with a reduction in cutting speed is largely due to process damping. In their 1978 CIRP keynote, Tlusty et al. [12] discussed the direct influence of tool geometry, work material, and cutting speed on the dynamic cutting force coefficients at process damping cutting speeds. The important factors described in these investigations provided the basis for subsequent process damping models.

Process damping is particularly important for hard-to-machine materials, such as titanium, nickel super alloys, and hardened steels. For this reason, more recent efforts have been made to analytically predict process damping behavior. In his 1989 publication, Wu [13] developed a model in which plowing forces present during the tool-workpiece contact are assumed to be proportional to the volume of interference between the flank of the cutter and the undulations existing on the workpiece. Several others later utilized this method of estimating process damping forces by calculating the volume of material displaced by the cutter. Tarng et al. [14] expanded the indentation model to more efficiently calculate process damping forces using feedforward neural networks. In their proposed model, they analyzed the stability in turning processes using different relief and rake angles to identify the stability boundary. Elbestawi et al. [15] modified Wu's indentation model for milling. An important aspect of this study was the ability to simulate the increase in stability limit due to tool wear effects at process damping speeds.

In 1994, the tool wear stabilizing effect in turning processes was observed by Chiou and Liang [16,17]. Here, a first-order Fourier transform representation of the interference between the tool and workpiece was developed to model the nonlinear process as linear. Analytical stability lobe diagrams were generated using the linear approximation and qualitative agreement was observed in turning experiments at several levels of flank wear.

Altintas et al. [18] also provided a method for identifying the dynamic cutting force coefficients and stability at low cutting velocities in turning. In a series of cutting tests, a fast tool servo was used to modulate the cutting tool at the desired frequencies and amplitudes. This removed the regenerative aspect of orthogonal cutting and isolated the

process damping effect. This study also considered the effects of tool wear on the process coefficients and illustrated the influence on stability at low cutting speeds.

Continuing in their study of process damping in machining, Altintas et al. [19] extended their prior research to include milling at low cutting velocities. By modeling process damping as a linear function of the velocity and modeling both rotating and fixed structures present in the cutting process, they produced the stability boundary for the process damping regime. Using Wu's indentation method to obtain the process damping coefficients, they were able to compare simulations against a series of slot milling experiments. They observed stability dependence both on cutting speed and symmetry in the rotating system's structural dynamics.

Huang and Wang [20] showed that the plowing force (more than the shear force) was the dominant contributor in process damping for peripheral milling operations. In this study, the effects of cutting conditions (cutting speed, feed, axial and radial depths of cut) on process damping were examined. Separating the process damping force into shearing and plowing components enabled them to identify that plowing was the dominant element in process damping.

Budak and Tunc [21] used an energy-based method to identify the process damping force coefficient and reinforced the concept that decreasing the relief angle increases the process damping effect for milling and turning processes. They found that the hone radius could cause a process damping effect at higher cutting speeds in orthogonal cutting. The proposed method was verified by time domain simulation and experiments.

In a follow-up study, Budak and Tunc [22] extended their model to include additional effects of cutting conditions and tool geometry on process damping. In this paper, they

observed a slight increase in process damping when using a cylindrical flank face as compared to a planar flank geometry.

Sims and Turner [23] developed a time domain model in milling operations that included non-linear process damping effects. Their method calculated: 1) the current tooth position, 2) the instantaneous chip thickness based on the tooth position, and 3) the forces that arise due to the flank-wave interference. Generated data revealed a strong connection between the feed rate of the cutter and the process damping wavelength. Their observation was that higher feed per tooth values correspond to lower out-of-phase forces. Experimental comparison with time domain simulation suggested further calibration of the model parameters was required either through experimentation or detailed chip formation modeling.

Turner et al. [24] experimentally assessed the role of geometric cutter parameters in process damping. Cutting tests performed on a flexure were used to evaluate the process damping influence of edge geometry, relief angle, rake angle, and variable helix/pitch angle on milling operations. The flexible workpiece study revealed a significant performance increase using variable helix/pitch cutters and tools with increased edge radius. To a lesser extent, low relief angle/low rake angle combinations also increased the process damping performance.

CHAPTER 3: ANALYTICAL STABILITY ANALYSIS PART 1: TURNING

In this chapter, an iterative, analytical stability analysis that incorporates effects of process damping is described. An overview of the traditional stability analysis is first presented followed by a detailed description of the new analysis that includes process damping. The dynamic model is used to describe single and MDOF turning.

3.1 Linear Stability Analysis for Turning: An Overview

Frequency-domain solutions for machining stability are well established and have been applied for many years. Efforts initiated by Tobias, Tlusty, and Merritt [1-3] identified regenerative chatter as a mechanism influenced largely by the cutting system's dynamic response. The frequency response function (FRF) of the cutting system was mapped to create stability lobe diagrams that display chip width versus spindle speed to identify stable and unstable cutting regions.

In descriptions of regenerative chatter in machining, the instantaneous cutting force, F_c, is typically written as:

$$F_c = K_s b h(t) \tag{1}$$

where K_s is the specific cutting force (which depends on the tool-workpiece combination and, to a lesser extent, the cutting parameters), b is the chip width, and $h(t)$ is the time-dependent instantaneous chip thickness:

$$h(t) = h_m + y(t-\tau) - y(t). \tag{2}$$

Referring back to Figure 1.1, the constant portion of the force containing the mean, or commanded, chip thickness, h_m, does not influence the stability of the operation. The feedback between the current vibration, $y(t)$, and the time-delayed vibration from the previous revolution, $y(t-\tau)$, is the mechanism that leads to self-excited vibration, where τ is the time for one revolution. The control feedback block diagram for a turning operation is presented in Figure 3.1, where G_{or} is the oriented frequency response function (described later) and the remaining terms are described in Eqs. 1 and 2.

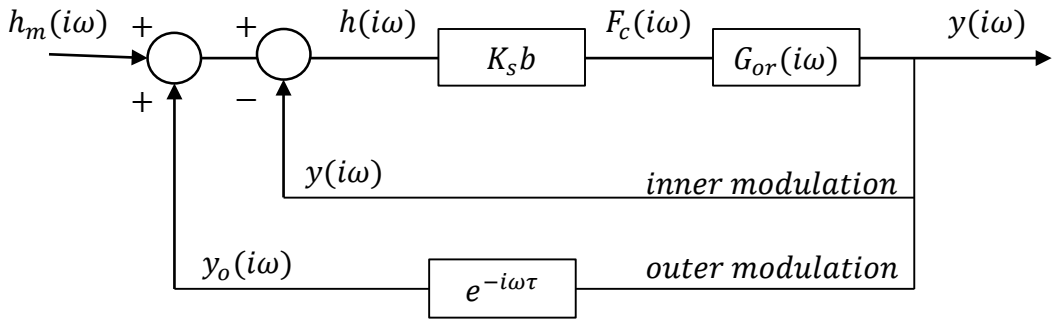

Figure 3.1: Control block diagram for a turning operation.

To describe the stability algorithm, consider the single DOF turning model displayed in Figure 3.2. Tlusty [2] defined the limiting stable chip width, b_{lim}, for regenerative chatter using:

$$b_{\lim} = \frac{-1}{2K_s \operatorname{Re}\left(G_{or}\right)}, \tag{3}$$

where $G_{or} = \cos(\beta - \alpha)\cos(\alpha)\, G_u$. In this expression, β is the force angle relative to the surface normal, α is the angle between the *u* direction and the surface normal, and G_u is the frequency response function in the *u* direction, which can be described using the modal mass, *m*, modal stiffness, *k*, and modal (viscous) damping, *c*.

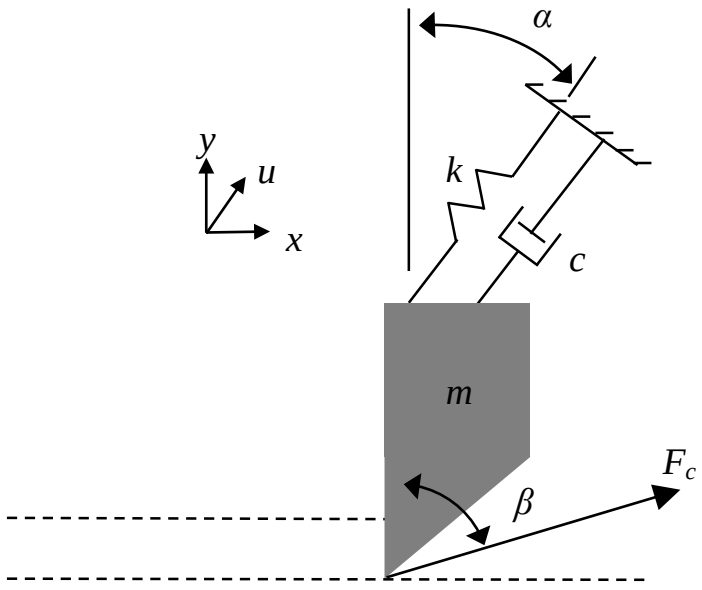

Figure 3.2: Single degree of freedom turning model.

The expression relating the spindle speed, Ω, to the phase, ε, is given as:

$$\frac{f_c}{\Omega} = N + \frac{\varepsilon}{2\pi}, \tag{4}$$

where $N = 0,1,2,\ldots$ is the integer number of vibration waves left on the workpiece surface per revolution, f_c is the chatter frequency (from the negative real portion of G_{or}), and ε is the relative phase between the current and the time-delayed vibration; see Eq (5). Here, Re denotes the real part and Im the imaginary part of the oriented frequency response function.

$$\varepsilon = 2\pi - 2\tan^{-1}\left(\frac{\mathrm{Re}(G_{or})}{\mathrm{Im}(G_{or})}\right) \quad \text{(rad)} \tag{5}$$

Figure 3.3 presents an example stability lobe diagram where the curves generated from the governing equations separate the region into stable and unstable chip width-spindle speed combinations.

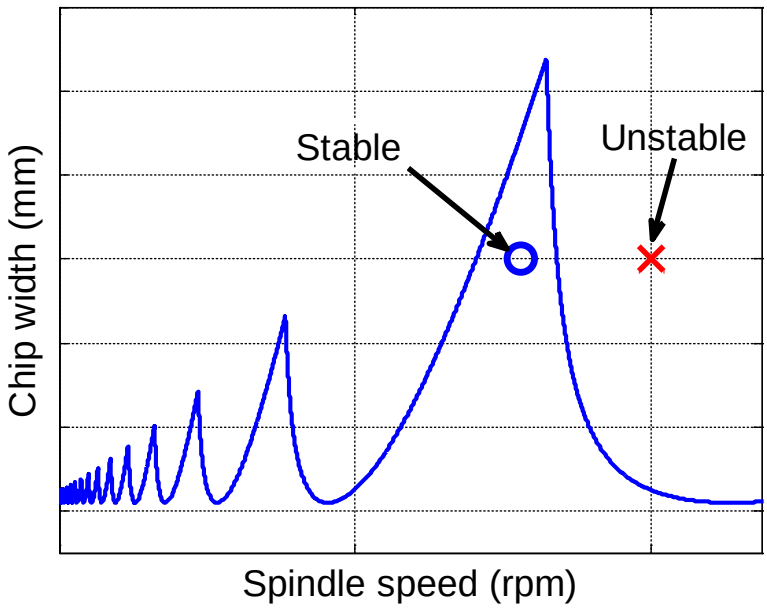

Figure 3.3: Example stability lobe diagram. The stability boundary separates stable (chip width, spindle speed) pairs (denoted by 'o') and unstable pairs (denoted by '×').

3.2 Stability Analysis Including Process Damping

From Figure 3.3, the chatter-free depths of cut are observed to diminish substantially at low spindle speeds, where the stability lobes become more closely spaced. Fortunately, the process damping effect can serve to increase the allowable chip width for low spindle speeds. The process damping force, F_d, is characterized as a 90º ($\pi/2\ rad$) phase shift relative to the displacement and opposite in sign from the velocity. Given the preceding description, the process damping force is modeled as the viscous damping force shown in Eq. 6.

$$F_d = -C\frac{b}{V}\dot{y} \tag{6}$$

Here, the process damping force in the *y* direction (perpendicular to the cut surface) is expressed as a function of the cutter velocity, $\dot{y}$, chip width, *b*, cutting speed, *V*, and process damping coefficient, *C*. The following sections demonstrate how an analytical stability solution is derived for both milling and turning applications with the inclusion of the process damping force.

3.2.1 Single DOF Turning

Consider the single DOF system presented in Figure 3.2. To incorporate the process damping force into the stability analysis, it is first projected in the *u* direction:

$$F_u = F_d\cos(\alpha) = -C\frac{b}{V}\dot{y}\cos(\alpha) = -\left(C\frac{b}{V}\cos(\alpha)\right)\dot{y}. \tag{7}$$

The final form of the *u* projection of the process damping force is effectively a viscous damping term. Therefore, the force can be incorporated in the traditional regenerative chatter stability analysis by modifying the structural damping in G_u. As illustrated in Figure

3.2, the single degree of freedom, lumped-parameter dynamic model can be described using the modal mass, *m*, modal viscous damping coefficient, *c*, and modal spring stiffness, *k*. In the absence of process damping, the time domain equation of motion in the *u* direction is:

$$m\ddot{u} + c\dot{u} + ku = F_c \cos(\beta - \alpha). \tag{8}$$

In this equation, one overdot indicates one time derivative (velocity) and two overdots indicate two time derivatives (acceleration). The corresponding FRF in the *u* direction is:

$$G_u = \frac{U}{F_c \cos(\beta - \alpha)} = \frac{1}{-m\omega^2 + ic\omega + k}, \tag{9}$$

where ω is the excitation frequency (rad/s). When process damping is included, however, the equation becomes:

$$m\ddot{u} + c\dot{u} + ku = F_c \cos(\beta - \alpha) - \left(C\frac{b}{V}\cos(\alpha) \right)\dot{y}. \tag{10}$$

Replacing $\dot{y}$ in Eq. (10 with $\cos(\alpha)\,\dot{u}$ gives:

$$m\ddot{u} + c\dot{u} + ku = F_c \cos(\beta - \alpha) - \left(C\frac{b}{V}\cos^2(\alpha) \right)\dot{u}. \tag{11}$$

Rewriting Eq. 11 to combine the velocity terms yields:

$$m\ddot{u} + \left(c + C\frac{b}{V}\cos^2(\alpha) \right)\dot{u} + ku = F_c \cos(\beta - \alpha), \tag{12}$$

where the new viscous damping coefficient is $c_{new} = \left(c + C\frac{b}{V}\cos^2(\alpha) \right)$. Replacing the original damping coefficient, *c*, (from the structural dynamics only) with c_{new} enables process damping to be incorporated in the analytical stability model. The new FRF is then:

$$G_u = \frac{U}{F_c \cos(\beta - \alpha)} = \frac{1}{-m\omega^2 + ic_{new}\omega + k}. \quad (13)$$

The modified FRF is a function of the spindle speed-dependent limiting chip width and the cutting speed (which, in turn, depends on the spindle speed). Therefore, the chip width and spindle speed values must be known beforehand to incorporate process damping effects. This leads to an iterative, converging analysis, in which the new damping coefficient is updated after each iteration. The stability boundary is established for each lobe number, *N*, using the following steps:

1. The analytical stability boundary is calculated with no process damping to identify the initial *b* and *Ω* vectors.
2. These vectors are used to determine the corresponding c_{new} vector.
3. The stability analysis is repeated with the new damping value to determine updated *b* and *Ω* vectors.
4. The process is repeated until the stability boundary converges.

To demonstrate this approach, consider the model in Figure 3.2 with $\alpha = 0°$, $k = 6.48 \times 10^6$ N/m, $m = 0.561$ kg, $c = 145$ N · s/m, $K_s = 2927 \times 10^6$ N/m^2, $\beta = 61.8°$ and $d = 35$ mm. The stability boundary with no process damping ($C = 0$ N/m) is shown in Figure 3.4 for *N* = 0 to 100 lobes. It is observed that the limiting chip width approaches the asymptotically stable chip width of $b = 0.37$ mm for spindle speeds below $\Omega = 1000$ rpm.

Results for the converging procedure with process damping for the N = 20 stability lobe are provided in Figure 3.5. Converging behavior is observed for the 10 iterations as the lobes move up and slightly to the right. A practical selection of 20 iterations was applied for the diagrams throughout this study to ensure convergence. Figure 3.6 displays the new stability diagram for N = 0 to 100 with $C = 6.11 \times 10^5$ N/m.

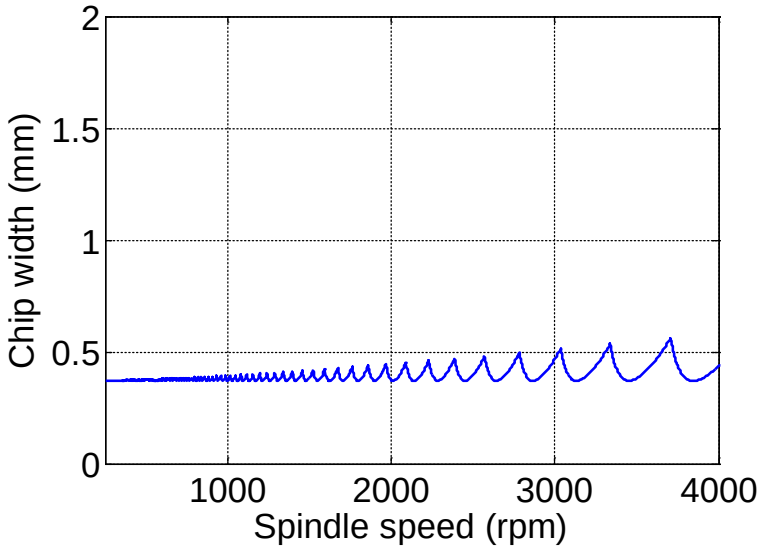

Figure 3.4: Stability diagram for the single DOF model from Figure 3.2, with no process damping.

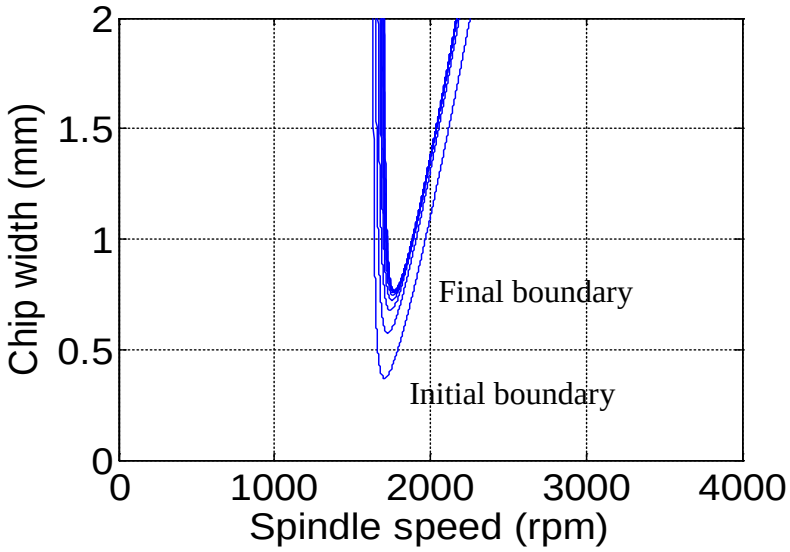

Figure 3.5: Convergence demonstration (N = 20 for 10 iterations) for the single degree-of-freedom model from Figure 3.2 with $C = 6.11 \times 10^5$ N/m.

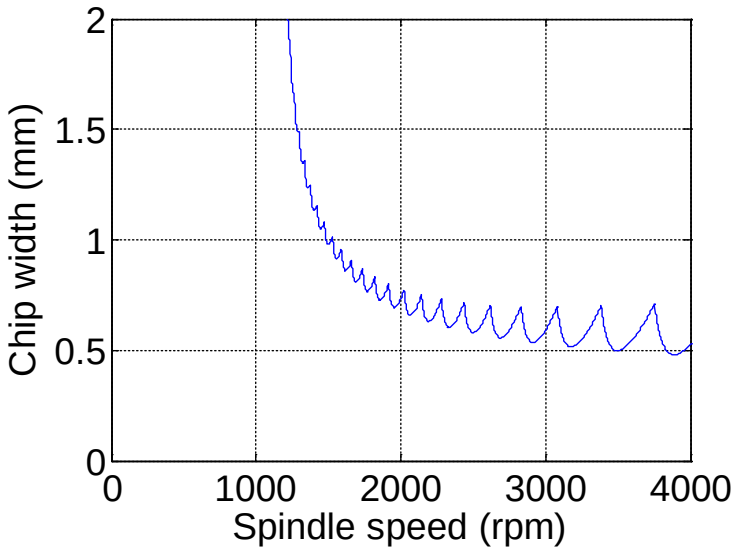

Figure 3.6: Stability diagram for the single degree-of-freedom turning model from Figure 3.6 with $C = 6.11 \times 10^5$ N/m.

3.2.2 Single DOF Turning in Two Directions

In some cases, it is not sufficient to consider the system flexibility in one direction only. The process damping model can be extended to include vibration in two orthogonal directions as illustrated in Figure 3.7.

To proceed with the analytical solution, the process damping force, defined in Eq 6, and the cutting force are projected into the u_1 and u_2 directions as shown in Eqs. 14 and 15, where $F_{c1}$and $F_{c2}$are the cutting force components in the u_1 and u_2 directions.

$$F_{u1} = F_c \cos(\beta - \alpha_1) - \left(C \frac{b}{V} \cos(\alpha_1) \right) \dot{y} = F_{c1} - \left(C \frac{b}{V} \cos(\alpha_1) \right) \dot{y} \tag{14}$$

$$F_{u2} = F_c \cos(\beta - \alpha_2) - \left(C \frac{b}{V} \cos(\alpha_2) \right) \dot{y} = F_{c2} - \left(C \frac{b}{V} \cos(\alpha_2) \right) \dot{y} \tag{15}$$

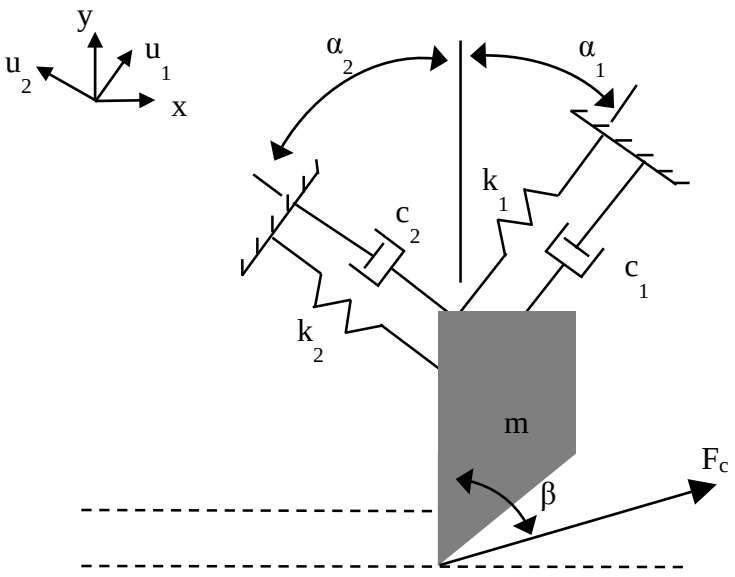

Figure 3.7: Turning model with a single DOF in two orthogonal directions.

The time domain equations of motion for the two directions are provided in Eqs. 16 and 17, where $m_i, c_i,$ and k_i, $i = 1, 2$, are the mass, viscous damping coefficient, and stiffness for the single DOF structural dynamics.

$$m_1\ddot{u}_1 + c_1\dot{u}_1 + k_1u_1 = F_{c1} - \left(C\frac{b}{V}\cos(\alpha_1)\right)\dot{y} \tag{16}$$

$$m_2\ddot{u}_2 + c_2\dot{u}_2 + k_2u_2 = F_{c2} - \left(C\frac{b}{V}\cos(\alpha_2)\right)\dot{y} \tag{17}$$

The *y* direction velocity can be written as a function of the velocities in the u_1 and u_2 directions as shown in Eq. 18. Substitution of Eq. 18 into Eqs. 16 and 17 yields Eqs. 19 and 20. Even though the structural dynamics are uncoupled (orthogonal), the equations of motion for the two directions are now coupled through the $\dot{u}_1$ and $\dot{u}_2$ velocity terms.

$$\dot{y} = \dot{u}_1\cos(\alpha_1) + \dot{u}_2\cos(\alpha_2) \tag{18}$$

$$m_1\ddot{u}_1 + c_1\dot{u}_1 + k_1u_1 = F_{c_1} - C\frac{b}{V}(\dot{u}_1\cos(\alpha_1) + \dot{u}_2\cos(\alpha_2))\cos(\alpha_1) \tag{19}$$

$$m_2\ddot{u}_2 + c_2\dot{u}_2 + k_2u_2 = F_{c_2} - C\frac{b}{V}(\dot{u}_1\cos(\alpha_1) + \dot{u}_2\cos(\alpha_2))\cos(\alpha_2) \tag{20}$$

By assuming a solution of the form $u_1(t) = U_1e^{i\omega t}$ for harmonic motion, Eqs. 19 and 20 can be rewritten in the frequency domain. The results are provided in Eqs. 21 and 22, where the U_1 and U_2 terms have been grouped on the left hand side in both equations and the $e^{i\omega t}$ term has been dropped from both sides in each case.

$$\left(-m_1\omega^2 + i\omega\left(c_1 + C\frac{b}{V}(\cos(\alpha_1))^2\right) + k_1\right)U_1 + i\omega\left(C\frac{b}{V}\cos(\alpha_1)\cos(\alpha_2)\right)U_2 = F_{c_1} \tag{21}$$

$$\left(-m_2\omega^2 + i\omega\left(c_2 + C\frac{b}{V}(\cos(\alpha_2))^2\right) + k_2\right)U_2 + i\omega\left(C\frac{b}{V}\cos(\alpha_1)\cos(\alpha_2)\right)U_1 = F_{c_2} \tag{22}$$

These equations are arranged in matrix form as:

$$\begin{bmatrix} a_{11} & a_{12} \\ a_{21} & a_{22} \end{bmatrix} \begin{bmatrix} U_1 \\ U_2 \end{bmatrix} = \begin{bmatrix} F_{c1} \\ F_{c2} \end{bmatrix}, \tag{23}$$

where:

- $a_{11} = -m_1\omega^2 + i\omega\left(c_1 + C\frac{b}{V}(\cos(\alpha_1))^2\right) + k_1$
- $a_{12} = i\omega\left(C\frac{b}{V}\cos(\alpha_1)\cos(\alpha_2)\right)$
- $a_{21} = a_{12}$
- $a_{22} = -m_2\omega^2 + i\omega\left(c_2 + C\frac{b}{V}(\cos(\alpha_2))^2\right) + k_2$

Using complex matrix inversion on a frequency-by-frequency basis, the direct and cross frequency response functions for the coupled dynamic system are obtained, as shown in Eq. 24. The direct FRFs are located in the on-diagonal positions and the cross FRFs are located in the off-diagonal positions; the cross FRFs are equal, because the inverted matrix is symmetric.

The fundamental stability equations (Eqs. 3-5) are then used to relate the limiting stable

$$\begin{bmatrix} U_1 \\ U_2 \end{bmatrix} = \begin{bmatrix} a_{11} & a_{12} \\ a_{21} & a_{22} \end{bmatrix}^{-1} \begin{bmatrix} F_{c1} \\ F_{c2} \end{bmatrix} = \begin{bmatrix} \frac{U_1}{F_{c1}} & \frac{U_1}{F_{c2}} \\ \frac{U_2}{F_{c1}} & \frac{U_2}{F_{c2}} \end{bmatrix} \begin{bmatrix} F_{c1} \\ F_{c2} \end{bmatrix} \tag{24}$$

chip width, b_{lim}, to the commanded spindle speed, Ω. However, Tlusty's approach is extended here to develop an oriented FRF that incorporates both the direct and cross FRFs from Eq. 24. The oriented FRF is defined using Eq. 25, where μ_{ij} $(i, j = 1,2)$ are the directional orientation factors:

- $\mu_{11} = \cos(\beta - \alpha_1)\cos(\alpha_1)$ projects *F* into u_1 to cause u_1 vibration through the direct FRF $\frac{U_1}{F_{c_1}}$ and then projects this result into *y*.

- $\mu_{12} = \cos(\beta + \alpha_2)\cos(\alpha_1)$ projects F into u_2 to cause u_1 vibration through the cross FRF $\frac{U_1}{F_{c_2}}$ and then projects this result into y.
- $\mu_{21} = \cos(\beta - \alpha_1)\cos(\alpha_2)$ projects F into u_1 to cause u_2 vibration through the cross FRF $\frac{U_2}{F_{c_1}}$ and then projects this result into y.
- $\mu_{22} = \cos(\beta + \alpha_2)\cos(\alpha_2)$ projects F into u_2 to cause u_2 vibration through the direct FRF $\frac{U_2}{F_{c_2}}$ and then projects this result into y.

$$G_{or} = \mu_{11}\frac{U_1}{F_{c_1}} + \mu_{12}\frac{U_1}{F_{c_2}} + \mu_{21}\frac{U_2}{F_{c_1}} + \mu_{22}\frac{U_2}{F_{c_2}} \tag{25}$$

The direct and cross FRFs included in Eq. 25 incorporate the process damping contribution by modifying the structural damping through the terms: $i\omega\left(c_1 + C\frac{b}{V}(\cos(\alpha_1))^2\right)$, $i\omega\left(C\frac{b}{V}\cos(\alpha_1)\cos(\alpha_2)\right)$, and $i\omega\left(c_2 + C\frac{b}{V}(\cos(\alpha_2))^2\right)$ as shown in Eq. 23. The process damping contribution depends on the $\frac{b}{V}$ ratio in each case, where $V = \frac{\pi d}{60}\Omega$ (d is the workpiece diameter and Ω is expressed in rpm). Therefore, the b and Ω vectors must be known in order to modify the damping. This again establishes a converging stability solution. As shown previously, the solution converges rapidly (20 iterations or less is typically sufficient).

To demonstrate the algorithm, consider the model in Figure 3.7 with α_1 = 30°, α_2 = 60°, β = 70°, K_s = 2000 N/mm^2, C = 200 N/mm, and d = 75 mm for an outer diameter turning operation. The structural dynamics are symmetric with a stiffness of 9×10^6 N/m, a

natural frequency of 900 Hz, and a viscous damping ratio of 0.03 (3%). The corresponding stability limit with process damping effects is displayed in Figure 3.8.

3.2.3 Multiple DOF Turning in Two Directions

The coupled dynamics solution is now extended to mutiple DOF turning in the two orthogonal directions, u_1 and u_2 as illustrated in Figure 3.9. From an FRF measurement in each direction, the modal parameters can be extracted. These modal parameters represent uncoupled single DOF systems in the modal coordinates q_1 and q_2 for the u_1 direction and p_1 and p_2 for the u_2 direction [25]. This modal representation requires that proportional damping hold, but this is a reasonable approximation for the lightly damped tool dynamics typically observed in practice.

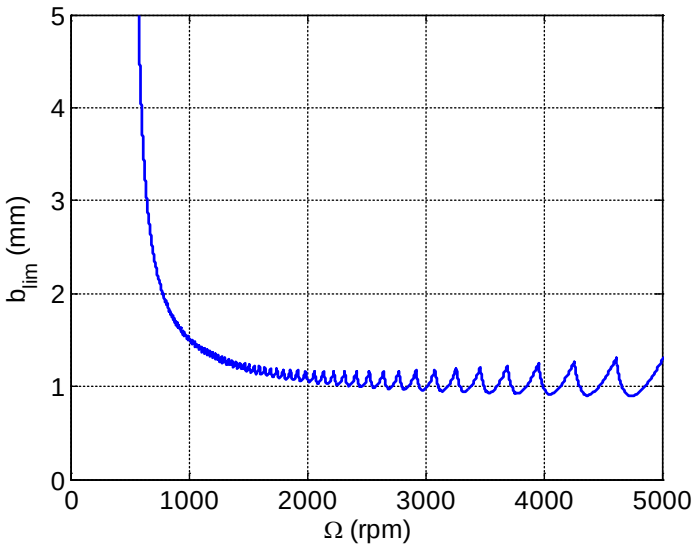

Figure 3.8: The analytical stability limit for turning model with a single DOF in two orthogonal directions.

Equation 16, which provides the equation of motion for the u_1 direction with a single DOF, is rewritten in Eq. 26 to describe motion in the first modal DOF, q_1. The y direction velocity is again $\dot{y} = \dot{u}_1 \cos(\alpha_1) + \dot{u}_2 \cos(\alpha_2)$, but $\dot{u}_1$ is now the sum of the modal

velocities, $\dot{u}_1 = \dot{q}_1 + \dot{q}_2$; the results for $\dot{u}_2$ are similar. Substitution yields Eqs. 27, 28 and 29 give the results for the second modal degree of freedom motion, q_2 in the u_1 direction.

$$m_{q1}\ddot{q}_1 + c_{q1}\dot{q}_1 + k_{q1}q_1 = F_{c1} - \left(C\frac{b}{V}\cos(\alpha_1)\right)\dot{y} \tag{26}$$

$$m_{q_1}\ddot{q}_1 + c_{q_1}\dot{q}_1 + k_{q_1}q_1 = F_{c_1} - C\frac{b}{V}\cos(\alpha_1)\left(\cos(\alpha_1)\,(\dot{q}_1 + \dot{q}_2) + \cos(\alpha_2)\,(\dot{p}_1 + \dot{p}_2)\right) \tag{27}$$

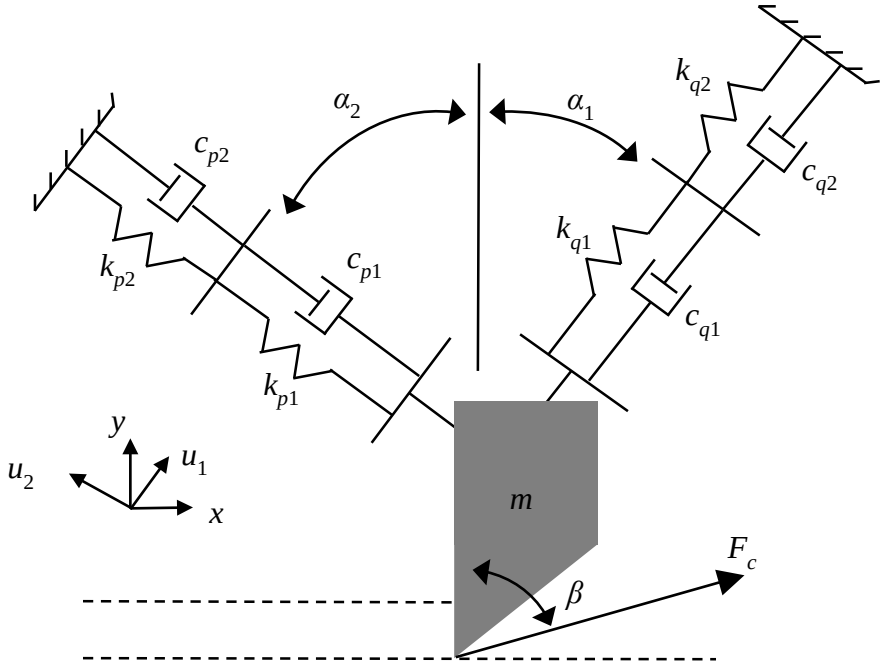

Figure 3.9: Two DOF in two orthogonal directions turning model.

$$m_{q2}\ddot{q}_2 + c_{q2}\dot{q}_2 + k_{q2}q_2 = F_{c1} - \left(C\frac{b}{V}\cos(\alpha_1)\right)\dot{y} \tag{28}$$

$$m_{q_2}\ddot{q}_2 + c_{q_2}\dot{q}_2 + k_{q_2}q_2 = F_{c_1} - C\frac{b}{V}\cos(\alpha_1)\left(\cos(\alpha_1)\,(\dot{q}_1 + \dot{q}_2) + \cos(\alpha_2)\,(\dot{p}_1 + \dot{p}_2)\right) \tag{29}$$

Equations 27 and 29 are converted to the frequency domain by again assuming harmonic motion so that $q_j(t) = Q_j e^{i\omega t}$ and $p_j(t) = P_j e^{i\omega t}$ for j = 1, 2. Equation 27

represents motion in Q_1 and Eq. 29 describes motion in Q_2. Even though the modal degrees of freedom are uncoupled by definition, the two equations of motion for the u_1 direction now include both Q_1 and Q_2 due to process damping. Similar to the single DOF model in the previous section, the equations also include contributions from the u_2 direction dynamics (P_1 and P_2). Interestingly, the equations of motion are coupled in both modal coordinates and the two orthogonal directions. This presents a rich dynamic system which is unlike other machining models.

$$\left(-m_{q_1}\omega^2 + i\omega\left(c_{q_1} + C\frac{b}{V}(\cos(\alpha_1))^2\right) + k_{q_1}\right)Q_1 + \left(i\omega C\frac{b}{V}(\cos(\alpha_1))^2\right)Q_2 + \left(C\frac{b}{V}\cos(\alpha_1)\cos(\alpha_2)\right)(P_1 + P_2) = F_{c_1} \tag{30}$$

$$\left(-m_{q_2}\omega^2 + i\omega\left(c_{q_2} + C\frac{b}{V}(\cos(\alpha_1))^2\right) + k_{q_2}\right)Q_2 + \left(i\omega C\frac{b}{V}(\cos(\alpha_1))^2\right)Q_1 + \left(C\frac{b}{V}\cos(\alpha_1)\cos(\alpha_2)\right)(P_1 + P_2) = F_{c_1} \tag{31}$$

Following the same approach, the frequency domain equations for the u_2 direction are presented in Eqs 32 and 33 where Eq. 32 describes motion in P_1 and Eq. 33 describes motion in P_2.

$$\left(-m_{p_1}\omega^2 + i\omega\left(c_{p_1} + C\frac{b}{V}(\cos(\alpha_2))^2\right) + k_{p_1}\right)P_1 + \left(i\omega C\frac{b}{V}(\cos(\alpha_2))^2\right)P_2 + \left(C\frac{b}{V}\cos(\alpha_1)\cos(\alpha_2)\right)(Q_1 + Q_2) = F_{c_2} \tag{32}$$

$$\left(-m_{p_2}\omega^2 + i\omega\left(c_{p_2} + C\frac{b}{V}(\cos(\alpha_2))^2\right) + k_{p_2}\right)P_2 + \left(i\omega C\frac{b}{V}(\cos(\alpha_2))^2\right)P_1 + \left(C\frac{b}{V}\cos(\alpha_1)\cos(\alpha_2)\right)(Q_1 + Q_2) = F_{c_2} \tag{33}$$

Equations 30-33 are arranged in matrix form as shown in Eq. 34, where:

- $a_{11} = \left(-m_{q_1}\omega^2 + i\omega\left(c_{q_1} + C\frac{b}{V}(\cos(\alpha_1))^2\right) + k_{q_1}\right)$
- $a_{12} = i\omega\left(C\frac{b}{V}(\cos(\alpha_1))^2\right)$
- $a_{13} = i\omega\left(C\frac{b}{V}\cos(\alpha_1)\cos(\alpha_2)\right)$
- $a_{14} = i\omega\left(C\frac{b}{V}\cos(\alpha_1)\cos(\alpha_2)\right)$
- $a_{21} = a_{12}$
- $a_{22} = \left(-m_{q_2}\omega^2 + i\omega\left(c_{q_2} + C\frac{b}{V}(\cos(\alpha_1))^2\right) + k_{q_2}\right)$
- $a_{23} = i\omega\left(C\frac{b}{V}\cos(\alpha_1)\cos(\alpha_2)\right)$
- $a_{24} = i\omega\left(C\frac{b}{V}\cos(\alpha_1)\cos(\alpha_2)\right)$
- $a_{31} = a_{13}$
- $a_{32} = a_{23}$
- $a_{33} = \left(-m_{p_1}\omega^2 + i\omega\left(c_{p_1} + C\frac{b}{V}(\cos(\alpha_2))^2\right) + k_{p_1}\right)$
- $a_{34} = i\omega\left(C\frac{b}{V}\cos(\alpha_1)\cos(\alpha_2)\right)$
- $a_{41} = a_{14}$
- $a_{42} = a_{24}$
- $a_{43} = a_{34}$
- $a_{44} = \left(-m_{p_2}\omega^2 + i\omega\left(c_{p_2} + C\frac{b}{V}(\cos(\alpha_2))^2\right) + k_{p_2}\right)$.

$$\begin{bmatrix} Q_1 \\ Q_2 \\ P_1 \\ P_2 \end{bmatrix} = \begin{bmatrix} a_{11} & a_{12} & a_{13} & a_{14} \\ a_{21} & a_{22} & a_{23} & a_{24} \\ a_{31} & a_{32} & a_{33} & a_{34} \\ a_{41} & a_{42} & a_{43} & a_{44} \end{bmatrix}^{-1} \begin{bmatrix} F_{c1} \\ F_{c1} \\ F_{c2} \\ F_{c2} \end{bmatrix} = \begin{bmatrix} \frac{Q_{1,1}}{F_{c1}} & \frac{Q_{1,2}}{F_{c1}} & \frac{Q_{1,3}}{F_{c2}} & \frac{Q_{1,4}}{F_{c2}} \\ \frac{Q_{2,1}}{F_{c1}} & \frac{Q_{2,2}}{F_{c1}} & \frac{Q_{2,3}}{F_{c2}} & \frac{Q_{2,4}}{F_{c2}} \\ \frac{P_{1,1}}{F_{c1}} & \frac{P_{1,2}}{F_{c1}} & \frac{P_{1,3}}{F_{c2}} & \frac{P_{1,4}}{F_{c2}} \\ \frac{P_{2,1}}{F_{c1}} & \frac{P_{2,2}}{F_{c1}} & \frac{P_{2,3}}{F_{c2}} & \frac{P_{2,4}}{F_{c2}} \end{bmatrix} \begin{bmatrix} F_{c1} \\ F_{c1} \\ F_{c2} \\ F_{c2} \end{bmatrix} \tag{34}$$

The direct FRFs in the u_1 and u_2 directions are defined by Eqs. 35 and 36 respectively; the cross FRFs are provided in Eqs. 37 and 38. The oriented FRF is again calculated using Eq. 25 and the directional orientation factors are the same.

$$\frac{U_1}{F_{c1}} = \frac{Q_{1,1}}{F_{c1}} + \frac{Q_{1,2}}{F_{c1}} + \frac{Q_{2,1}}{F_{c1}} + \frac{Q_{2,2}}{F_{c1}} \tag{35}$$

$$\frac{U_2}{F_{c2}} = \frac{P_{1,3}}{F_{c2}} + \frac{P_{1,4}}{F_{c2}} + \frac{P_{2,3}}{F_{c2}} + \frac{P_{2,4}}{F_{c2}} \tag{36}$$

$$\frac{U_2}{F_{c1}} = \frac{P_{1,1}}{F_{c1}} + \frac{P_{1,2}}{F_{c1}} + \frac{P_{2,1}}{F_{c1}} + \frac{P_{2,2}}{F_{c1}} \tag{37}$$

$$\frac{U_1}{F_{c2}} = \frac{Q_{1,3}}{F_{c2}} + \frac{Q_{1,4}}{F_{c2}} + \frac{Q_{2,3}}{F_{c2}} + \frac{Q_{2,4}}{F_{c2}} \tag{38}$$

The model may be extended to additional DOFs in each direction. For three DOFs in each direction, for example, Eq. 34 becomes a 6×6 symmetric matrix. The direct and cross FRFs are then a sum of six, rather than four, terms from the inverted matrix.

To demonstrate the multiple DOF algorithm, consider the model in Figure 3.9 with α_1 = 30°, α_2 = 60°, β = 70°, K_s = 2000 N/mm^2, C = 200 N/mm, and d = 75 mm for an outer diameter turning operation. The structural dynamics are symmetric with a modal stiffness of 7×10^6 N/m, a natural frequency of 600 Hz, and a viscous modal damping ratio of 0.03 (3%) for the first mode and a modal stiffness of 9×10^6 N/m, a natural frequency of 900 Hz, and a viscous modal damping ratio of 0.03 (3%) for the second mode. The corresponding stability limit with process damping effects is displayed in Figure 3.10.

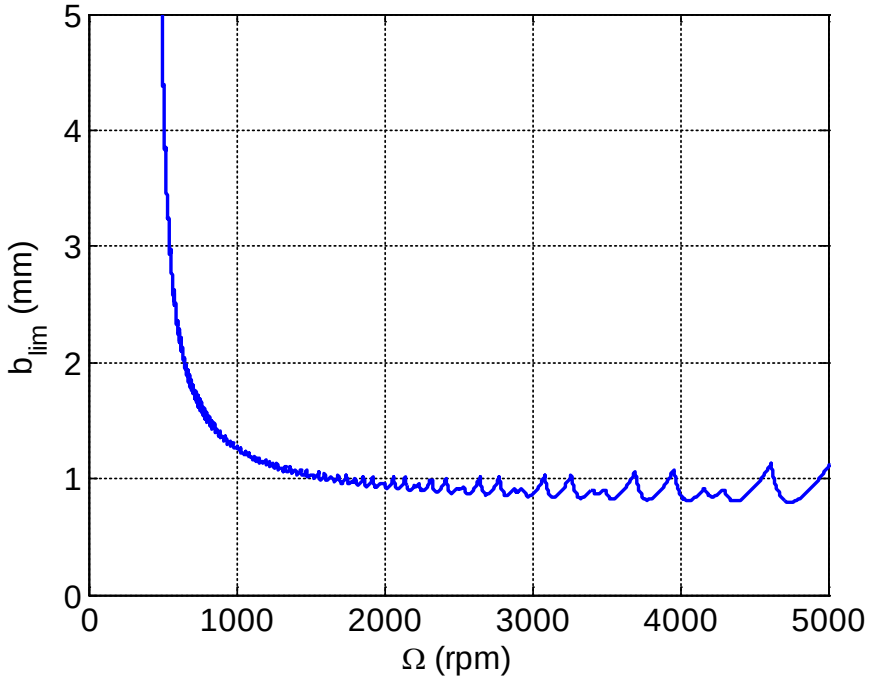

Figure 3.10: Analytical stability limit results for turning model with two DOF in two orthogonal directions.

CHAPTER 4: ANALYTICAL STABILITY ALGORITHM PART 2: MILLING

Tlusty [2] modified the turning analysis to accommodate the milling process. A primary obstacle to defining an analytical solution for milling (aside from the same inherent time delay) is the time dependence of the cutting force direction. Tlusty solved this problem by assuming an average angle of the tooth in the cut, ϕ_{ave}, and, therefore, an average force direction. This produced an autonomous, or time-invariant, system.

In this chapter, an analytical solution, similar to solution presented for turning in Chapter 3, is presented that enables single and multiple DOF structural dynamics to be considered with the inclusion of process damping effects. The solution is carried out in a similar manner by describing a process damping force in the surface normal direction of the cut as a function of depth of cut, cutting speed, tool velocity and a single empirical process damping coefficient. The analytical solution for milling is presented in the following sections.

4.1 Stability Analysis Including Process Damping

The milling models are depicted in Figure 4.1 and 4.2Figure 4.2, where x is the feed direction (the positive direction indicates the workpiece motion for a fixed tool position). The cutting force, F_c, inclined relative to the surface normal, n, by the angle β is also displayed. The surface normal is shown to be oriented at the average angle of a tooth in the cut, ϕ_{ave}, which is the mean of the cut starting, ϕ_s, and exit, ϕ_e, angles. These angles are

defined by the milling operation (up/conventional or down/climb milling) and the radial depth of cut. Figure 4.1 and 4.2 illustrate up/conventional and down/climb milling operation at arbitrary radial immersions, respectively.

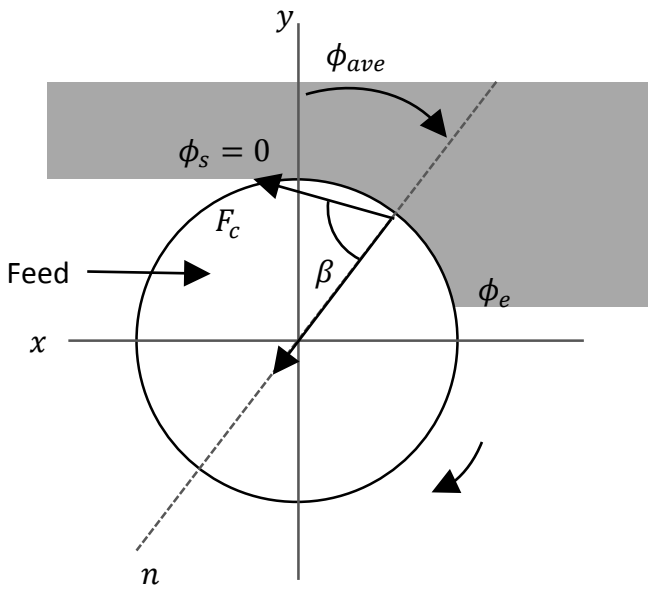

Figure 4.1: Milling model for up/conventional milling. The vector *n* defines the average surface normal direction and *x* is the feed direction.

The variable component of the cutting force is described by Eq. 39, where K_s is the specific cutting force coefficient that relates the cutting force to the chip area, *b* is the commanded axial depth of cut, $n_0(t)$ is the vibration amplitude in the *n* direction from the previous tooth, and $n(t)$ is the current vibration amplitude. The difference between n_0 and *n* identifies the variable chip thickness due to the vibration from one revolution to the next and provides the basis for regenerative chatter.

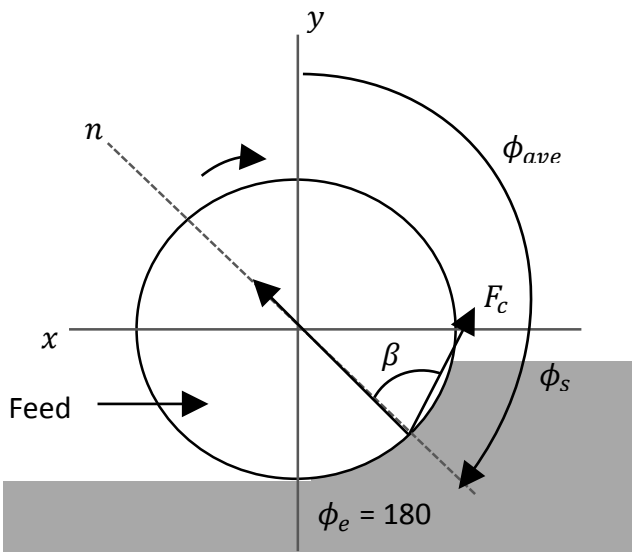

Figure 4.2: Milling model for down/climb milling. The vector *n* defines the average surface normal direction and *x* is the feed direction.

The mean component of the cutting force is excluded because it does not influence stability for the linear analysis presented here.

$$F_c = K_s b(n_0(t) - n(t)) \tag{39}$$

The assumption for Eq. 39 is that there is no phase shift between the variable force and the chip thickness. This is indicated by the real values of b and K_s. However, it has been shown that a phase shift can occur at low cutting speeds. This phenomenon is captured by the inclusion of the process damping force, F_d, defined in Eq. 40, where C is the process damping coefficient, V is the cutting speed, and $\dot{n}$ is the tool velocity in the n direction. The process damping force is oriented in the n direction and opposes the cutting force (as projected in the n direction). In other words, it is a viscous damping force; therefore, the

process damping force is used to modify the structural damping and obtain an analytical stability solution.

$$F_d = -C\frac{b}{V}\dot{n} \tag{40}$$

4.1.1 Single DOF Milling in Two Directions

To proceed with the solution, the cutting and process damping forces are projected into the *x* and *y* directions as shown in Eqs. (41)-(42), where $\phi_{ud} = 90 - \phi_{ave}$ for up milling and $\phi_{ud} = \phi_{ave} - 90$ for down milling.

$$F_x = F_c\cos(\beta + \phi_{ave} - 90) - C\frac{b}{V}\dot{n}\cos(\phi_{ud}) = F_{c_x} - C\frac{b}{V}\dot{n}\cos(\phi_{ud}) \tag{41}$$

$$\begin{aligned} F_y &= F_c\cos(180 - \phi_{ave} - \beta) - C\frac{b}{V}\dot{n}\cos(180 - \phi_{ave}) \\ &= F_{c_y} - C\frac{b}{V}\dot{n}\cos(180 - \phi_{ave}) \end{aligned} \tag{42}$$

The time domain equations of motion for the two directions are provided in Eqs. 43-44, where m_i, c_i, and k_i, $i = x, y$, are the mass, viscous damping coefficient, and stiffness for the single DOF structural dynamics. In these equations, one overdot indicates one time derivative (velocity) and two overdots indicate two time derivatives (acceleration).

$$m_x\ddot{x} + c_x\dot{x} + k_x x = F_{c_x} - C\frac{b}{V}\dot{n}\cos(\phi_{ud}) \tag{43}$$

$$m_y\ddot{y} + c_y\dot{y} + k_y y = F_{c_y} - C\frac{b}{V}\dot{n}\cos(180 - \phi_{ave}) \tag{44}$$

The *n* direction velocity can be written as a function of the velocities in the *x* and *y* directions as shown in Eq. 45. Substitution of Eq. 45 into Eqs. 43-44 yields Eqs. 46-47. Even though the structural dynamics are uncoupled (orthogonal), the equations of motion for the two directions are now coupled through the $\dot{x}$ and $\dot{y}$ velocity terms.

$$\dot{n} = \dot{x}\cos(\phi_{ud}) + \dot{y}\cos(180 - \phi_{ave}) \tag{45}$$

$$m_x\ddot{x} + c_x\dot{x} + k_x x = F_{c_x} - C\frac{b}{V}\cos(\phi_{ud})\left(\dot{x}\cos(\phi_{ud}) + \dot{y}\cos(180 - \phi_{ave})\right) \tag{46}$$

$$m_y\ddot{y} + c_y\dot{y} + k_y y = F_{c_y} - C\frac{b}{V}\cos(180 - \phi_{ave})\left(\dot{x}\cos(\phi_{ud}) + \dot{y}\cos(180 - \phi_{ave})\right) \tag{47}$$

By assuming solutions of the form $x(t) = Xe^{i\omega t}$ and $y(t) = Ye^{i\omega t}$ for harmonic motion, Eqs. 46-47 can be rewritten in the frequency domain (ω is frequency). The results are provided in Eqs. 48-49, where the *X* and *Y* terms have been grouped on the left hand side of both equations and the $e^{i\omega t}$ term has been dropped from both sides.

$$\left(-m_x\omega^2 + i\omega\left(c_x + C\frac{b}{V}\left(\cos(\phi_{ud})\right)^2\right) + k_x\right)X + i\omega\left(C\frac{b}{V}\cos(\phi_{ud})\cos(180 - \phi_{ave})\right)Y = F_{c_x} \tag{48}$$

$$\left(-m_y\omega^2 + i\omega\left(c_y + C\frac{b}{V}\left(\cos(180 - \phi_{ave})\right)^2\right) + k_y\right)Y + i\omega\left(C\frac{b}{V}\cos(\phi_{ud})\cos(180 - \phi_{ave})\right)X = F_{c_y} \tag{49}$$

These equations are arranged in matrix form as shown in Eq. (50), where:

- $a_{11} = \left(-m_x\omega^2 + i\omega\left(c_x + C\frac{b}{V}\left(\cos(\phi_{ud})\right)^2\right) + k_x\right)$
- $a_{12} = i\omega\left(C\frac{b}{V}\cos(\phi_{ud})\cos(180 - \phi_{ave})\right)$

- $a_{21} = a_{12}$
- $a_{22} = \left(-m_y\omega^2 + i\omega\left(c_y + C\frac{b}{V}\left(\cos\left(180 - \phi_{ave}\right)\right)^2\right) + k_y\right)$.

$$\begin{bmatrix} a_{11} & a_{12} \\ a_{21} & a_{22} \end{bmatrix}\begin{bmatrix} X \\ Y \end{bmatrix} = \begin{bmatrix} F_{cx} \\ F_{cy} \end{bmatrix}, \tag{50}$$

Using complex matrix inversion on a frequency-by-frequency basis, the direct and cross frequency response functions (FRFs) for the coupled dynamic system are obtained as shown in Eq. 51. The direct FRFs are located in the on-diagonal positions and the cross FRFs are located in the off-diagonal positions; the cross FRFs are equal because the inverted matrix is symmetric.

$$\begin{bmatrix} X \\ Y \end{bmatrix} = \begin{bmatrix} a_{11} & a_{12} \\ a_{21} & a_{22} \end{bmatrix}^{-1}\begin{bmatrix} F_{cx} \\ F_{cy} \end{bmatrix} = \begin{bmatrix} \frac{X}{F_{cx}} & \frac{X}{F_{cy}} \\ \frac{Y}{F_{cx}} & \frac{Y}{F_{cy}} \end{bmatrix}\begin{bmatrix} F_{cx} \\ F_{cy} \end{bmatrix} \tag{51}$$

This work builds on the analytical stability solution presented by Tlusty [2]. As shown in Figure 4.1 and Figure 4.2, he assumed an average angle of the tooth in the cut and, therefore, an average cutting force direction. This produced an autonomous, or time invariant, system. He then made use of directional orientation factors, μ_x and μ_y, to first project this force into the *x* and *y* directions and, second, project these results into the surface normal, *n* (in the direction of ϕ_{ave}). The limiting axial depth of cut, b_{lim}, and spindle speed, Ω, are defined as a function of frequency using Eqs. 52-54, where $Re(G_{or})$ is the negative real part of the oriented FRF, N_t^* is the average number of teeth in the cut (see Eq.

(54), where the angles are expressed in°), f_c is the valid chatter frequencies (i.e., those frequencies where $Re(G_{or})$ is negative), N_t is the number of cutter teeth, N = 0, 1, 2, … is the integer number of waves between teeth (i.e., the lobe number), and $\varepsilon = 2\pi - 2\tan^{-1}\left(\frac{Re(G_{or})}{Im(G_{or})}\right)$ is the phase between the current vibration and the previous tooth. The spindle speed and limiting axial depth are plotted against one another to represent the stability boundary in traditional stability lobe diagrams.

$$b_{\lim} = \frac{-1}{2K_s \operatorname{Re}\left(G_{or}\right) N_t^*} \tag{52}$$

$$\frac{f_c}{\Omega} = N + \frac{\varepsilon}{2\pi} \tag{53}$$

$$N_t^* = \frac{\phi_e - \phi_s}{360/N_t} \tag{54}$$

Tlusty's approach is extended here to develop an oriented FRF that incorporates both the direct and cross FRFs from Eq. 51. The oriented FRF is defined using Eq. 55, where μ_{ij}, $i, j = x, y$, are the directional orientation factors:

- $\mu_{xx} = \cos\left(\beta + \phi_{ave} - 90\right)\cos\left(\phi_{ud}\right)$ projects F into x to cause x vibration through the direct FRF $\frac{X}{F_{c_x}}$ and then projects this result into n
- $\mu_{xy} = \cos\left(180 - \beta + \phi_{ave}\right)\cos\left(\phi_{ud}\right)$ projects F into y to cause x vibration through the cross FRF $\frac{X}{F_{c_y}}$ and then projects this result into n

- $\mu_{yx} = \cos(\beta + \phi_{ave} - 90)\cos(180 - \phi_{ave})$ projects *F* into *x* to cause *y* vibration through the cross FRF $\frac{Y}{F_{c_x}}$ and then projects this result into *n*
- $\mu_{yy} = \cos(180 - \beta + \phi_{ave})\cos(180 - \phi_{ave})$ projects *F* into *y* to cause *y* vibration through the direct FRF $\frac{Y}{F_{c_y}}$ and then projects this result into *n*.

$$G_{or} = \mu_{xx}\frac{X}{F_{c_x}} + \mu_{xy}\frac{X}{F_{c_y}} + \mu_{yx}\frac{Y}{F_{c_x}} + \mu_{yy}\frac{Y}{F_{c_y}} \tag{55}$$

The direct and cross FRFs included in Eq. 55 incorporate the process damping contribution by modifying the structural damping through the terms: $i\omega\left(c_x + C\frac{b}{V}\left(\cos(\phi_{ud})\right)^2\right)$, $i\omega\left(C\frac{b}{V}\cos(\phi_{ud})\cos(180 - \phi_{ave})\right)$, and $i\omega\left(c_y + C\frac{b}{V}\left(\cos(180 - \phi_{ave})\right)^2\right)$ as shown in Eq. 50. The process damping contribution depends on the $\frac{b}{V}$ ratio in each case, where $V = \frac{\pi d}{60}\Omega$ (d is the tool diameter and Ω is expressed in rpm). Therefore, the b and Ω vectors must be known in order to modify the damping. This establishes a converging stability solution. The following steps are completed for each lobe number, *N*:

1. the analytical stability boundary is calculated with no process damping to identify initial b and Ω vectors
2. these vectors are used to determine the process damping contribution
3. the stability analysis is repeated with the new damping terms to determine updated b and Ω vectors
4. the process is repeated until the stability boundary converges.

Again, the solution converges rapidly (20 iterations or less is typically sufficient).

To demonstrate the algorithm, consider the model in Figure 4.1 with $\phi_s = 0$, $\phi_e = 90°$, $\beta = 70°$, $K_s = 2000$ N/mm^2, $C = 200$ N/mm, $N_t = 4$, and $d = 19$ mm for a 50% radial immersion up milling operation. The structural dynamics are symmetric in x and y with a stiffness of 9×10^6 N/m, a natural frequency of 900 Hz, and a viscous damping ratio of 0.03 (3%). The corresponding stability limit with process damping effects is displayed in Figure 4.3.

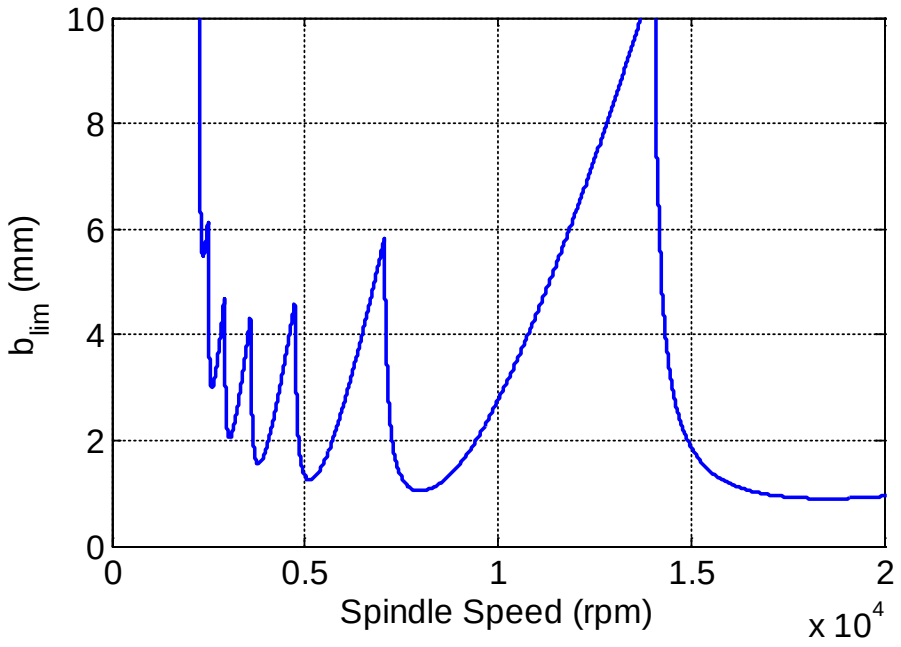

Figure 4.3: Analytical stability limit results for milling model with a single DOF in the x and y directions.

4.1.2 Multi-Degree-of-Freedom Milling in Two Directions

The coupled dynamics solution is now extended to two DOF in the *x* and *y* directions. From an FRF measurement in each direction, the modal parameters can be extracted (by peak picking, for example) which represent uncoupled single DOF systems in the modal coordinates q_1 and q_2 for the *x* direction and p_1 and p_2 for the *y* direction [25]. This modal representation requires that proportional damping holds, but this is a reasonable approximation for the lightly damped tool point dynamics typically observed in practice.

Equation 43, which provides the equation of motion for the *x* direction with a single DOF, is rewritten in Eq. 56 to describe motion in the first modal DOF, q_1. The *n* direction velocity is again $\dot{n} = \dot{x}\cos(\phi_{ud}) + \dot{y}\cos(180 - \phi_{ave})$, but $\dot{x}$ is now the sum of the modal velocities, $\dot{x} = \dot{q}_1 + \dot{q}_2$ and $\dot{y} = \dot{p}_1 + \dot{p}_2$. Substitution yields Eq. 57. Equations 58 and 59 give the results for q_2 motion (the second modal DOF) in the *x* direction.

$$m_{q_1}\ddot{q}_1 + c_{q_1}\dot{q}_1 + k_{q_1}q_1 = F_{c_x} - C\frac{b}{V}\dot{n}\cos(\phi_{ud}) \tag{56}$$

$$m_{q_1}\ddot{q}_1 + c_{q_1}\dot{q}_1 + k_{q_1}q_1 = F_{c_x} - C\frac{b}{V}\cos(\phi_{ud})\left(\cos(\phi_{ud})(\dot{q}_1 + \dot{q}_2) + \cos(180 - \phi_{ave})(\dot{p}_1 + \dot{p}_2)\right) \tag{57}$$

$$m_{q_2}\ddot{q}_2 + c_{q_2}\dot{q}_2 + k_{q_2}q_2 = F_{c_x} - C\frac{b}{V}\dot{n}\cos(\phi_{ud}) \tag{58}$$

$$m_{q_2}\ddot{q}_2 + c_{q_2}\dot{q}_2 + k_{q_2}q_2 = F_{c_x} - C\frac{b}{V}\cos(\phi_{ud})\left(\cos(\phi_{ud})(\dot{q}_1 + \dot{q}_2) + \cos(180 - \phi_{ave})(\dot{p}_1 + \dot{p}_2)\right) \tag{59}$$

Equations 57 and 59 are converted to the frequency domain by again assuming harmonic motion so that $q_j(t) = Q_j e^{i\omega t}$ and $p_j(t) = P_j e^{i\omega t}$, j = 1, 2. Equation 60 represents motion in Q_1 and Eq. (61) describes motion in Q_2. Even though the modal degrees of freedom are uncoupled by definition, the two equations of motion for the *x* direction now include both Q_1 and Q_2 due to process damping. Similar to the single DOF model in the previous section, the equations also include contributions from the *y* direction dynamics (P_1 and P_2). As with turning, the equations of motion are coupled in both modal coordinates and the two orthogonal directions [26].

$$\left(-m_{q_1}\omega^2 + i\omega\left(c_{q_1} + C\frac{b}{V}\left(\cos\left(\phi_{ud}\right)\right)^2\right) + k_{q_1}\right)Q_1 + i\omega\left(C\frac{b}{V}\left(\cos\left(\phi_{ud}\right)\right)^2\right)Q_2 + i\omega\left(C\frac{b}{V}\cos\left(\phi_{ud}\right)\cos\left(180 - \phi_{ave}\right)\right)(P_1 + P_2) = F_{c_x} \quad (60)$$

$$\left(-m_{q_2}\omega^2 + i\omega\left(c_{q_2} + C\frac{b}{V}\left(\cos\left(\phi_{ud}\right)\right)^2\right) + k_{q_2}\right)Q_2 + i\omega\left(C\frac{b}{V}\left(\cos\left(\phi_{ud}\right)\right)^2\right)Q_1 + i\omega\left(C\frac{b}{V}\cos\left(\phi_{ud}\right)\cos\left(180 - \phi_{ave}\right)\right)(P_1 + P_2) = F_{c_x} \quad (61)$$

Following the same approach, the frequency domain equations for the *y* direction are presented in Eqs. 62 and 63, where Eq. 62 describes motion in P_1 and Eq. 63 describes motion in P_2.

$$\left(-m_{p_1}\omega^2 + i\omega\left(c_{p_1} + C\frac{b}{V}\left(\cos\left(180-\phi_{ave}\right)\right)^2\right) + k_{p_1}\right)P_1 + i\omega\left(C\frac{b}{V}\left(\cos\left(180-\phi_{ave}\right)\right)^2\right)P_2 + i\omega\left(C\frac{b}{V}\cos\left(\phi_{ud}\right)\cos\left(180-\phi_{ave}\right)\right)(Q_1+Q_2) = F_{c_y} \quad (62)$$

$$\left(-m_{p_2}\omega^2 + i\omega\left(c_{p_2} + C\frac{b}{V}\left(\cos\left(180-\phi_{ave}\right)\right)^2\right) + k_{p_2}\right)P_2 + i\omega\left(C\frac{b}{V}\left(\cos\left(180-\phi_{ave}\right)\right)^2\right)P_1 + i\omega\left(C\frac{b}{V}\cos\left(180-\phi_{ave}\right)\cos\left(\phi_{ud}\right)\right)(Q_1+Q_2) = F_{c_2} \quad (63)$$

Equations 60-63 are arranged in matrix form as shown in Eq. 64, where:

- $a_{11} = \left(-m_{q_1}\omega^2 + i\omega\left(c_{q_1} + C\frac{b}{V}\left(\cos\left(\phi_{ud}\right)\right)^2\right) + k_{q_1}\right)$
- $a_{12} = i\omega\left(C\frac{b}{V}\left(\cos\left(\phi_{ud}\right)\right)^2\right)$
- $a_{13} = i\omega\left(C\frac{b}{V}\cos\left(\phi_{ud}\right)\cos\left(180-\phi_{ave}\right)\right)$
- $a_{14} = i\omega\left(C\frac{b}{V}\cos\left(\phi_{ud}\right)\cos\left(180-\phi_{ave}\right)\right)$
- $a_{21} = a_{12}$
- $a_{22} = \left(-m_{q_2}\omega^2 + i\omega\left(c_{q_2} + C\frac{b}{V}\left(\cos\left(\phi_{ud}\right)\right)^2\right) + k_{q_2}\right)$
- $a_{23} = i\omega\left(C\frac{b}{V}\cos\left(\phi_{ud}\right)\cos\left(180-\phi_{ave}\right)\right)$
- $a_{24} = i\omega\left(C\frac{b}{V}\cos\left(\phi_{ud}\right)\cos\left(180-\phi_{ave}\right)\right)$
- $a_{31} = a_{13}$
- $a_{32} = a_{23}$
- $a_{33} = \left(-m_{p_1}\omega^2 + i\omega\left(c_{p_1} + C\frac{b}{V}\left(\cos\left(180-\phi_{ave}\right)\right)^2\right) + k_{p_1}\right)$

- $a_{34} = i\omega\left(C\frac{b}{V}\cos(\phi_{ud})\cos(180-\phi_{ave})\right)$
- $a_{41} = a_{14}$
- $a_{42} = a_{24}$
- $a_{43} = a_{34}$
- $a_{44} = \left(-m_{p_2}\omega^2 + i\omega\left(c_{p_2} + C\frac{b}{V}\left(\cos(180-\phi_{ave})\right)^2\right) + k_{p_2}\right).$

$$\begin{bmatrix} a_{11} & a_{12} & a_{13} & a_{14} \\ a_{21} & a_{22} & a_{23} & a_{24} \\ a_{31} & a_{32} & a_{33} & a_{34} \\ a_{41} & a_{42} & a_{43} & a_{44} \end{bmatrix} \begin{bmatrix} Q_1 \\ Q_2 \\ P_1 \\ P_2 \end{bmatrix} = \begin{bmatrix} F_{c_x} \\ F_{c_x} \\ F_{c_y} \\ F_{c_y} \end{bmatrix} \tag{64}$$

Using complex matrix inversion on a frequency-by-frequency basis, the direct and cross FRFs for the coupled dynamic system are obtained as shown in Eq. 65.

$$\begin{bmatrix} Q_1 \\ Q_2 \\ P_1 \\ P_2 \end{bmatrix} = \begin{bmatrix} a_{11} & a_{12} & a_{13} & a_{14} \\ a_{21} & a_{22} & a_{23} & a_{24} \\ a_{31} & a_{32} & a_{33} & a_{34} \\ a_{41} & a_{42} & a_{43} & a_{44} \end{bmatrix}^{-1} \begin{bmatrix} F_{c_x} \\ F_{c_x} \\ F_{c_y} \\ F_{c_y} \end{bmatrix} = \begin{bmatrix} \frac{Q_{1,1}}{F_{c_x}} & \frac{Q_{1,2}}{F_{c_x}} & \frac{Q_{1,3}}{F_{c_y}} & \frac{Q_{1,4}}{F_{c_y}} \\ \frac{Q_{2,1}}{F_{c_x}} & \frac{Q_{2,2}}{F_{c_x}} & \frac{Q_{2,3}}{F_{c_y}} & \frac{Q_{2,4}}{F_{c_y}} \\ \frac{P_{1,1}}{F_{c_x}} & \frac{P_{1,2}}{F_{c_x}} & \frac{P_{1,3}}{F_{c_y}} & \frac{P_{1,4}}{F_{c_y}} \\ \frac{P_{2,1}}{F_{c_x}} & \frac{P_{2,2}}{F_{c_x}} & \frac{P_{2,3}}{F_{c_y}} & \frac{P_{2,4}}{F_{c_y}} \end{bmatrix} \begin{bmatrix} F_{c_x} \\ F_{c_x} \\ F_{c_y} \\ F_{c_y} \end{bmatrix} \tag{65}$$

The direct FRFs in the *x* and *y* directions are defined by Eqs. 66-69, respectively; the cross FRFs are provided in Eqs. 30-31. The oriented FRF is again calculated using Eq. 17; the directional orientation factors are the same.

$$\frac{X}{F_{c_x}} = \frac{Q_{1,1}}{F_{c_x}} + \frac{Q_{1,2}}{F_{c_x}} + \frac{Q_{2,1}}{F_{c_x}} + \frac{Q_{2,2}}{F_{c_x}} \tag{66}$$

$$\frac{Y}{F_{c_y}} = \frac{P_{1,3}}{F_{c_y}} + \frac{P_{1,4}}{F_{c_y}} + \frac{P_{2,3}}{F_{c_y}} + \frac{P_{2,4}}{F_{c_y}} \tag{67}$$

$$\frac{y}{F_{c_x}} = \frac{P_{1,1}}{F_{c_x}} + \frac{P_{1,2}}{F_{c_x}} + \frac{P_{2,1}}{F_{c_x}} + \frac{P_{2,2}}{F_{c_x}} \tag{68}$$

$$\frac{X}{F_{c_y}} = \frac{Q_{1,3}}{F_{c_y}} + \frac{Q_{1,4}}{F_{c_y}} + \frac{Q_{2,3}}{F_{c_y}} + \frac{Q_{2,4}}{F_{c_y}} \tag{69}$$

The model may be extended to additional DOFs in each direction. For three DOFs in each direction, for example, Eq. 64 becomes a 6×6 symmetric matrix. The direct and cross FRFs are then a sum of six, rather than four, terms from the inverted matrix.

To demonstrate the algorithm, consider the model in Figure 4.1 with $\phi_s = 0$, $\phi_e = 90°$, $\beta = 70°$, $K_s = 2000$ N/mm^2, $C = 200$ N/mm, $N_t = 4$, and $d = 19$ mm for a 50% radial immersion up milling operation. The structural dynamics are symmetric with a modal stiffness of 7×10^6 N/m, a natural frequency of 700 Hz, and a viscous modal damping ratio of 0.03 (3%) for the first mode and a modal stiffness of 9×10^6 N/m, a natural frequency of 900 Hz, and a viscous modal damping ratio of 0.03 (3%) for the second mode. The corresponding stability limit with process damping effects is displayed in Figure 4.4.

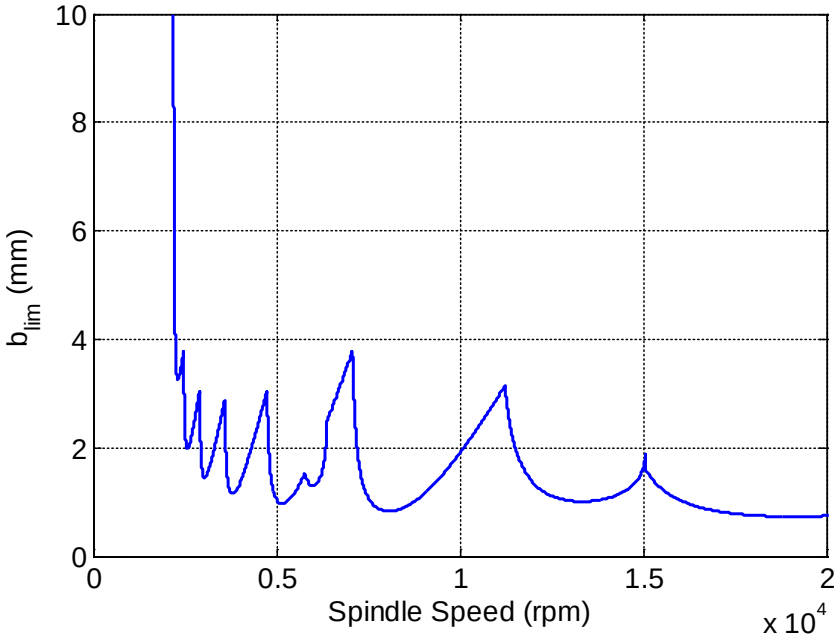

Figure 4.4: Analytical stability limit results for milling model with two DOF in the *x* and *y* directions.

CHAPTER 5: EXPERIMENTAL PROCEDURE

The stability algorithms described in Chapter 3 and Chapter 4 require the following information: the dynamics of the cutting system in the form of the frequency response function (FRF); the cutting force coefficient, K_s, and cutting force angle, β; the process damping coefficient, C; and other parameters specific to the cutting process, such as the radial depth of cut, number of cutting edges (in the case of milling), etc. This chapter presents experimental setups and procedures for acquiring the stability model parameters. It also presents a method for modeling the tool life for a given cutting operation, which proves useful for the hard-to-machine materials concerned with in this work.

5.1 Specific Cutting Force Identification

The cutting forces in a given manufacturing process is considered to be proportional to the chip area by a constant known as the specific cutting force, K_s; see Eq. 1. To a first-order approximation, the value of the specific cutting force is dependent on the workpiece material. The tool geometry, cutting speed, and feed rate are known to have higher order effects on specific cutting force value.

Several methods may be used to develop a cutting force model for a given cutting operations. Thermo-visco-plastic constitutive laws, such as Johnson-Cook, may be used to predict the shear angles, strain rates, and temperatures associated with chip formation and,

therefore, the forces generated during cutting. These methods normally require high strain rate material testing using a compressive split-Hopkinson bar. Alternatively, cutting force model parameters may be obtained from historically tabulated data. A potential drawback is that the values of K_s also depend on the state of the material. That is, any heat treatment or method of cold work may affect the value. The following sections present a mechanistic approach to cutting coefficient identification for milling and turning operations.

5.1.1 Specific Cutting Force Identification for Turning

From Eq. 1, the total, instantaneous, cutting force, F, is proportional to the chip area, $A = bh$, by a single term referred to as the specific cutting force, K_s. The total cutting force can be decomposed into normal and tangential components, F_n and F_t, using F and the average cutting force angle, β:

$$F_n = \cos(\beta)\, F = K_s \cos(\beta) bh = \; k_n bh \tag{70}$$

$$F_t = \sin(\beta)\, F = K_s \sin(\beta)\, bh = \; k_t bh \tag{71}$$

The k_n and k_t terms are referred to as the normal and tangential cutting force coefficients. These terms can readily be measured by mounting the tool to a cutting force dynamometer, which decomposes the force experienced at the tool tip into three orthogonal force components. Figure 5.1 shows the experimental force measurement setup. A Kistler 9257B dynamometer is aligned with the axes of the machine and an orthogonal cut is taken from a cylindrical workpiece. Figure 5.2 shows an example of the normal and tangential cutting forces involved in a cutting test. Due to inherent flexibility in the system, the average of the measured forces was used in each calculation. With an average value for F_n and F_t, the

values for k_n, k_t, β, and K_s may be calculated. The total force presented in Figure 5.2 is the root sum square of the force components.

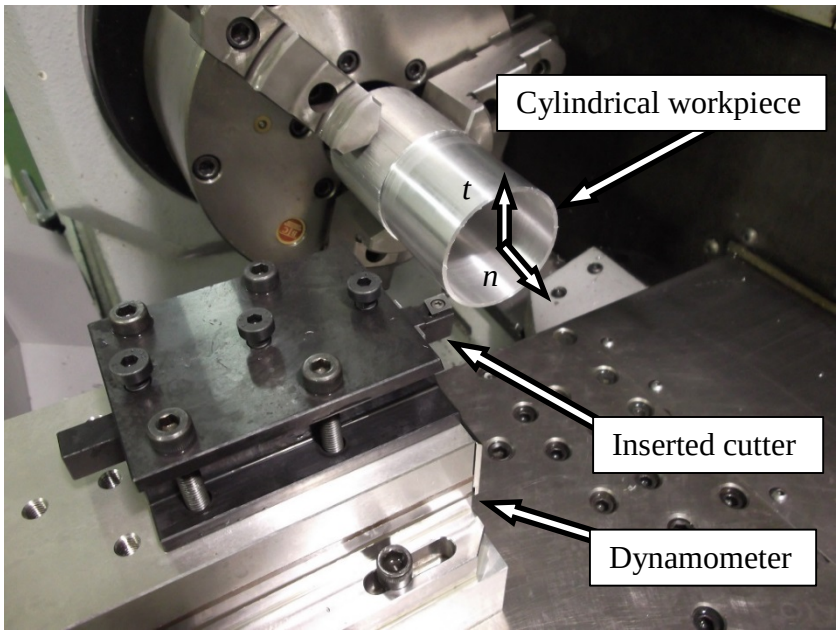

Figure 5.1: Force measurement setup for turning experiments using the Kistler 9257B dynamometer. The tangential and normal forces are measured during the cutting of a cylindrical workpiece in an orthogonal cut.

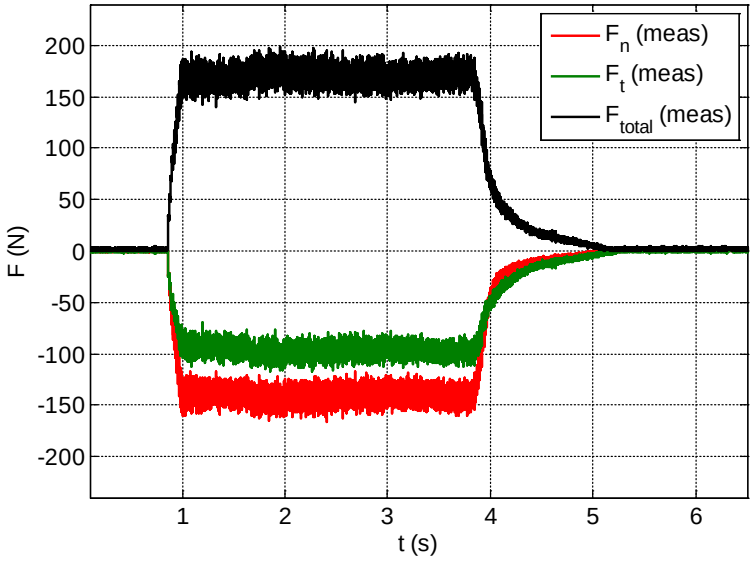

Figure 5.2: Normal and tangential cutting forces measured during orthogonal test cut.

5.1.2 Specific Cutting Force Identification for Milling

The forces generated during milling operations vary periodically with each rotation of the tool. For this reason, the method used to calculate the cutting force coefficients in turning cannot be used in milling. Instead, the cutting coefficients are determined via a linear regression using the average cutting forces measured by a dynamometer over a range of specified feed per tooth values. Figure 5.3 shows the force measurement setup for milling.

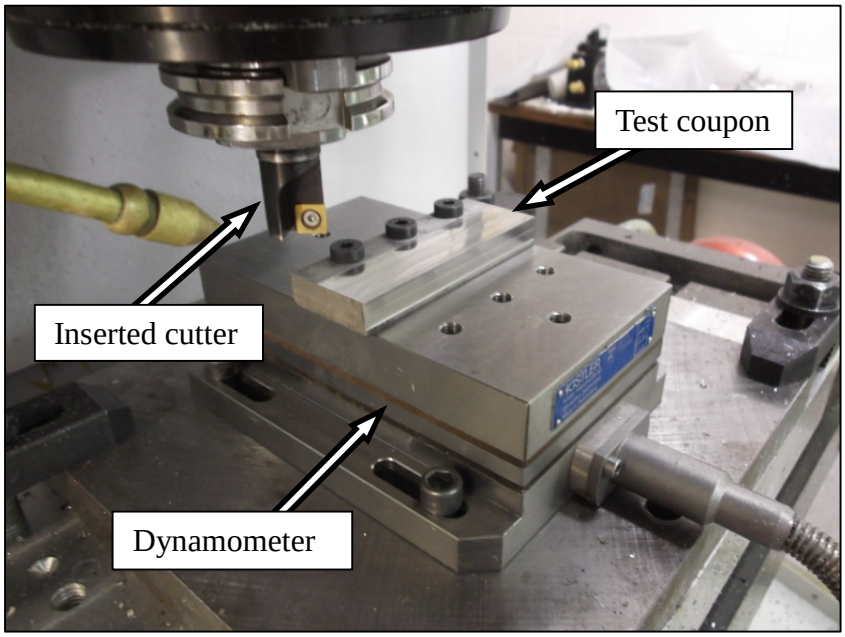

Figure 5.3: Cutting force measurement setup using a three component force dynamometer.

Schmitz [25] presents the method where the k_n and k_t terms can be calculated from the mean x and y force data. Figure 5.4 illustrates an example of the cutting forces obtained during a test cut using a single flute endmill.

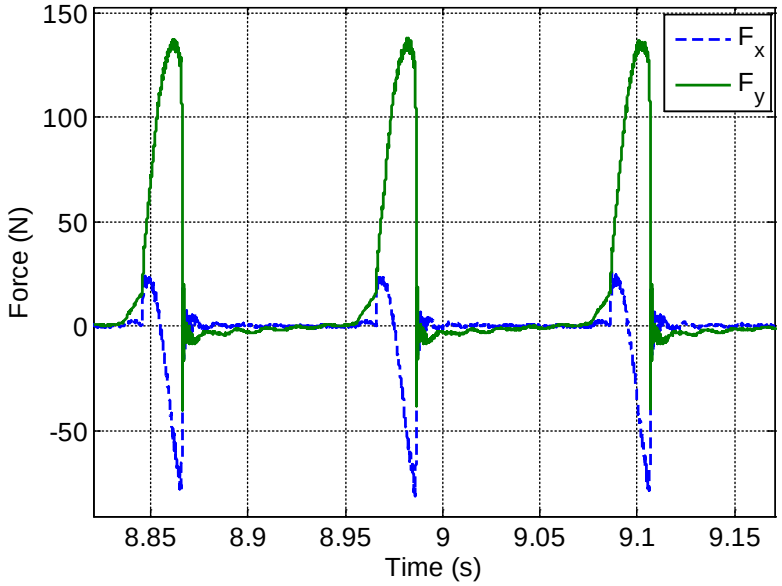

Figure 5.4: Example of cutting forces decoupled into *x* and *y*-directions for a 25% radial immersion test cut using a single-tooth endmill.

If the mean *x* and *y* force values, $\bar{F}_x$ and $\bar{F}_y$, are plotted versus a range of feed per tooth values, as illustrated in Figure 5.5, the cutting coefficients can be extracted from a linear regression fit using the expressions:

$$\bar{F}_x = \left[\frac{N_t b f_t}{8\pi}\left(-k_t \cos(2\phi) + k_n(2\phi - \sin(2\phi))\right)\right]_{\phi_s}^{\phi_e} \tag{72}$$

$$\bar{F}_y = \left[\frac{N_t b f_t}{8\pi}\left(-k_t(2\phi - \sin(2\phi)) + k_n \cos(2\phi)\right)\right]_{\phi_s}^{\phi_e} \tag{73}$$

From these expressions, it can be seen that cutting coefficient values can be calculated using the slopes from the linear fit and solving the system of equations. The specific cutting

force and cutting force direction can be calculated by $K_s = (k_t^2 + k_n^2)^{1/2}$ and $\beta = \tan^{-1}(k_t/k_n)$.

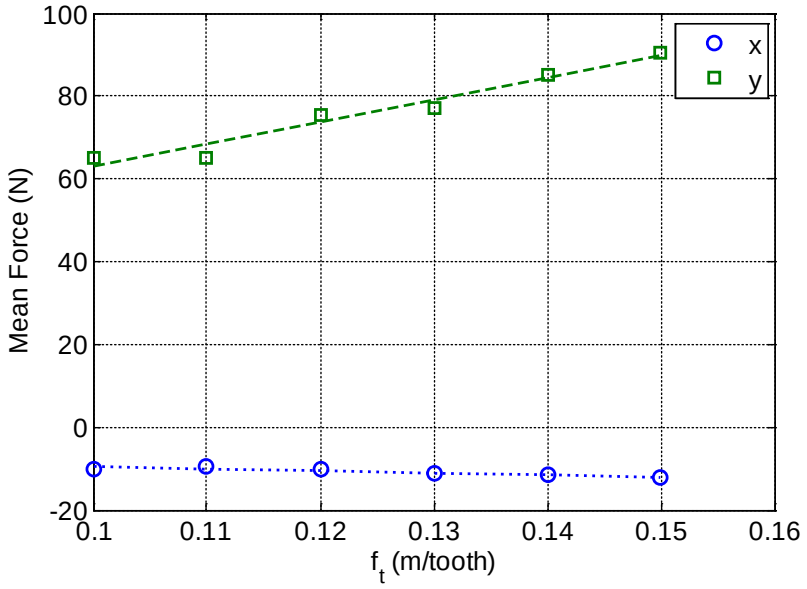

Figure 5.5: Linear regression results for mean *x* and *y* forces versus a range of feed per tooth values.

5.2 Tool Life Prediction and Modeling

Because the cutting tool naturally wears, particularly for the hard-to-machine materials considered in this work, a Taylor tool life model was established for each tool-material combination. Although more recent tool life models have been presented, Taylor's model was selected due to its widespread familiarity. The reason for obtaining tool life parameters was to establish an appropriate cutting speed range and avoid prohibitive tool wear for the selected tool-material combinations.

Tool life, *T*, is defined as the time required to obtain a predetermined wear level. Depending on the dominant wear mode, the wear level may be described using the flank wear width (FWW), crater depth, and/or notch depth. The Taylor tool life equation relates the tool life to the cutting speed using a power law model [26]:

$$VT^{n_t} = C_T$$

where n_T and C_T are empirical constants. The primary mode of tool wear in all cases in this work was flank wear; see Figure 5.6. In several test cases, the cutting force coefficients and process damping coefficient were identified under moderately worn conditions. To avoid removing the inserted tool from the spindle, a portable digital microscope was used to record the FWW at regular intervals as shown in Figure 5.7.

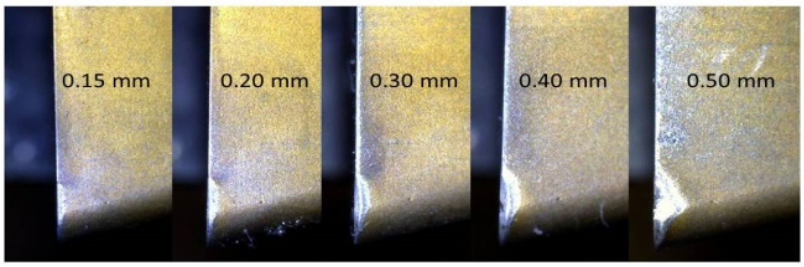

Figure 5.6: Sample measurements of the maximum FWW progression during wear tests.

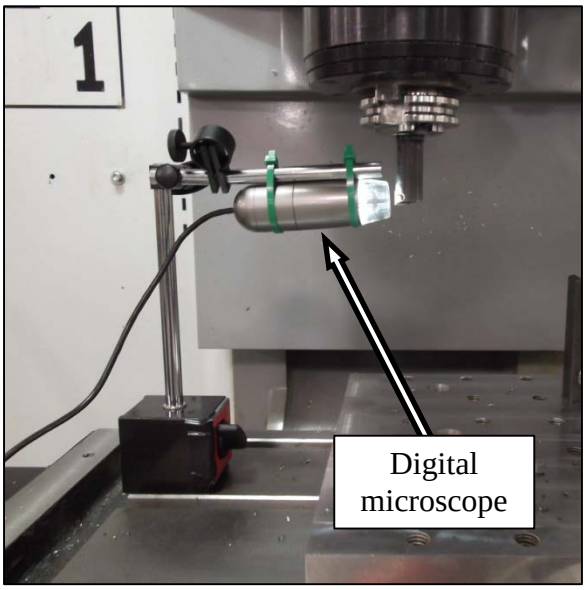

Figure 5.7: Setup for interrupted FWW measurements.

Tool wear testing was completed at specified cutting velocities and the tool life was defined as the time required to reach the maximum FWW of 400 μm. There was an

uncertainty in each FWW measurement due to the repeatability of the angular orientation of the microscope relative to the cutting edge. This variation proved to be negligible, but care was taken to ensure the cutting edge was approximately in the same angular orientation for each measurement. Figure 5.8 displays the FWW progression versus cutting time for Ti 6Al-4V. The 'o' symbols represent the intervals at which the FWW was recorded. In all cases, as expected, the wear rate was found to increase as cutting speed was increased.

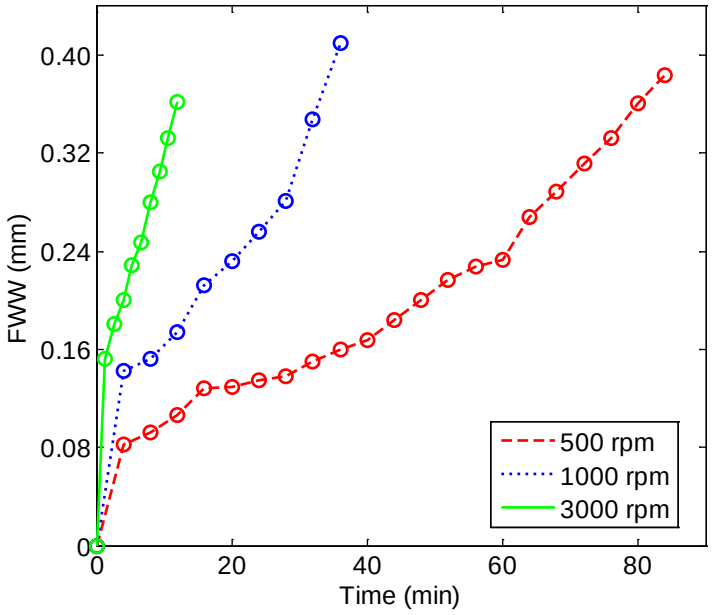

Figure 5.8: Increase in FWW with cutting time at three spindle speeds for Ti 6Al-4V.

The values for n_T and C_T were identified using a least squares curve fit to the (V, T) data points. The tool life (min) was plotted versus the cutting speed (m/s) and a power law curve was fit to the data. For example, Figure 5.9 displays the curve fit through the three data points for Ti 6Al-4V (R^2 = 0.97). It is observed that cutting operations are limited to

spindle speeds less than 1000 rpm if a tool life greater than approximately 30 minutes is desired. As a practical limit, this range of spindle speeds was used to select the operating speed range for process damping characterization.

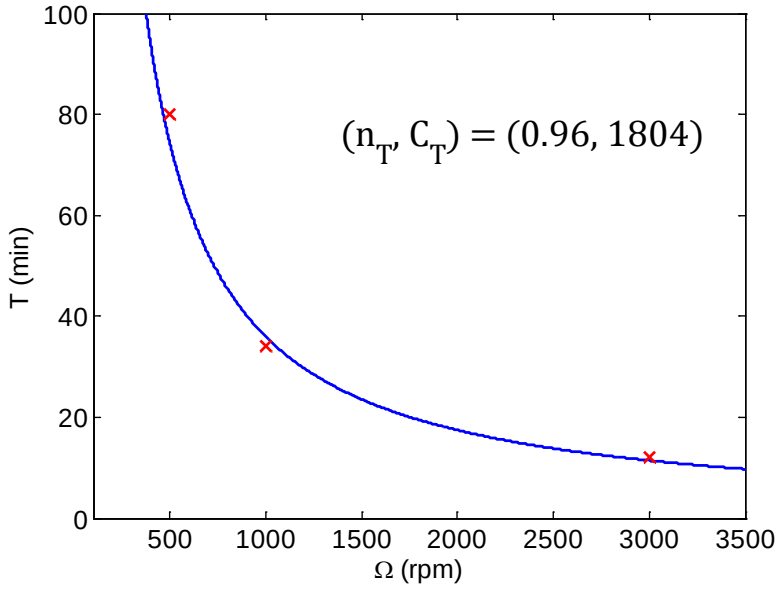

Figure 5.9: Taylor tool life model fit for Ti 6Al-4V.

5.3 Process Damping Coefficient Identification

The structural dynamics associated with various cutting operations can be complex and hard to model. For this reason, a series of compliant, flexure-based, structures of known and controllable dynamics were constructed to accurately identify the stability of an operation. Using each system of known dynamics, a grid of low-speed (chosen from the tool life operating range) test points was selected to investigate the process damping behavior. A multiple DOF notch-type flexural cutting tool was used to identify the process damping regime in turning. A single DOF and a two DOF flexible workpiece platform were each used to verify the process damping algorithm and identify process damping coefficient in milling for various hard-to machine metals. The following sections present

the methods used to identify the process damping coefficient for turning and milling operations.

5.3.1 Least RSS Method for Process Damping Coefficient Identification

Conventional linear stability analysis (i.e., C = 0 N/m) was first used to validate the stability behavior at higher speeds for the flexure setup. Using the experimental flexure modal parameters and cutting force coefficients, analytical stability lobes were generated without including the effects of process damping. Several test cuts were then chosen to confirm that key features predicted by the analytical lobes existed at higher spindle speeds. As seen in Figure 5.10, the predicted behavior was observed experimentally. Additionally, the critical limiting chip width, $b_{\text{lim,cr}}$, was identified to be approximately 1 mm for the 228 Hz SDOF milling setup; this result also agreed with the analytical prediction. A similar approach was used to validate the stability boundary for the 156 Hz single DOF setup, milling multi-DOF setup, and turning multi-DOF setup.

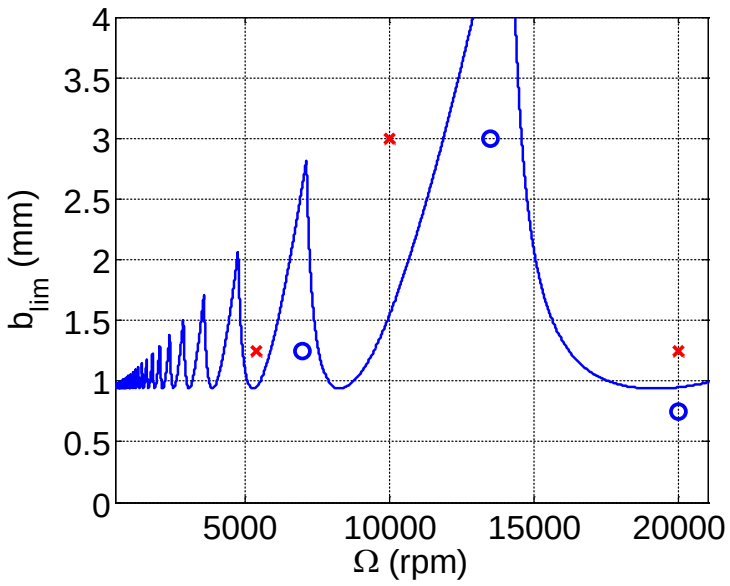

Figure 5.10: Stability lobe validation for the single DOF milling (f_n = 228 Hz) milling setup. Stable cuts (o) and unstable cuts (×) are identified.

A grid of test points at low spindle speeds was next selected to investigate the process damping behavior. Based on the stable/unstable cutting test results, a single variable residual sum of squares (*RSS*) estimation was applied to identify the process damping coefficient that best represented the experimental stability boundary; see Figure 5.11. The spindle speed-dependent experimental stability limit, b_i, was selected to be the midpoint between the stable and unstable points at the selected spindle speed. The sum of squares of residuals is given by Eq. 74, where $f(\Omega_i)$ is the analytical stability boundary and *n* is the number of test points.

$$RSS = \sum_{i=1}^{n} (b_i - f(\Omega_i))^2 \tag{74}$$

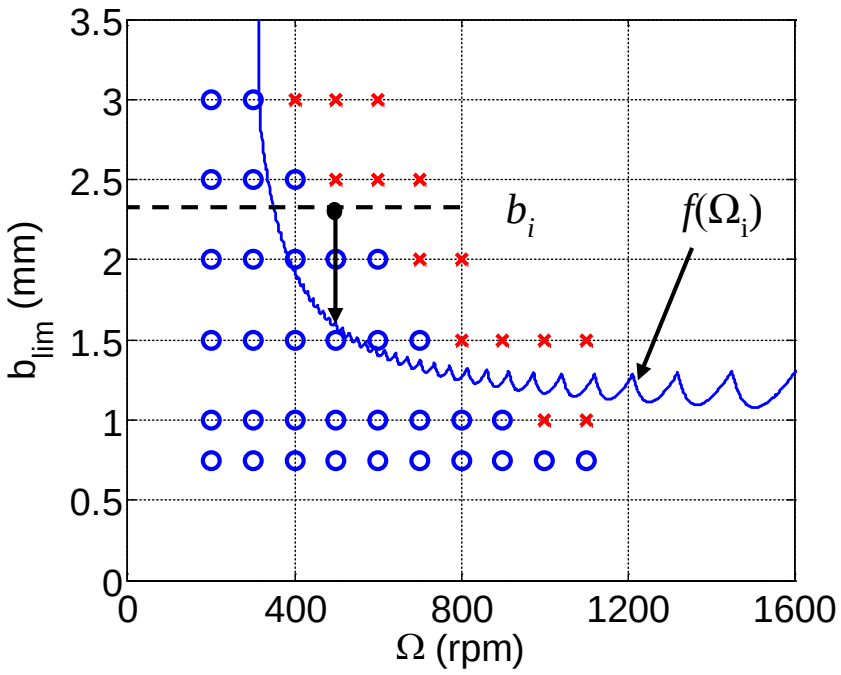

Figure 5.11: Description of variables for RSS estimate of process damping coefficient.

A range of process damping coefficients was selected and the *RSS* value was calculated for each corresponding stability limit; see Figure 5.12. The *C* value that corresponded to the minimum *RSS* value was selected to identify the final stability boundary for all test conditions. The following sections present the methods for process damping coefficient identification for the milling and turning setups.

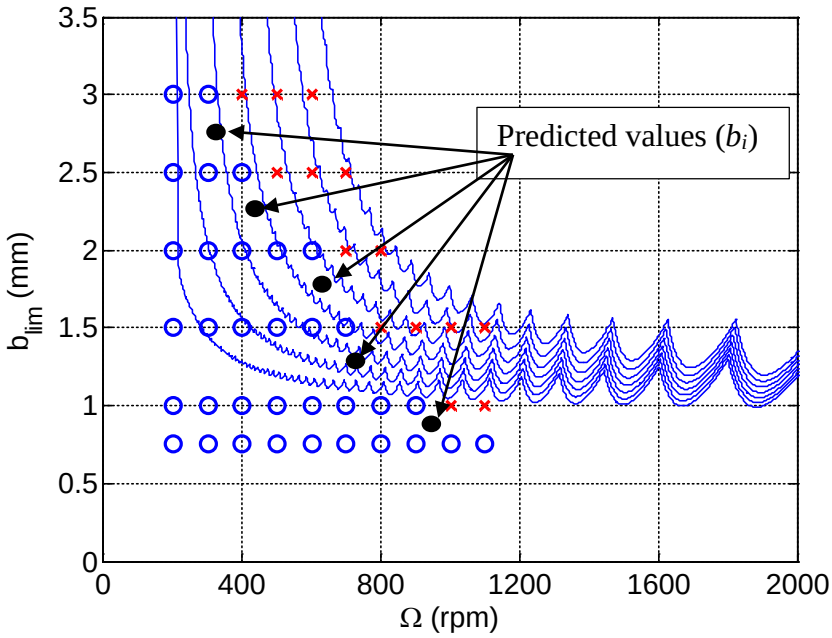

Figure 5.12: Sweep of process damping coefficients used to select final stability boundary

5.3.2 Process Damping Coefficient Identification for Turning Setup

The experiments to identify the process damping coefficient and verify the algorithm presented in Chapter 3 were carried out on a Haas TL-1 CNC lathe. A custom notch hinge flexible cutting tool was designed to provide a repeatable multi-DOF system in the feed direction of the cutting operation; see Figure 5.13. The notch-hinge geometry was designed

to produce two comparable stiffness bending modes at natural frequencies sufficiently spaced apart. The intent for this design was to produce stability lobes with what are known as “competing lobes”. The cutting insert (Sandvik CCMW32.51H13A) was uncoated with a 7° relief angle, 0° rake angle, and no chip-breaker. The method used to design the flexible cutting tool is presented in Appendix A.

In order to isolate the workpiece dynamics from the cutting process, a tubular geometry was selected in which the feed direction was parallel to the length of the tube. In this arrangement, the stiffness of the workpiece was much greater than that of the cutting tool. Because the flexure compliance was much higher than the workpiece specimen in the feed direction, the stability analysis was completed using the flexure’s dynamic properties. The frequency response function and modal parameters for the flexure in the feed and tangential directions are provided in Figure 5.14 and Table 5.1.

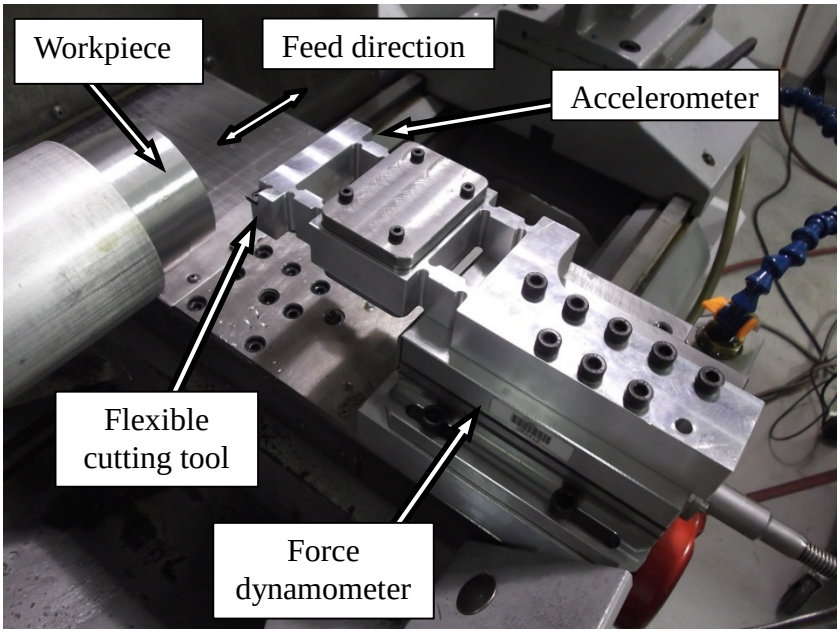

Figure 5.13: Experimental setup for turning stability tests. A cutting force dynamometer and accelerometer (not shown) were used to monitor the tool vibration during cutting.

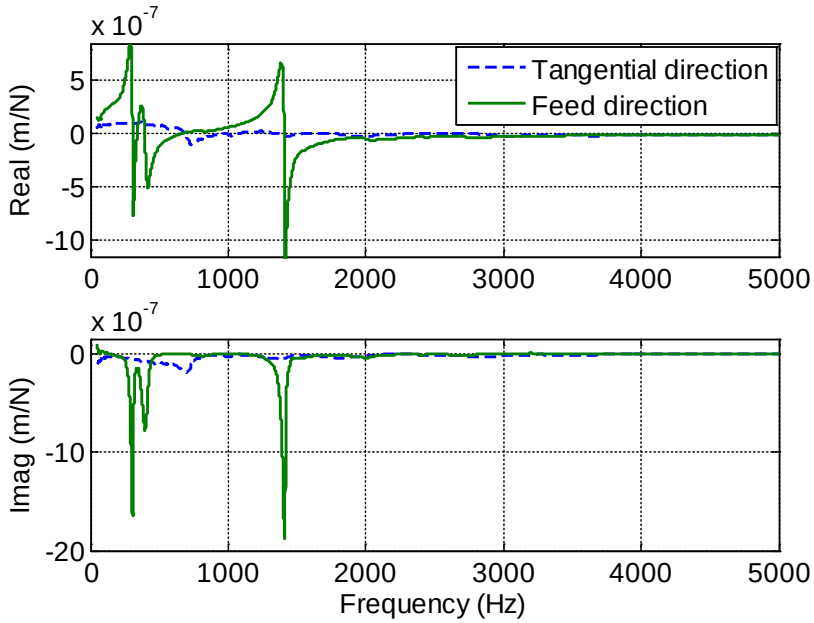

Figure 5.14: Frequency response function of flexible cutting tool in tangential and feed directions.

Table 5.1: Modal parameters for flexible cutting tool setup

Direction	Viscous damping ratio (%)	Modal stiffness ($\times 10^7$ N/m)	Natural frequency (Hz)
Tangential	7.21	3.71	703
Feed	3.56	0.85	304
	5.46	1.17	394
	0.99	2.69	1410

The stability of a selected test cut was identified in several ways. An accelerometer (PCB Piezotronics model 352B10) and cutting force dynamometer (Kistler model 9257B) were used to monitor the cutting operations. The level of vibration and forces during each test cut as well as the frequency content were used to establish stable/unstable performance.

Also, qualitatively, the machined surface finish after each test cut was inspected using a digital microscope.

5.3.2.1 Vibration Measurements for Turning

Figure 5.15 illustrates an example stability lobe diagram and test cut results for the flexure setup. Points A-C were selected to describe the characteristics of stable and unstable cutting conditions. Figure 5.16 displays the force and acceleration signals for point A at a spindle speed of Ω=300 rpm and chip width of b=3 mm. It is observed that the forces generated for this stable cut remained steady at a mean of approximately 364 N with no apparent growth or instability in the time domain. The frequency content of the force and accelerometer signals at point A reveal slight, but not distinct, peaks near the flexure's natural frequencies; Table 5.1.

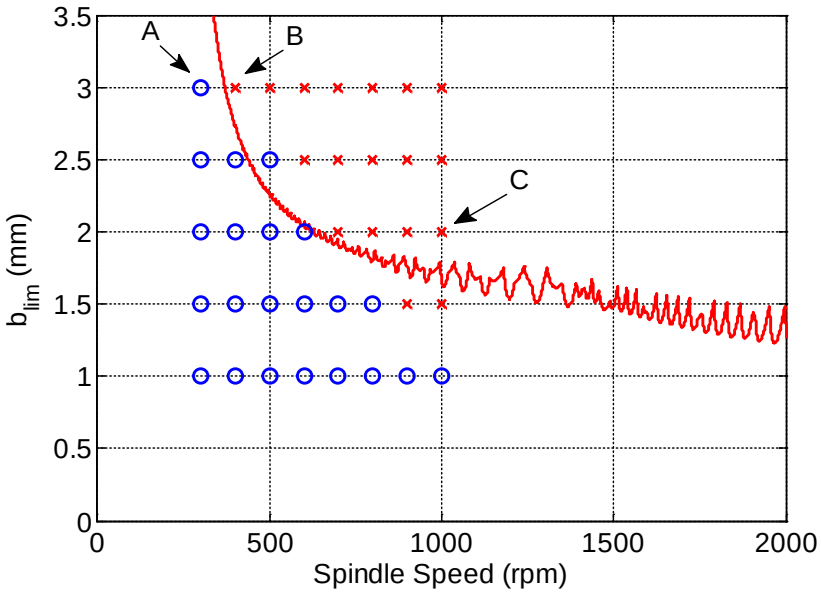

Figure 5.15: Stability boundary for the multi-degree of freedom system with the grid of stable (o) and unstable (x) cutting tests identified.

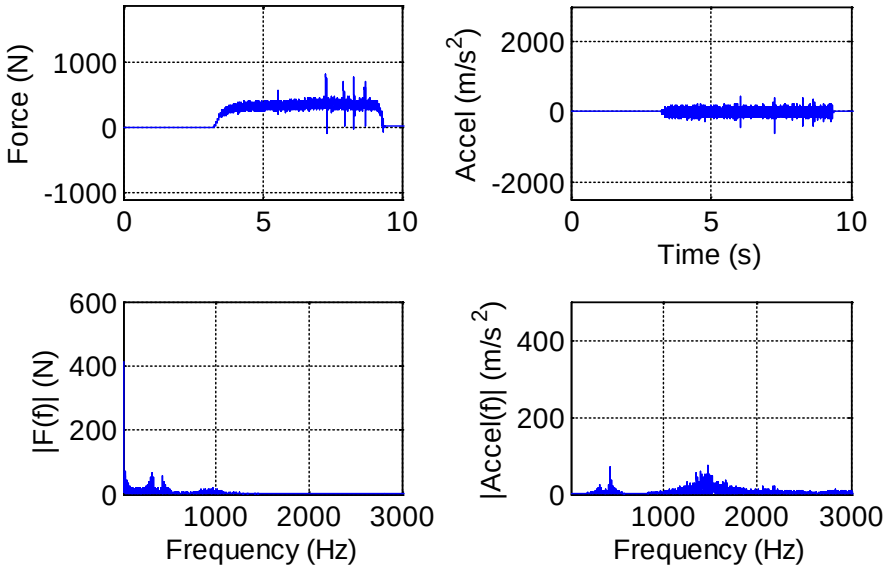

Figure 5.16: Cutting force and accelerometer time domain signals in the feed direction for the stable point A {300 rpm, 3.0 mm} with corresponding frequency content below.

Point B in Figure 5.15 presents an example of a low-speed, unstable cutting operation. The spindle speed is $\Omega = 400$ rpm, and the chip width is $b = 3$ mm. Figure 5.17 shows the force and vibration measurements for this unstable operation. A substantial increase in force and acceleration is observed after approximately one second of the total time in the cut. The fundamental chatter frequency is measured to be near the frequency corresponding to the first bending mode of the flexible tool, $f_c = 310$ Hz.

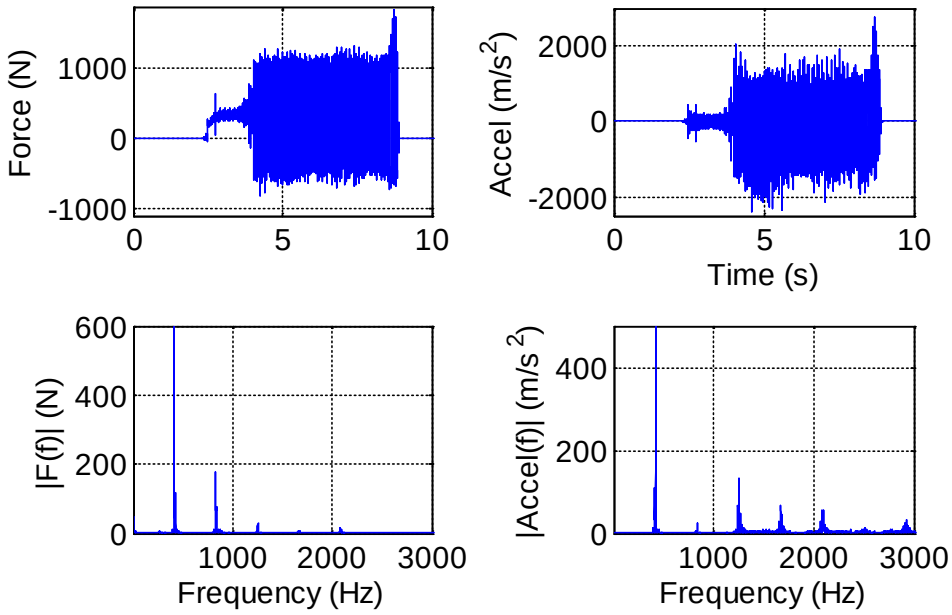

Figure 5.17: Cutting force and accelerometer time domain signals in the feed direction for the unstable point B {400 rpm, 3.0 mm}, with corresponding frequency content below. The chatter frequency is approximately 310 Hz.

Point C in Figure 5.15 is another example of unstable cutting conditions. The test was conducted at a spindle speed $\Omega = 100\,rpm$ and chip width, $b = 2\,mm$. An increase in the cutting velocity shifts the chatter frequency to a frequency near the second bending mode of the flexible cutting tool, $f_c = 1493\,Hz$. In the time domain, it is also observed that the higher frequency oscillating force is lower in magnitude than the unstable cuts oscillating at the lower chatter frequencies.

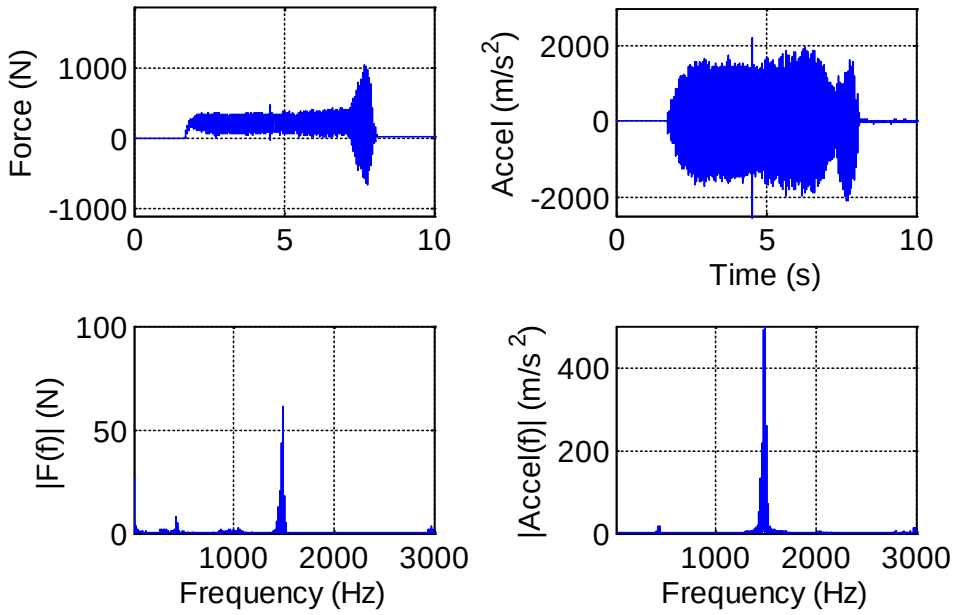

Figure 5.18: Cutting force and accelerometer time domain signals in the feed direction for the unstable point B {1000 rpm, 2.0 mm} with corresponding frequency content below. The chatter frequency is approximately 1493 Hz.

5.3.2.2 Surface Roughness and Chip Morphology for Turning

In most industrial cutting operations, the relative vibration between the cutting tool and workpiece surface dictates the part surface finish. Figure 5.19 presents the surface finish and chip morphology of a typical stable cutting operation. The digital microscope image in Figure 5.19b represents a cut surface with very little discernable surface defects. The chips produced from this type of cut are smooth and continuous due to the absence of a chip breaker, see Figure 5.19c.

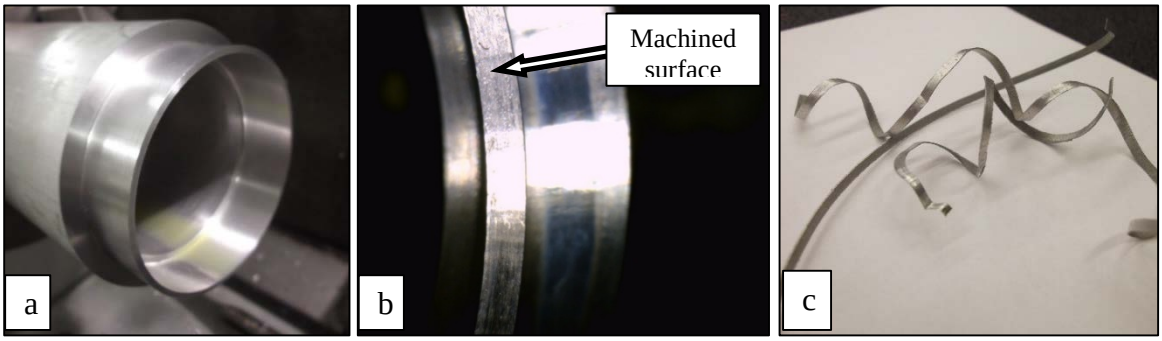

Figure 5.19: Surface roughness and chip morphology of stable test cut.

Figure 5.20 depicts the surface finish and chip morphology of a clearly unstable cutting test. From the digital microscope image in Figure 5.20b, there are large undulations remaining on the workpiece surface. The chips produced from an unstable test cut contain similar undulations and, in cases of large enough vibrations, are discontinuous from the cutter leaving the surface of the workpiece, see Figure 5.20c. Such cutting conditions are known to have a negative influence on tool life, the machine tool, and workpiece quality.

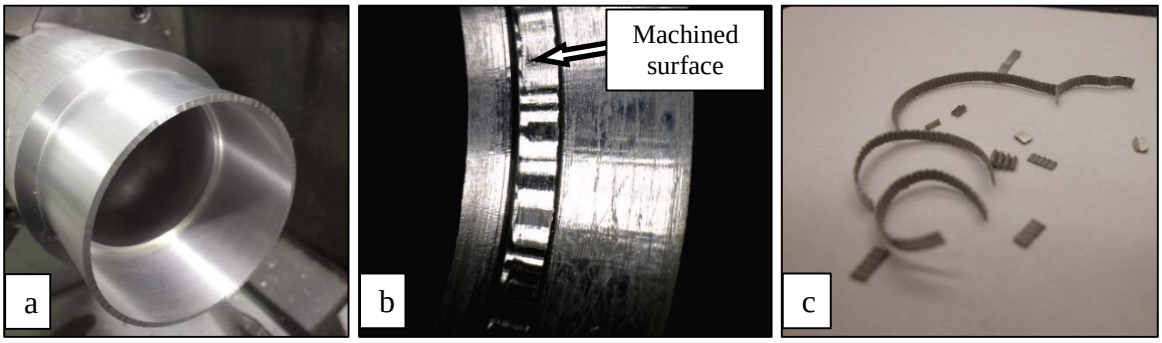

Figure 5.20: Surface roughness and chip morphology of unstable test cut.

5.3.3 Process Damping Coefficient Milling Setup

The procedure for obtaining the process damping coefficient for milling is provided in this section. Cutting tests were performed on both single and two DOF flexural cutting platforms to validate the algorithm. Because the compliances of the flexures were much higher than the tool-holder-spindle-machine, the stability analysis was completed using only the flexures' dynamic properties. The stability limit was identified over a grid of axial depth of cut and spindle speed pairs. Using the experimental stability boundary, the process damping coefficient was then identified. The effects of insert relief angle and tool wear on the process damping coefficient were examined. The flexure dynamics were also adjusted to determine the sensitivity of the coefficient to changes in the system dynamics.

5.3.3.1 Single Degree of Freedom Experimental Setup

The experimental setup used a parallelogram leaf-type flexure in order to control the dynamics of the system and approximate single degree of freedom behavior. The flexure was constructed to provide a flexible foundation for individual workpieces/coupons. Figure 5.21 shows the full experimental setup for the single DOF cutting tests. The dimensions of the flexure were chosen so that the flexibility of the platform was much greater than that of the cutting tool. The flexure leafs were selected to be 3.13 mm thick AISI 6061 aluminum sheets. An AISI 1080 steel sheet was used as the top platform to increase the mass of the flexible system. The entire system was fixed to the machine table using T-slot nuts. An accelerometer was also mounted to the flexure platform to provide in-process data for stability evaluation.

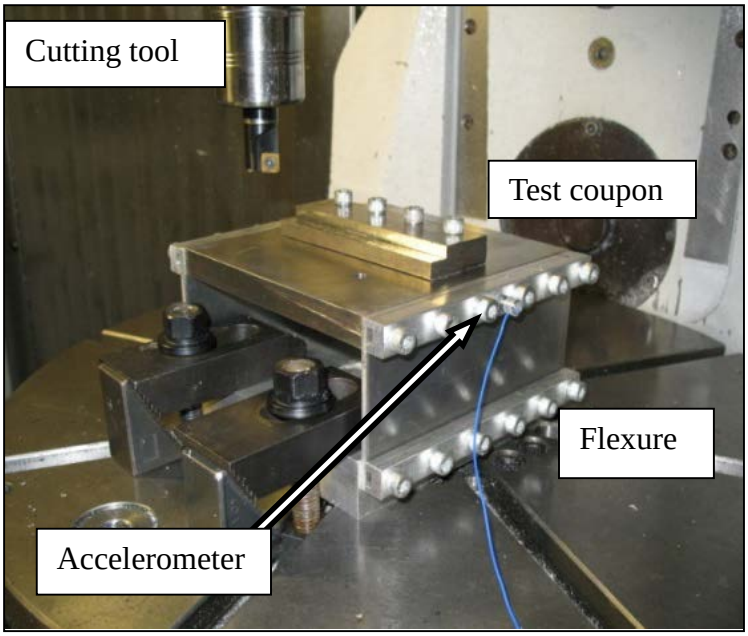

Figure 5.21: Single degree of freedom setup for milling stability tests and process damping coefficient identification.

To study the influence of relief angle on the process damping behavior, two single-tooth indexable square endmills of similar diameter were used. The first was an 18.54 mm diameter inserted endmill (Kennametal model KICR-0.73-SD3-033.3C) with a 15° relief angle (SDCW322 KC725M). The second was a 19.05 mm diameter endmill (Cutting Tool Technologies model DRM-03) with an 11° relief angle insert (SPEB322 KC725M). Both cutting tools had a zero degree rake angle. The inserts had no edge preparation and similar TiAlN coatings. The tools were placed in a Schunk Tribos® holder with an overhang length of approximately 55.0 mm. Individual workpieces, or test coupons, were bolted on the flexure so that test cuts could be completed at any specified radial immersion. A preliminary frequency response function for the single degree of freedom setup was obtained by impact testing the flexure setup with an uncut test part mounted to the top. FRFs for the stiff direction of the flexure and the tool (both *x* and *y* directions) were also

obtained in order to confirm that they were much stiffer than the intended flexible direction for the flexure. Measurements showed the peak imaginary amplitudes for the tool response were approximately ten-times smaller than the intended flexure direction and were, therefore, considered negligible when modeling the dynamic system; see Figure 5.22.

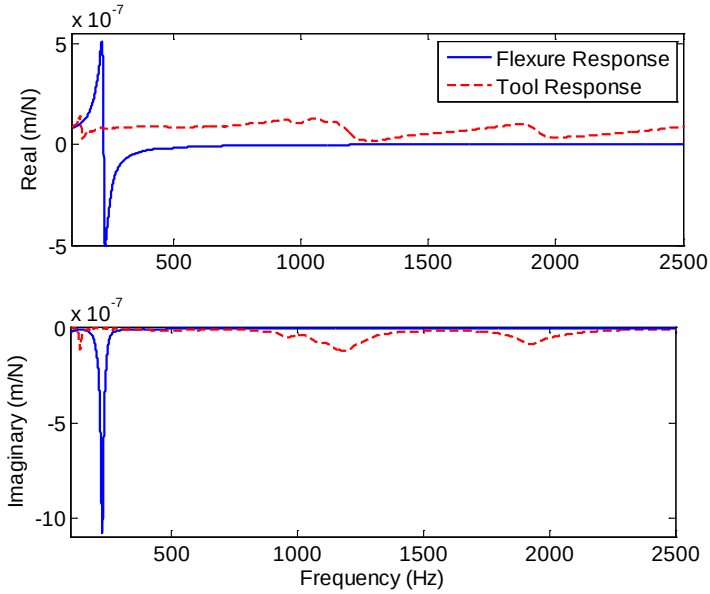

Figure 5.22: Frequency response function comparison of single DOF flexure and cutting tool in machine spindle (*x* and *y* directions were similar).

The sensitivity of the process damping coefficient to changes in the system dynamics was also evaluated in this study. The dynamics of the system were altered by adding mass to the flexure platform. The added mass decreased the natural frequency by approximately 32%. The modal parameters for both cases are provided in Table 5.1. The *x* and *y* directions correspond to flexible and stiff directions of the flexure, respectively, where *x* is the feed direction of the milling cutter.

Table 5.2: Modal parameters for single DOF flexure with and without mass.

	Direction	Modal stiffness (N/μm)	Viscous damping ratio (%)	Natural frequency (Hz)
No mass	*x*	2.77	6.3	228
	y	174	3.7	1482
Added mass	*x*	4.37	1.8	156
	y	276	2.8	1137

A piezoelectric accelerometer (PCB Piezotronics model 352B10) was used to measure the vibration during cutting. The frequency content of the accelerometer signal was used in combination with the machined surface finish to establish stable/unstable performance. Cuts that exhibited uniform vibration in the time-domain and exhibited content in the frequency-domain at the associated tooth passing frequency and its harmonics were considered to be stable. Figure 5.23 and Figure 5.24 represent an example stable test in the time and frequency domain, respectively.

Alternatively, cuts that exhibited vibrations which increased significantly over the duration of the cut and showed significant frequency content near the flexure's *x* direction natural frequency were considered to be unstable. Figure 5.25 and Figure 5.26 represent an unstable cutting condition in the time and frequency domains, respectively.

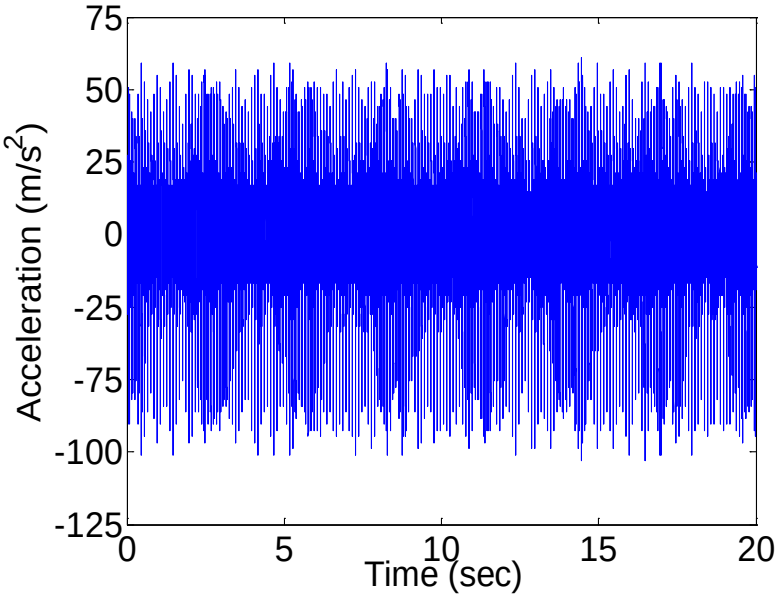

Figure 5.23: Time domain acceleration signal of a stable cut.

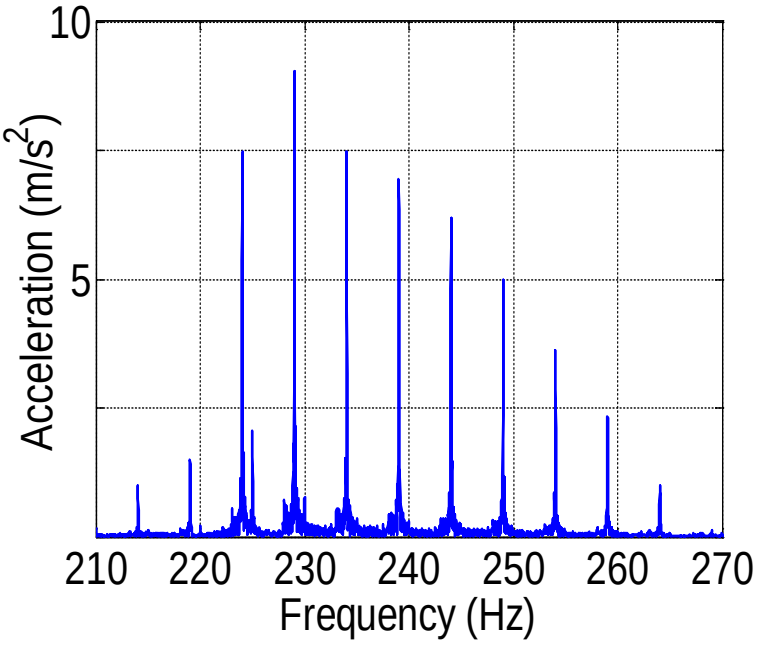

Figure 5.24: Frequency domain signal of a stable cut performed by a single-tooth cutter at 300 rpm (5 cps).

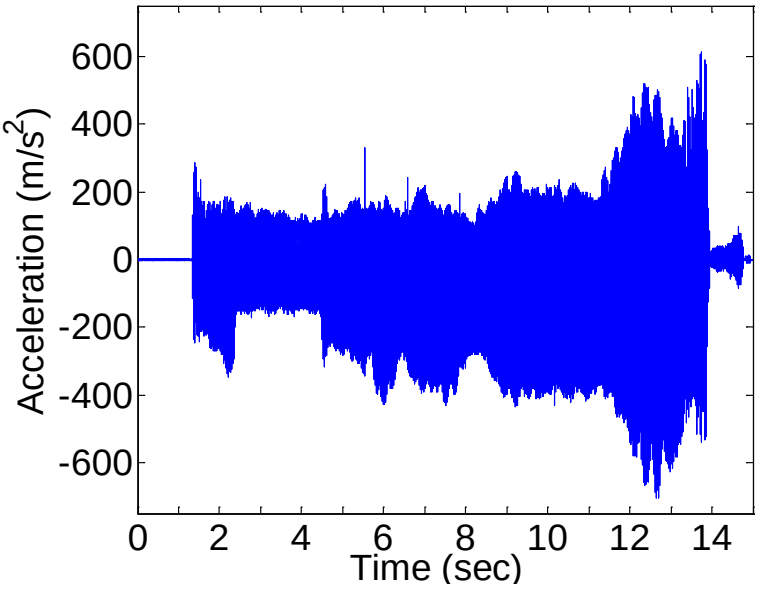

Figure 5.25: Time domain signal of an unstable cutting performance.

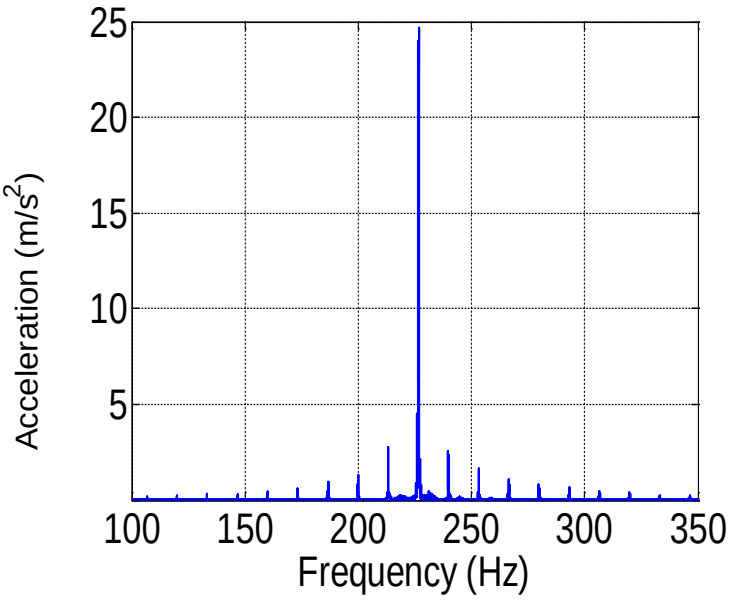

Figure 5.26: Frequency domain signal of an unstable cutting performance. Strong frequency content is observed at the flexure's 228 Hz natural frequency for the test completed at 700 rpm (11.7 cps).

In addition to vibration measurements, the surface of the workpiece was analyzed visually after each test cut. Qualitatively, the surface texture of a stable cut exhibited very few surface flaws, shown in Figure 5.27. Inspection of the workpiece surface for an unstable cut revealed irregular vibratory flaws in the finish due to the self-excited cutter vibration; see Figure 5.28.

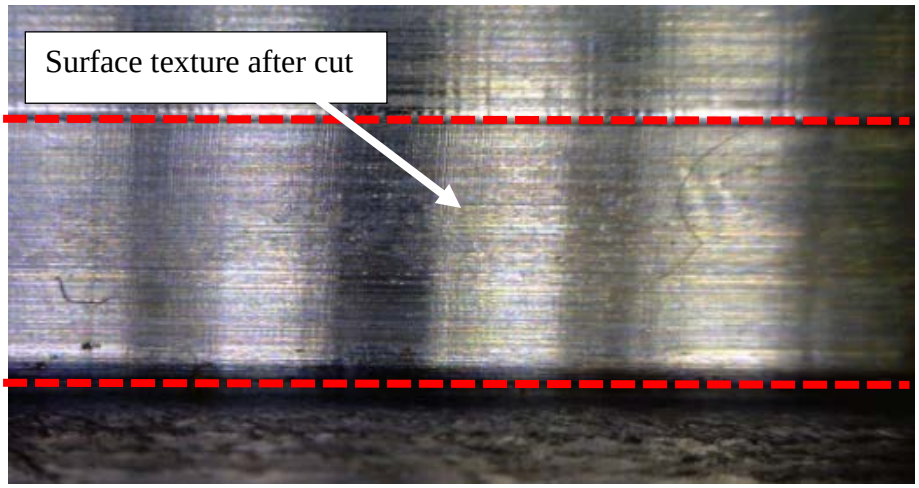

Figure 5.27: Surface finish of workpiece after a stable cut.

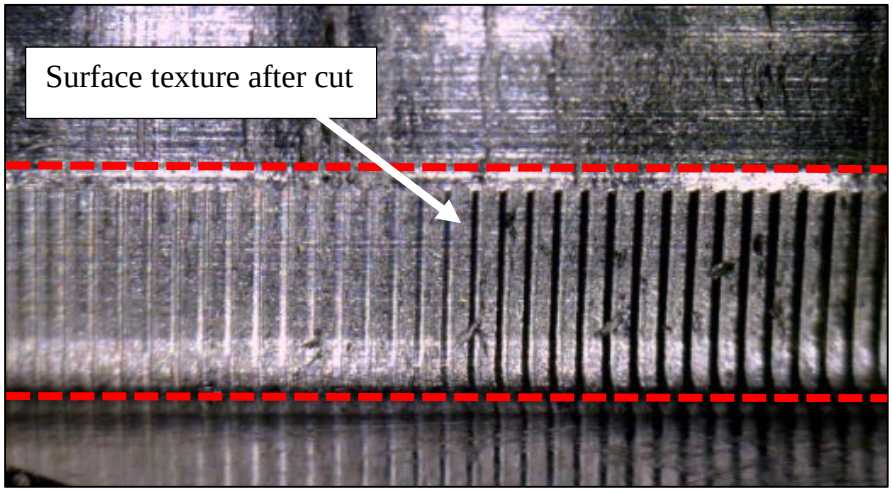

Figure 5.28: Surface finish of workpiece after an unstable cut.

5.3.3.2 Multi-DOF Experimental Setup

To validate the multiple DOF process damping model for milling, low-speed cutting tests were performed and a process damping coefficient was calculated. Experiments were performed on a Haas TM-1 CNC milling machine. A custom-designed notch hinge flexure, pictured in Figure 5.29, was designed; placing a small workpiece upon this flexure provided a repeatable two DOF system along the feed direction. To negate the effects of tool dynamics, tool corner radius effects, and interaction between the tool end and the floor of a just-machined slot, a fin geometry was selected for the workpiece. Using this configuration, analogous to the tube turning experiments presented in Section 5.3.2, the tool is much stiffer than the workpiece/flexure system. The fin is flexible in the *z* direction, but the tool used had a zero degree helix angle, so the *z* direction force is negligible.

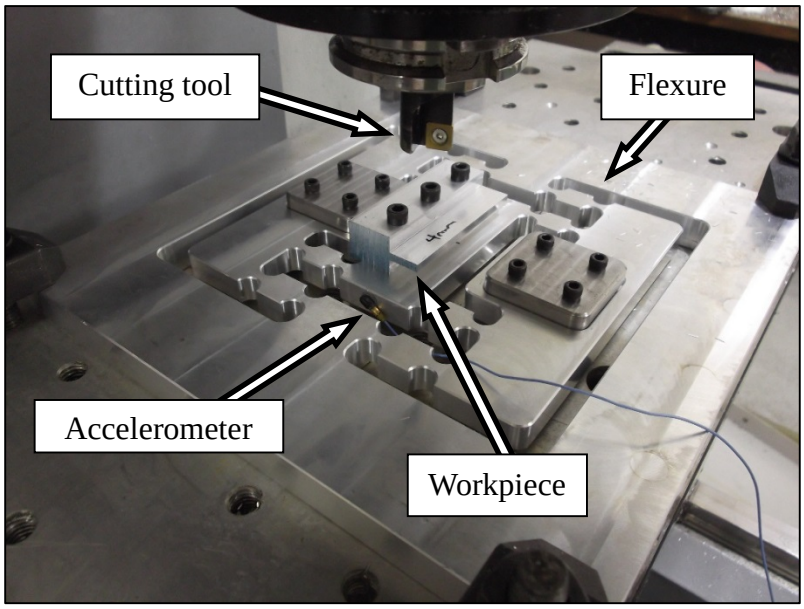

Figure 5.29: Experimental setup for two DOF milling stability tests. An accelerometer was used to monitor the flexure vibration during machining.

Because the flexure is intentionally more compliant than the tool along the feed direction, the stability analysis is performed using the modal parameters of the flexible system. Table 5.3 and Figure 5.30 provide the modal parameters and the frequency response function of the workpiece/flexure system along the feed (*x*) and tangential (*y*) directions, oriented as shown in Figure 5.29. The stability of individual test cuts was identified according to vibration and surface finish characteristics described in the single DOF milling experimental setup

Table 5.3: Modal parameters for two DOF flexible workpiece setup.

Direction	Viscous damping ratio (%)	Modal stiffness ($\times 10^7$ N/m)	Natural frequency (Hz)
Tangential	1.82	4.208	1678
Feed	0.37	0.814	515
	0.14	2.871	1408

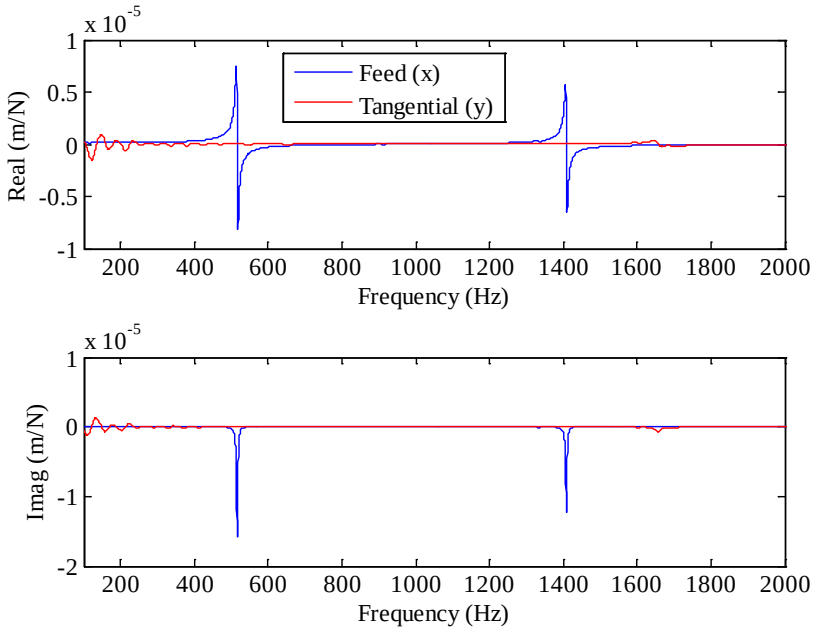

Figure 5.30: Frequency response function of flexible system in feed (*x*) and tangential (*y*) directions.

CHAPTER 6: EXPERIMENTAL RESULTS AND DISCUSSION

Experiments were conducted using all three setups described in Chapter 5 to observe the process damping behavior and subsequent stability increase at low cutting speeds. The bulk of the work described involves the single DOF milling setup. A single DOF setup simplifies the manner in which chatter is identified. Using the SDOF setup, quantitative effects of clearance angle, flank wear width (FWW), and change in dynamics were evaluated using the process damping coefficient identification method previously described. A database of process modeling coefficients for AISI 1018 steel, 6061-T6 aluminum, Ti 6Al-4V, AISI 304 stainless steel, and Inconel 718 is also presented in this section. The database includes coefficients for the process damping model, specific cutting force, and Taylor tool-life model. For the multi DOF turning and milling setups, preliminary results include process modeling coefficients for 6061-T6 aluminum.

6.1 Experimental Identification of the Process Coefficients for SDOF Milling

The specific cutting force, process damping coefficient and tool-life parameters were experimentally identified and tabulated for the following materials: AISI 1018 steel, Ti 6Al-4V, AISI 304 stainless steel, and Inconel 718. The process damping coefficients were collected using the single DOF flexure setup. The influence of relief angle on the process coefficients were observed using two single tooth indexable square endmills of similar diameter. The first was an 18.54 mm diameter endmill (Kennametal model KICR-0.73-SD3-033.3C) with a 15° relief angle (SDCW322 - KC725M). The second was a

19.05 mm diameter endmill (Cutting Tool Technologies model DRM-03) with an 11° relief angle insert (SPEB322 KC725M). Both cutting tools had a zero degree rake angle. The inserts had no edge preparation and similar TiAlN coatings. The tools were placed in a Tribos® holder with an overhang length of approximately 55 mm.

6.1.1 AISI 1018 Steel Process Coefficients for SDOF

6.1.1.1 AISI 1018 Steel Cutting Force Coefficients

The cutting force coefficients were identified under stable cutting conditions using a cutting force dynamometer (Kistler model 9257B). The cutting tests were performed as described in Chapter 5.1 using a spindle speed of 500 rpm, an axial depth of cut of 3 mm, and a feed per tooth range of 0.05-0.25 mm/tooth. A linear regression to the mean cutting force over a series of tests at the selected feed per tooth values was used to identify the cutting force model values. The tests were completed three times and the average values were used in the following stability characterization. The results of the three trials are provided in Table 6.1 .

Table 6.1: Cutting force parameters for the 18.54 mm diameter, 15° relief cutter with low insert wear (FWW <100 µm).

Trial	k_t (N/mm^2)	k_n (N/mm^2)	K_s (N/mm^2)	β (deg)
1	2133.7	1043.3	2375.1	63.9
2	2024.1	1030.5	2271.3	63.0
3	2176.0	1084.0	2431.1	63.5
Mean	2111.3	1052.6	2359.1	63.5
Std. dev.	78.4	27.9	81.1	0.45

Table 6.2: Cutting force parameters for the 19.05mm diameter, 11° relief cutter with low insert wear (FWW <100 μm).

Trial	k_t (N/mm^2)	k_n (N/mm^2)	K_s (N/mm^2)	β (deg)
1	2205.5	1142.4	2483.8	62.6
2	2353.7	1219.6	2650.9	62.7
3	2145.2	1202.7	2459.3	60.7
Mean	2234.8	1188.2	2531.3	62.0
Std. dev.	87.6	40.6	104.3	1.1

For the 18.54 mm diameter cutter, the mean specific cutting force, K_s, and cutting force direction, β, were determined to be 2359.1 N/mm^2 and 63.5°, respectively. For the 19.05 mm diameter cutter, the mean values were K_s = 2531.0 N/mm^2 and β = 62.0°. For moderately worn insert conditions (0.150 μm < FWW < 0.250 μm) the mean specific cutting force and cutting force direction were K_s = 2441.0 N/mm^2 and β = 63.5° for the 18.54 mm diameter cutter and K_s = 2550.2 N/mm^2 and β = 62.0° for the 18.54 mm diameter cutter. There was an observed increase, though slight, from the low wear to moderately worn cases in the cutting force testing of each material selected.

6.1.1.2 AISI 1018 Steel Process Damping Coefficients

Conventional linear stability analysis (i.e., C = 0 N/m) was first used to validate the stability behavior at higher speeds for the SDOF flexure setup. Using the experimental flexure modal parameters and cutting force coefficients, analytical stability lobes were generated without including the effects of process damping. Several test cuts were then chosen to confirm that key features predicted by the analytical lobes existed at higher spindle speeds. As seen in Figure 6.1, the predicted behavior was observed experimentally. Additionally, the critical limiting chip width, $b_{\text{lim,cr}}$, was identified to be approximately 1.0 mm for the 228 Hz flexure setup; this result also agreed with the analytical prediction. A

similar approach was used to validate the stability boundary for the 156 Hz setup. The critical stability limit was approximately 0.4 mm for this case; see Figure 6.2.

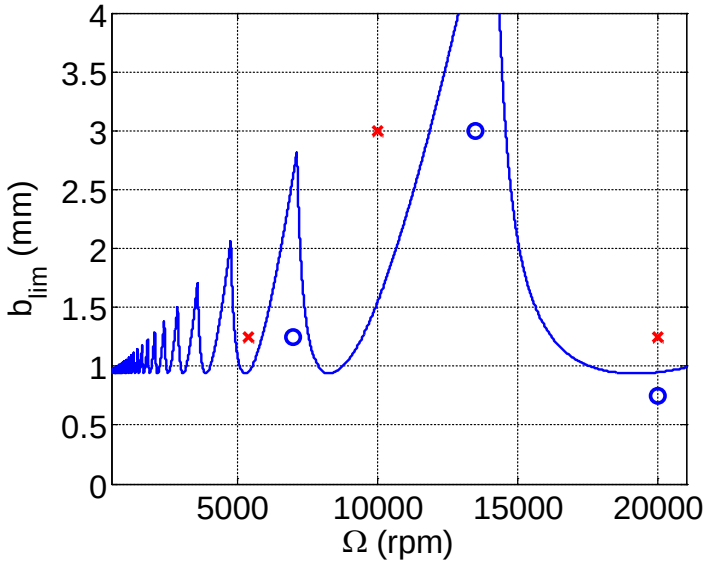

Figure 6.1: Stability lobe validation for the 228 Hz setup. Stable cuts (o) and unstable cuts (×) are identified.

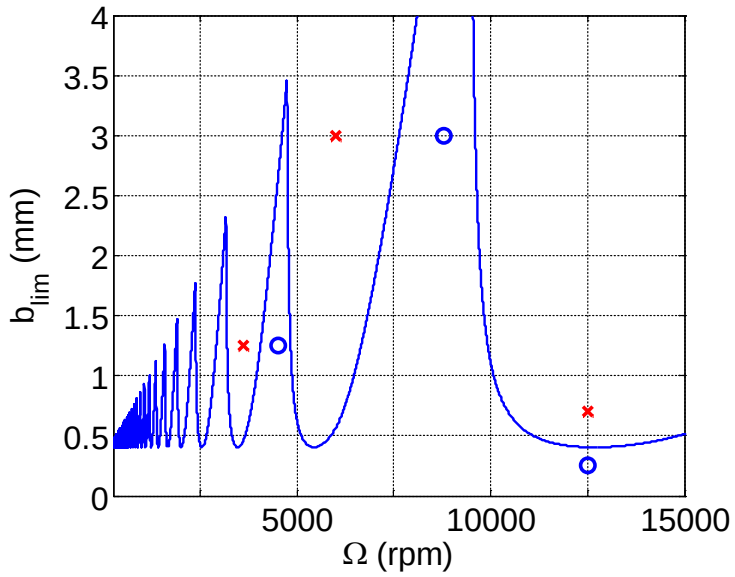

Figure 6.2: Stability lobe validation for the 156 Hz setup. Stable cuts (o) and unstable cuts (×) are identified.

A preselected grid of axial depths was chosen at low spindle speeds to identify the process damping regime for AISI 1018 steel. Stability testing was first performed for the 18.54 mm diameter, 15° relief angle end mill. The axial depths ranged from below the confirmed $b_{\text{lim,cr}}$ value of 1 mm to a maximum depth of 3 mm. All cuts were performed using 50% radial immersion up-milling conditions. The feed per tooth was also held constant at 0.05 mm/tooth. Using the minimum *RSS* method described in Chapter 5, a process damping coefficient of $C = 1.25\times10^5$ N/m was found to best fit the data for the 228 Hz system. The corresponding stability boundary is provided in Figure 6.3.

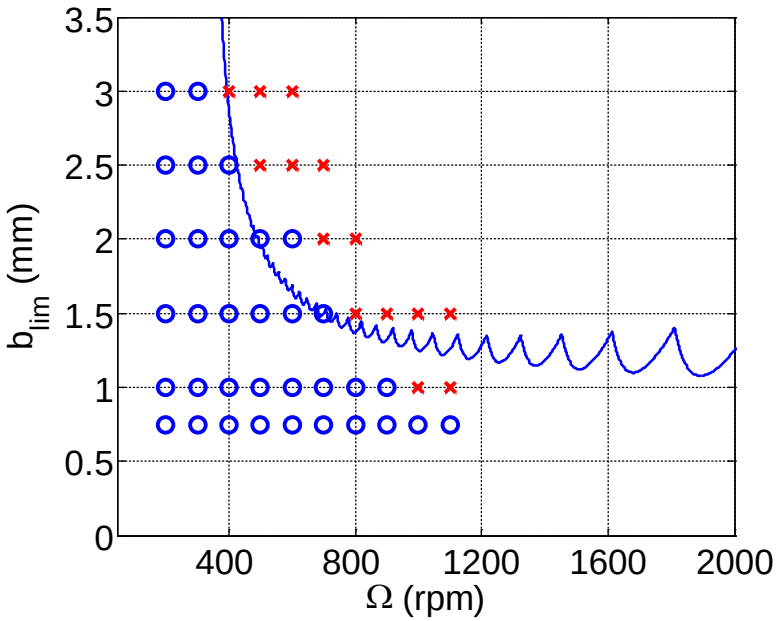

Figure 6.3: Up milling stability boundary for 50% radial immersion, 15° relief angle, low wear milling tests using the 228 Hz flexure setup ($C = 1.25\times10^5$ N/m).

Because flank wear can affect the process damping behavior due to changes in the tool/surface interference, the flank wear width (FWW) was limited to less than 100 µm for these stability tests; see Figure 6.4. The tool wear was monitored using the 60x digital microscope (Dino-Lite: model Pro-AM413T) described in Chapter 5.2.

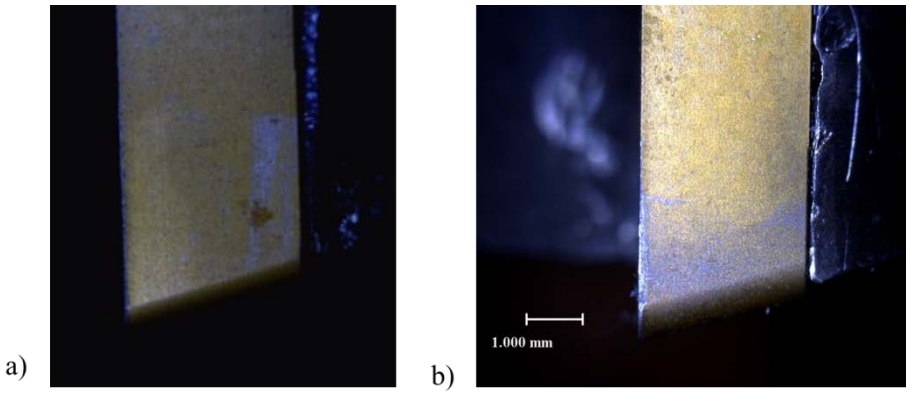

Figure 6.4: Tool wear measurement of: a) new 15° relief angle insert; and b) moderately worn 11° insert.

The procedure was repeated for the 156 Hz setup and a process damping coefficient of $C = 1.6 \times 10^5$ N/m was identified. These results are displayed in Figure 6.5. The lower natural frequency of the system causes a shift in the process damping regime to lower spindle speeds and limiting chip widths compared to the 228 Hz system. However, a comparison of the two process damping coefficients indicates less than a 4% difference. In this regard, it can be said that the process damping coefficient is insensitive to moderate changes in the system dynamics for single DOF systems.

Tests were then performed using the 19.05 mm diameter, 11° relief angle end mill. The same procedure was following and the FWW was again limited to be less than 100 μm for all cuts. The process damping coefficient for both the 228 Hz and 156 Hz setups was 1.65×10^5 N/m. See Figure 6.6 and Figure 6.7.

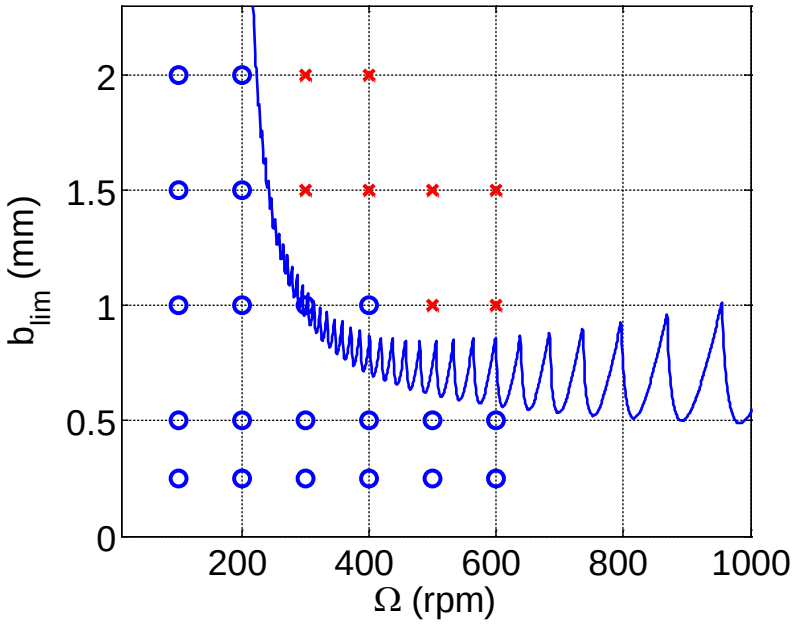

Figure 6.5: Up milling stability boundary for 50% radial immersion, 15° relief angle, low wear milling tests using the 156 Hz flexure setup (C = 1.30×10^5 N/m).

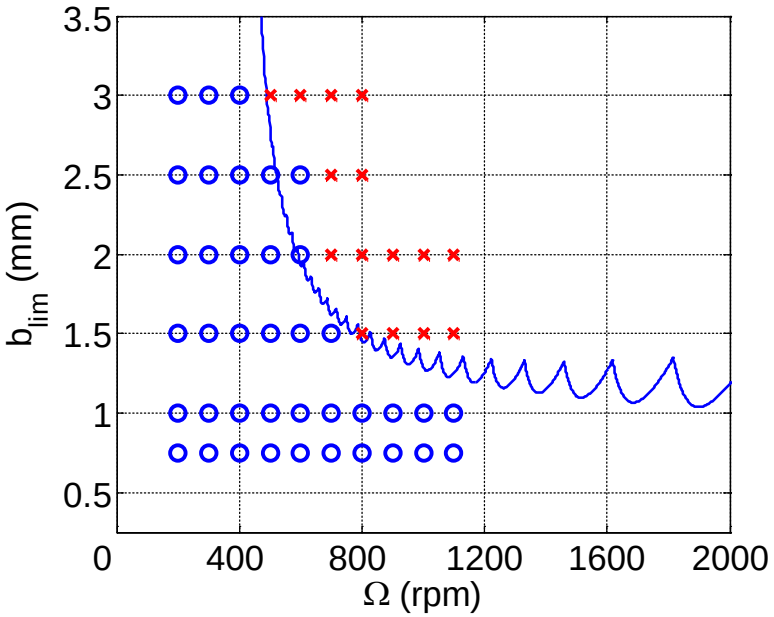

Figure 6.6: Up milling stability boundary for 50% radial immersion, 11° relief angle, low wear milling tests using the 228 Hz flexure setup (C = 1.65×10^5 N/m).

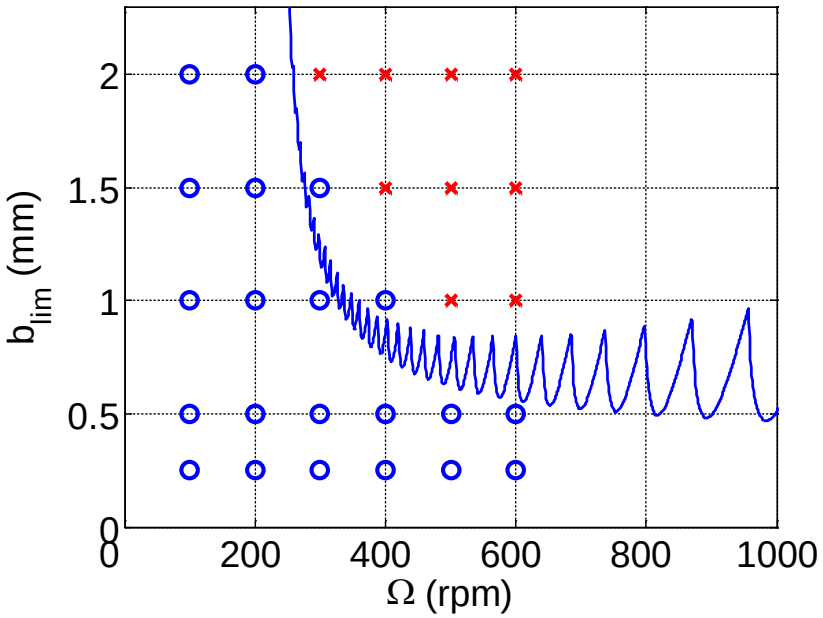

Figure 6.7: Up milling stability boundary for 50% radial immersion, 11° relief angle, low wear milling tests using the 156 Hz flexure setup (C = 1.65×10^5 N/m).

The low wear stability test results are summarized in Table 6.3. The process damping coefficient for the 228 Hz setup increased by 32% for the 11° relief angle tool relative to the 15° relief angle tool. A 27% increase was observed for the 156 Hz setup. These trends make sense given that additional interference would be encouraged by the smaller relief angle. Figure 6.8 illustrates the increase in the predicted stability boundary from a larger relief angle to smaller relief angle cutter.

Table 6.3: Comparison of process damping coefficients for low insert wear tests (FWW < 100 μm).

Relief angle (deg)	C (N/m) for the 228 Hz setup	C (N/m) for the 156 Hz setup
15	1.25×10^5	1.30×10^5
11	1.65×10^5	1.65×10^5

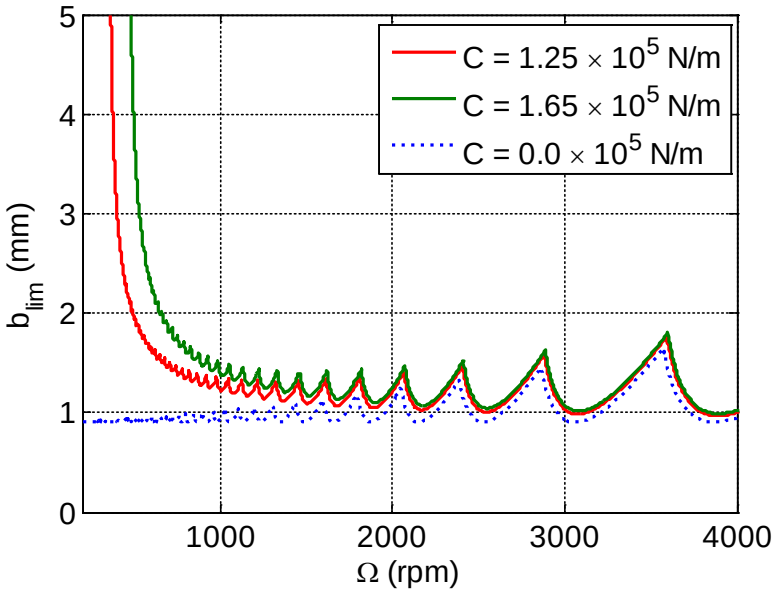

Figure 6.8: Comparison of analytical stability boundary for steel between the 15° relief angle process damping coefficient (C = 1.25×10^5 N/m - red) and the 11° relief angle process damping coefficient (C = 1.65×10^5 N/m - green). The blue stability boundary, C = 0.0×10^5 N/m, is used as a reference.

In order to explore the effect of tool wear on the process damping performance, tests were completed using worn tools where the FWW was maintained at a level of approximately 150 µm < FWW < 250 µm. For the 15° relief angle tool, the specific cutting force and cutting force direction were 2441.0 N/mm^2 and 63.5°, respectively; this represents a 3.5% increase in the specific cutting force relative to the unworn tool tests. However, the process damping coefficient was found to increase from the unworn tool tests by 20% for the 228 Hz setup and 31% for the 156 Hz setup. Similarly, for the 11° cutter, the cutting force parameters experienced only a slight change (K_s = 2550.2 N/mm^2 and β = 62.0°). However, the process damping coefficient increased by 15.2% for both flexure setups. See Table 6.4.

Table 6.4: Comparison of process damping coefficients for moderate wear tests (150 μm < FWW < 250 μm).

Relief angle (deg)	C (N/m) for the 228 Hz setup	C (N/m) for the 156 Hz setup
15	1.50×10^5	1.70×10^5
11	2.00×10^5	1.90×10^5

Repeat testing was performed using the 19.05 mm diameter, 11° relief angle cutting tool in order to observe the variability in the process damping coefficient identification process. A series of three additional cutting tests were performed on the 228 Hz system using an unworn insert. The three process damping coefficients were: 1.65×10^5 N/m, 1.65×10^5 N/m, and 1.45×10^5 N/m. Assuming a normal distribution, a two-sided 90% confidence level was computed for this small sample size. The confidence interval for the population mean was: $C = (1.60 \pm 0.15)\times10^5$ N/m. Figure 6.9 illustrates the corresponding confidence region.

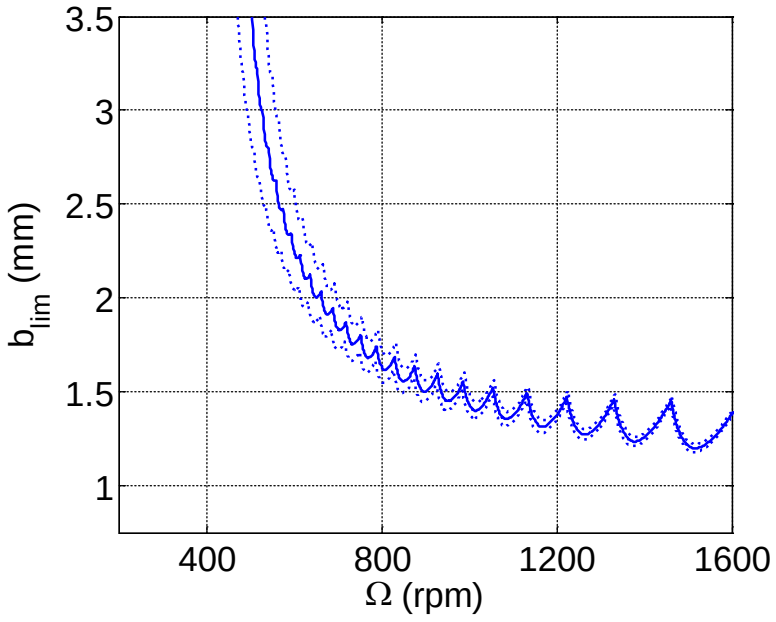

Figure 6.9: Up milling stability confidence region for 50% radial immersion, 11° relief angle milling tests using the 228 Hz flexure setup with an unworn cutting edge ($C = (1.60 \pm 0.15)\times10^5$ N/m).

6.1.2 Creating a Process Coefficient Database

With a technique in place to experimentally identify the process damping regime of the stability lobe diagram and the ability to portray the low-speed stability boundary using a single coefficient, a database of the process modeling coefficients was developed for several representative hard-to-machine materials. In addition to (mild) AISI 1018 steel, Ti 6Al-4V, AISI 304 stainless steel, and Inconel 718 were chosen to populate the database, based on their growing use in the medical, aerospace, and energy manufacturing sectors.

The database includes the process damping model coefficient, specific cutting force, and Taylor tool-life model. The coefficients are provided for two relief angles at both low and moderate wear states of the cutting edge. For the additional hard-to-machine metals in the database, the cutting conditions were changed from the 50% radial immersion up-milling in steel, to 25% radial depth of cut down-milling. This increased the allowable depths of cut for the harder materials and eliminated chip welding to the machined surface. The database of process modeling coefficients are presented in Table 6.5-6.9.

From Tables 6.5 and 6.6, it is observed that the process damping force coefficient, C, increases with progressive wear and decreases with a larger relief angle; a larger C value indicates more process damping. Both trends support the general description of process damping as interference between the relief face and machined surface. Increased flank wear reduces the apparent relief angle local to the cutting edge. A smaller relief angle, whether by design or via wear, encourages the interference phenomenon. Figure 6.10 illustrates the trend that a reduction in the insert relief angle leads to an increase in available stable cutting conditions.

Table 6.5: Process damping coefficients for the 11° relief angle tool geometry.

	Process damping coefficient, *C* (N/m)	
Material	Low insert wear (FWW < 0.100 µm)	Moderate insert wear (0.150 µm < FWW < 0.250 µm)
1018 Steel	1.65×10^5	2.00×10^5
Ti 6Al-4V	1.70×10^5	1.80×10^5
304 SS	5.20×10^5	5.80×10^5
Inconel 718	1.20×10^5	1.05×10^5

Table 6.6: Process damping coefficients for the 15° relief angle tool geometry.

	Process damping coefficient, *C* (N/m)	
Material	Low insert wear (FWW < 0.100 µm)	Moderate insert wear (0.150 µm < FWW < 0.250 µm)
1018 Steel	1.25×10^5	1.50×10^5
Ti 6Al-4V	1.20×10^5	1.40×10^5
304 SS	4.10×10^5	4.50×10^5
Inconel 718	1.00×10^5	1.30×10^5

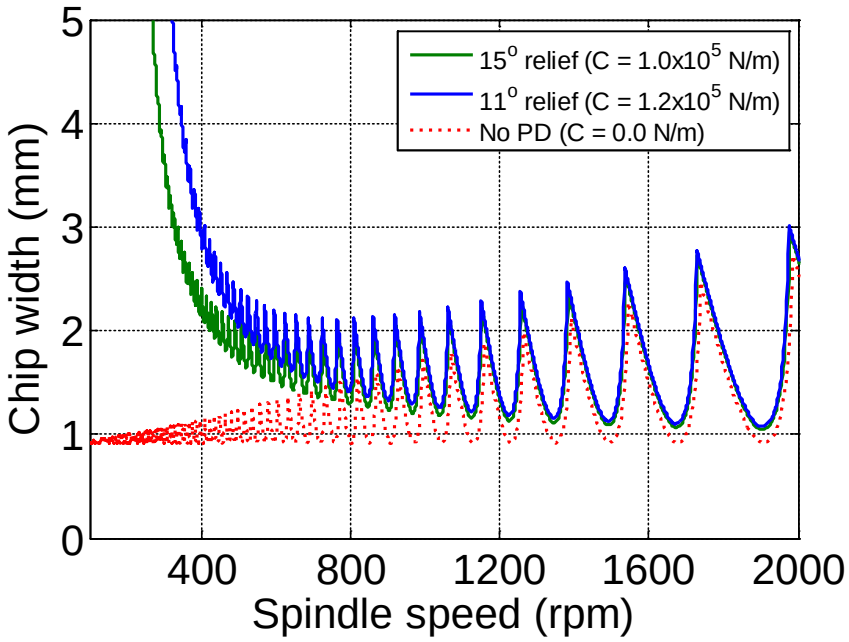

Figure 6.10: Stability boundary comparison for Inconel 718 for the low insert wear conditions.

For the specific cutting force coefficient, K_s, no clear trend is apparent for a change in the tool geometry. The largest difference for relief angle variation is 6.8% (1018 steel). The largest difference due to the wear level is -8.2% (15° relief angle tool, 6Al-4V titanium).

Table 6.7: Specific cutting force coefficients for the 11° relief angle tool geometry.

	Low insert wear (FWW < 0.100 µm)		Moderate insert wear (0.150 µm < FWW < 0.250 µm)	
Material	K_s (N/mm^2)	β (deg)	K_s (N/mm^2)	β (deg)
1018 Steel	2531.0	62.0	2550.2	62.0
Ti 6Al-4V	2107.0	66.0	2131.2	60.1
304 SS	3318.0	62.5	3517.0	61.0
Inconel 718	3515.0	61.1	3617.0	60.6

Table 6.8: Comparison of process coefficients for the 15° relief angle tool geometry.

	Low insert wear (FWW < 0.100 µm)		Moderate insert wear (0.150 µm < FWW < 0.250 µm)	
Material	K_s (N/mm^2)	β (deg)	K_s (N/mm^2)	β (deg)
1018 steel	2359.1	63.5	2441.0	63.5
Ti 6Al-4V	2076.3	66.7	2247.2	56.3
304 SS	3427.2	63.1	3503.2	61.5
Inconel 718	3582.0	62.0	3653.0	63.0

The Taylor tool life model parameters are presented in Table 6.9. It should be restated that the inserts used in gathering the tool life parameters were all PVD TiAlN coated. A water-based mist coolant with a flow rate of approximately 15-20 ml/min was used in each of the cutting experiments. Finally, the time to reach the limiting FWW of approximately 400 µm was the total cutting time for each selected cutting speed.

Table 6.9: Taylor tool-life model parameters.

Material	n_T	C_T	R^2
1018 steel*	0.34	649	0.95
Ti 6Al-4V	0.96	1804	0.97
304 SS	0.67	1484	0.98
Inconel 718	0.66	161	0.93

*Values were obtained from testing performed by Karandikar *et al*. [26] using the same tool geometry, but an uncoated insert and 50% radial immersion up milling.

6.2 Experimental Identification of Process Coefficients in MDOF Milling

An experimental process damping coefficient, C, was estimated from a residual sum of squares (RSS) minimization of points which best represent the stability boundary. A process damping coefficient value of $C = 1.80\times10^5$ N/m best represents the boundary. The stable (o) and unstable (x) test points and stability boundary are presented in Figure 6.11

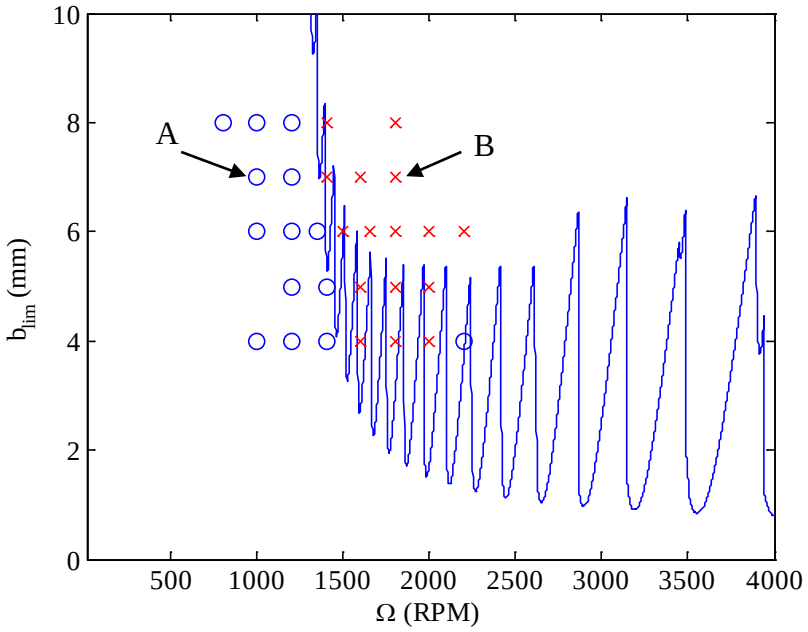

Figure 6.11: Stability boundary for the MDOF system. Stable (o) and unstable (x) experiments are identified.

Points A and B in Figure 6.11 were selected to illustrate stable and unstable cutting characteristics. Figure 6.12 illustrates the accelerometer signal at point A, a stable cut at 1000 rpm, b = 7.0 mm. The frequency content of the signal consists only of discrete peaks at integer multiples of the tooth passing frequency, in this case f_{tooth} = 16.66 Hz. Figure 6.13 illustrates measurement signals at point B, an unstable cut at 1800 rpm, b = 7.0 mm. This signal shows significant chatter frequency content near the second mode in addition to the discrete peaks at the tooth passing frequency; for this test, f_{tooth} = 30 Hz.

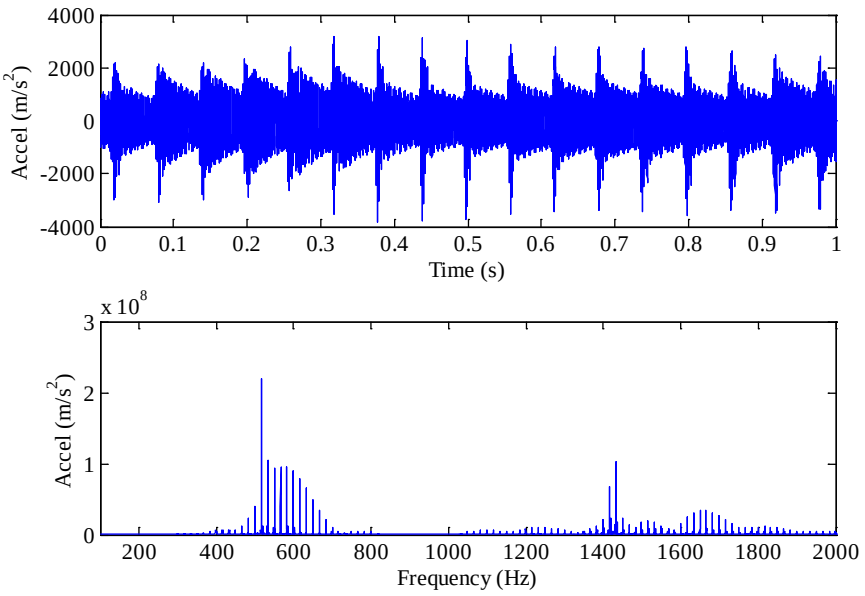

Figure 6.12: Accelerometer measurements of stable cut at 1000 rpm, b = 7.0 mm.

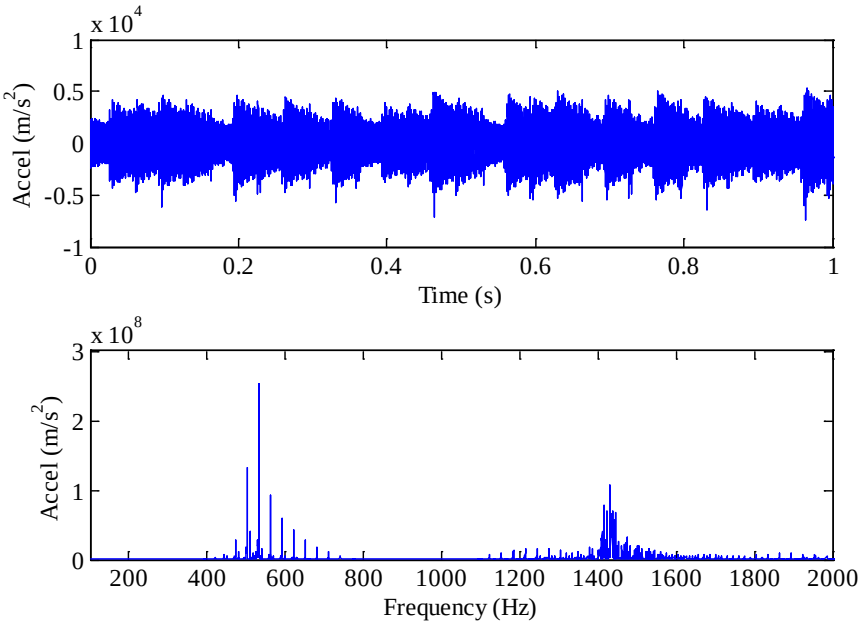

Figure 6.13: Accelerometer measurements of unstable cut at 1800 rpm, b = 7.0 mm.

6.3 Experimental Identification of Process Coefficients in MDOF Turning

The analytical model was validated using experimental testing. The average specific cutting force was calculated at both 500 and 1000 rpm for b = 1.0 mm and feed rate of 0.13 mm/rev to be approximately K_s = 1343±32 N/mm^2 and β = 55.0°. Orthogonal stability testing was completed using the custom parallelogram notch hinge flexible cutting tool to cut a tubular workpiece described in Chapter 5.3.1. Again, the cutting insert (Sandvik CCMW32.51H13A) was uncoated with a 7° relief angle, 0° rake angle, and no chip-breaker. Cutting vibration, cutting forces, and surface finish observation were used to distinguish stable and unstable cutting conditions for a defined grid of low spindle speed, chip width pairs. A process damping coefficient of $C = 2.60\times10^5$ N/m was calculated to best fit the grid of test points using a residual sum squared minimization for 6061-T6 aluminum. Figure 6.14 illustrates the actual stability boundary calculated for the MDOF

aluminum tests. The stability results for this test was described in detail in the experimental procedure in Chapter 5.3.2.

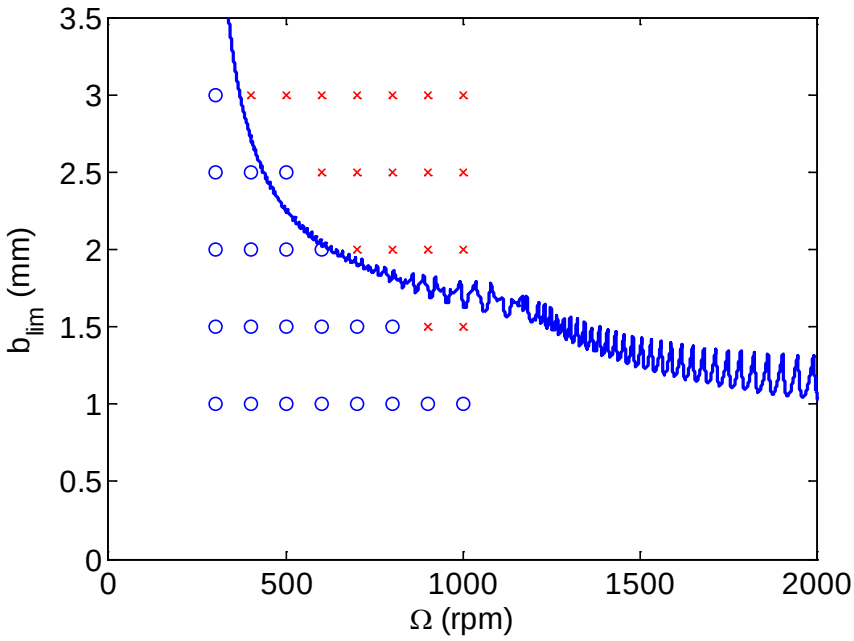

Figure 6.14: Stability boundary for the MDOF system with the grid of stable (o) and unstable (x) cutting tests identified (C = 2.6×10^5 N/m) for aluminum.

It is interesting to note the intersection of the stability boundary caused by the two vibratory modes that occurs at approximately 1200 rpm in the turning case. In fact, it is the higher stability boundary (corresponding to the stiffer vibration mode) that truncates the lower stability boundary (corresponding to less stiff mode of vibration) and determines the relatively large process damping coefficient value. If the lower stability boundary were not truncated, the process damping coefficient would be much lower and resemble the values obtained in single and multiple degree of freedom milling. The truncation that occurs could be an artifact of the stability algorithm; it is the dominant mode that needs to be considered when calculating the process damping value.

However, because the previous experiments revealed a sensitivity to tool geometry (i.e., relief angle and tool wear), it is uncertain if the large process damping coefficient value is a product of the algorithm or due to the discrepancy in the cutting insert geometry. To better understand this sensitivity, the MDOF milling stability tests were performed using the 11° relief angle coated insert, while the turning stability tests were performed with a 7° relief angle uncoated insert. The results of these tests are presented in the following section.

6.4 Process Damping Coefficient Versatility

A series of stability tests were conducted for single and multiple DOF milling and turning setups to examine the versatility of the experimental process damping coefficient. To avoid any effects from tool flank wear, the material chosen for each test was 6061-T6 aluminum. Additionally, the same coated milling insert (SPEB322 KC725M) was used in each of the cutting tests.

The test plan included the process damping coefficient identification for: first, the SDOF leaf-type flexure ($f_n \approx 250$ Hz), followed by a SDOF setup of much higher natural frequency. Previous experiments using steel workpieces showed that reducing the system's natural frequency had less than a 5% change in coefficient value. Increasing the system's natural frequency by greater than 200% would substantiate or refute the robustness of each identified process damping coefficient. Next, the same milling insert was seated in the MDOF turning flexure and the tubular orthogonal testing was repeated. The process damping value obtained was compared to the previous turning experiments using the 7° insert as well as the milling tests.

The stability testing procedure, which applied the least residual sum squared method to identify the process damping coefficient as described in Chapter 5, was used for the 11° relief insert geometry, 6061-T6 aluminum workpiece material, and parallelogram leaf-type flexure. The setup for this experiment is presented in Figure 6.15. Similar to the MDOF milling tests, the aluminum workpieces were pre-machined to have a fin geometry, to eliminate any nose radius effects.

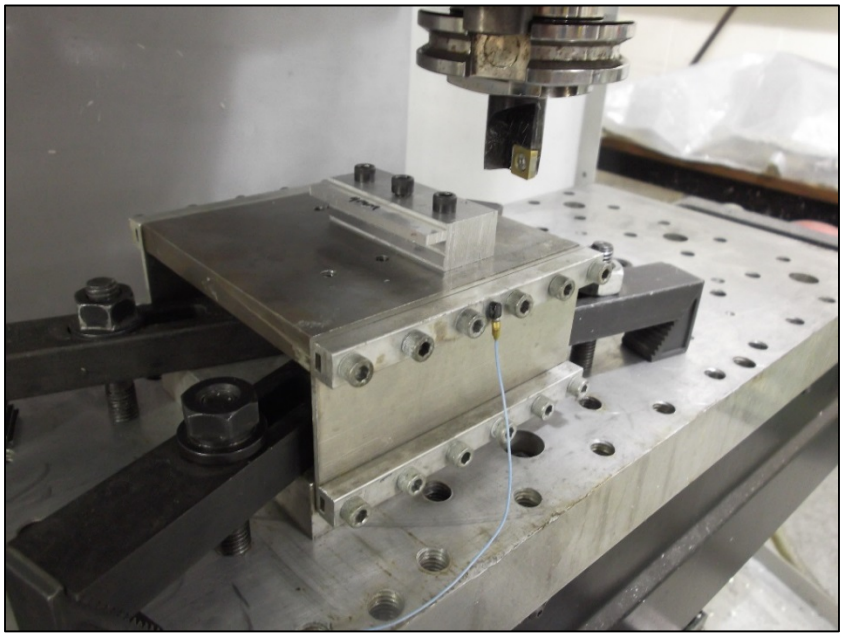

Figure 6.15: SDOF parallelogram leaf-type flexure for orthogonal stability testing with 6061-T6 aluminum finned workpieces.

An accelerometer was adhered to the flexure to gain insight into the stability of the cutting operation. The time and frequency domain signals of a stable and unstable test cut are illustrated in Figure 6.16. After performing test cuts over a specified grid of chip width - spindle speed combinations, a process damping coefficient of $C = 1.80\times10^5$ N/m was identified, see Figure 6.17. This C value corresponds closely to value of $C = 1.60\times10^5$ N/m for the MDOF aluminum tests with the same insert.

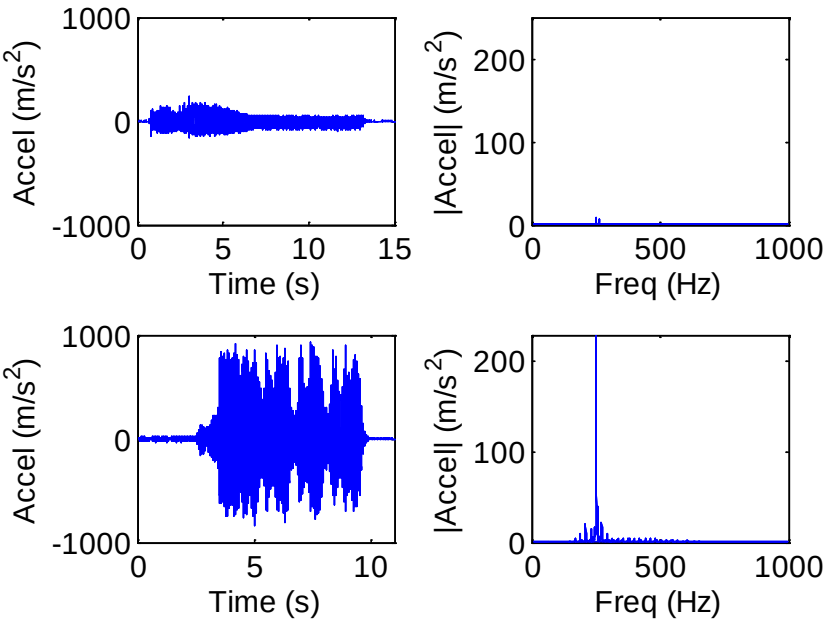

Figure 6.16: Accelerometer time domain signals of stable (top-left) and unstable (bottom-left) cutting parameters and the accompanied frequency domain stable (top-right) and unstable (bottom-right) signals.

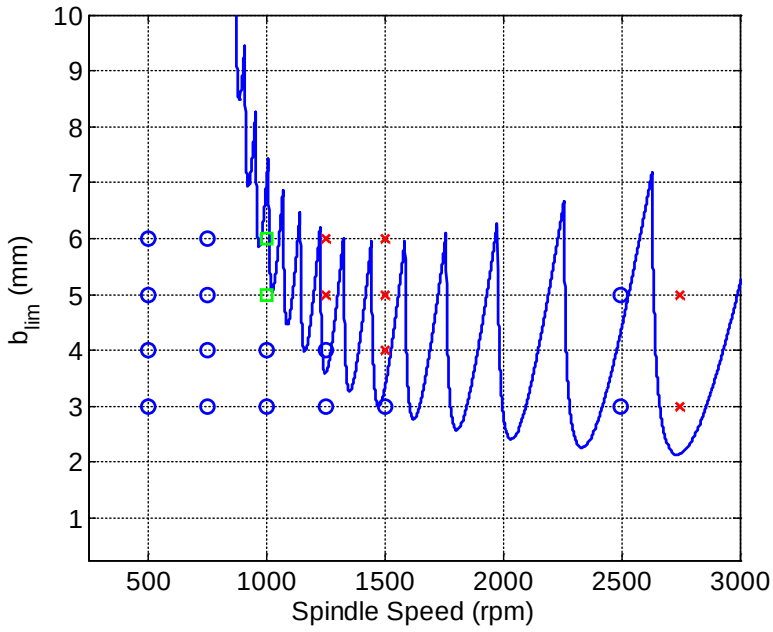

Figure 6.17: Grid of stable ('o'), unstable ('x'), and marginally stable ('square') test points with the final stability boundary corresponding to $C = 1.80\times10^5$ N/m.

To further reinforce the idea that the same process damping coefficient can be used for a wide range flexible cutting systems, an additional SDOF notch-type flexure was constructed and the same testing procedure was used to find the process damping coefficient. The setup for the SDOF system is depicted in Figure 6.18, with a schematic of the flexure in top-right of the image. The modal parameters of the higher natural frequency system are: f_n = 815 Hz, k = 8.90×10^6 N/m, and ζ = 0.47%. For reference, the lower natural frequency system's modal parameters for the aluminum tests were: f_n = 257 Hz, k = 5.58×10^6 N/m, and ζ = 1.6%.

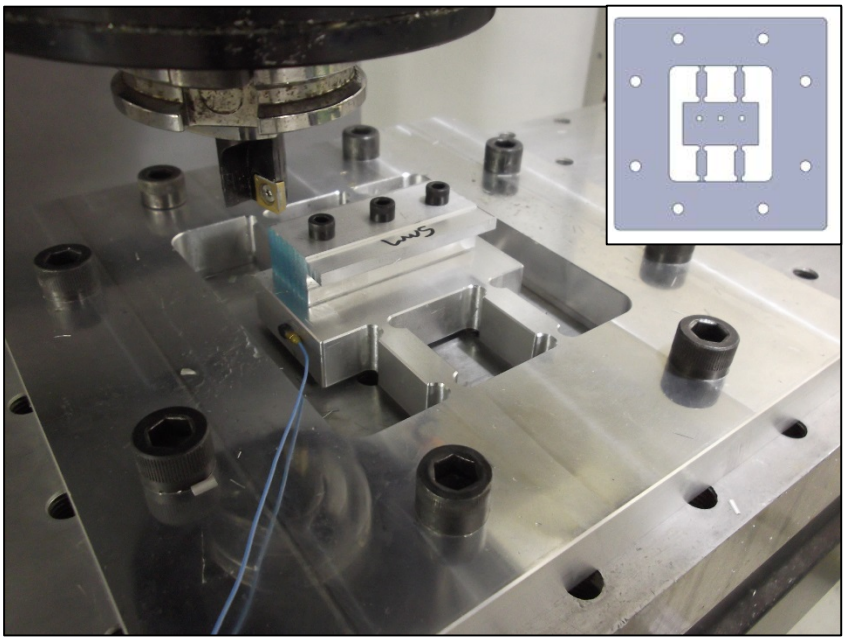

Figure 6.18: SDOF milling setup with system's natural frequency approximately f_n = 815 Hz. A schematic of the flexure is shown in the top right corner of the image.

Similar to the previous SDOF freedom stability tests, an accelerometer was attached during the orthogonal machining of finned-aluminum workpieces. The dynamic signals in the time and frequency domains are illustrated in Figure 6.19. A best-fit stability corresponded to a process damping coefficient value of C = 1.70×10^5 N/m, see Figure 6.20.

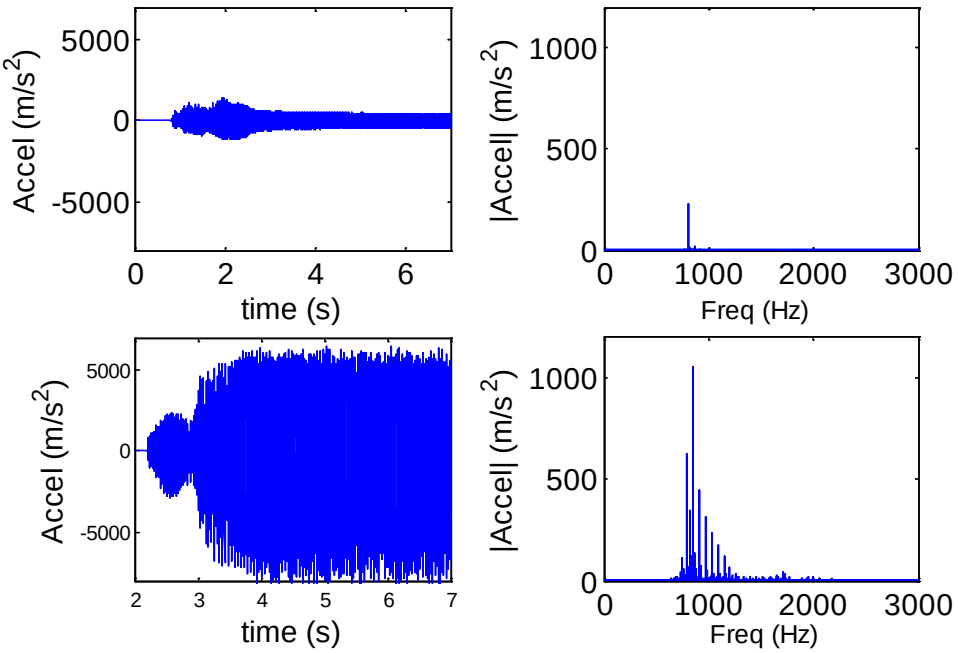

Figure 6.19: Accelerometer time domain signals of stable (top-left) and unstable (bottom-left) cutting parameters and the accompanied frequency domain stable (top-right) and unstable (bottom-right) signals for the f_n = 815 Hz system.

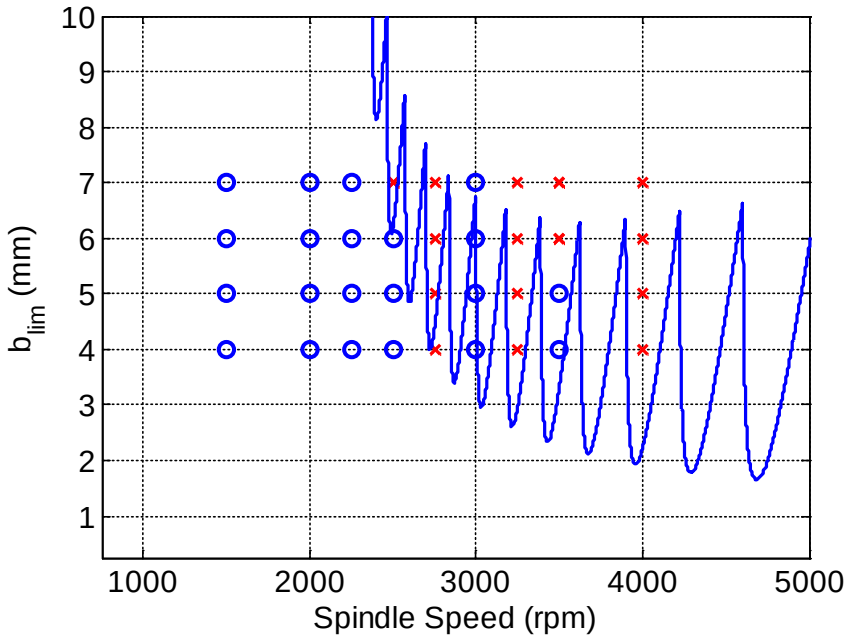

Figure 6.20: Grid of stable ('o') and unstable ('x') test points with the final stability boundary corresponding to $C = 1.70\times10^5$ N/m.

Examining the tests performed thus far, it is observed that there is relatively low variability between systems of low and high natural frequency as well as between single and multiple degrees of freedom systems. To address the large discrepancy of the process damping coefficient between milling and turning operations, the same insert geometry used in the milling tests was mounted in the MDOF flexure used in the turning stability tests, see Figure 6.21.

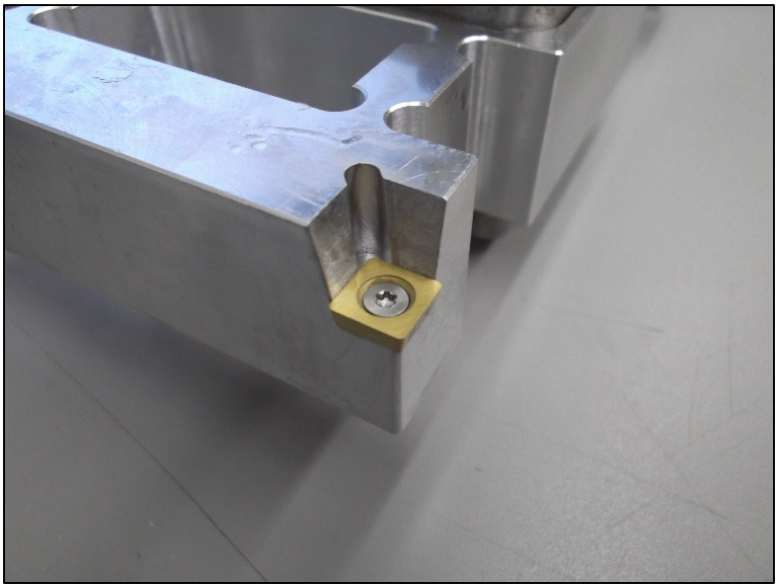

Figure 6.21: 11 degree milling insert mounted to MDOF flexible turning tool for orthogonal stability tests.

Upon remounting the flexure as described in Chapter 5, there were noted changes in the system's dynamics, see Table 6.10. Particularly, the damping ratios in the feed direction increased when remounting the flexure for the 11° relief angle tests.

Table 6.10: Feed direction modal parameters for 7° and 11° relief angle setups.

	Viscous damping ratio (%)	Modal stiffness ($\times 10^7$ N/m)	Natural frequency (Hz)
	7° relief angle setup		
Mode 1	3.56	0.85	304
Mode 2	5.46	1.17	394
Mode 3	0.99	2.69	1410
	11° relief angle setup		
Mode 1	6.23	0.80	303
Mode 2	9.01	0.96	405
Mode 3	1.68	1.88	1433

A similar grid of chip width-spindle speed combinations were tested as the original turning experiments and the stability was analyzed. A process damping coefficient of $C = 1.70 \times 10^5$ N/m was calculated to best fit the grid of test points. However, it was observed that the grid of stable and unstable points changed relatively little between the two tests, see Figure 6.22. Due to the slight changes in dynamics between the sensitive modes of vibration, the intersection of the stability boundaries also changes. The intersection of the two lower stability boundaries, which occurred at approximately 1200 rpm and 1.5 mm previously, now occurs near 500 rpm and 2.5 mm. The stability boundary is truncated in such a way that it is now the lower boundary (corresponding to the more flexible mode of vibration) which determines the ‘best fit’ process damping coefficient.

It is concluded that there is a decision to make when analyzing MDOF systems. Either the user can fit the stability boundary while taking into consideration all modes of vibration, or the user can consider only the most flexible mode of vibration when calculating the

process damping coefficient. The former method may lead to higher, perhaps artificial, process damping coefficient values. The latter method of taking into consideration the most flexible mode of vibration has been shown to lead to process damping values which agree for single and multiple DOF systems in milling and turning.

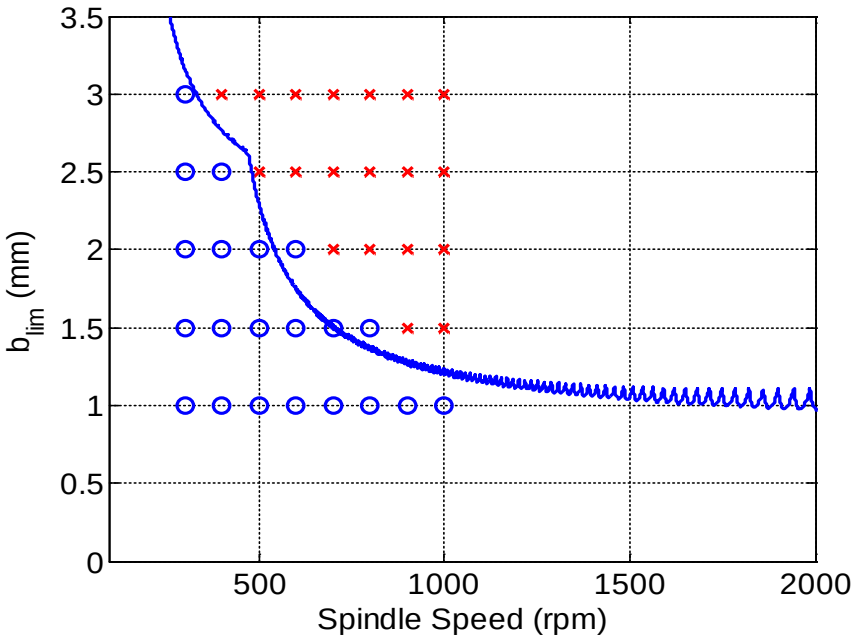

Figure 6.22:Grid of stable ('o') and unstable ('x') test points with the final stability boundary corresponding to $C = 1.70\times10^5$ N/m for turning tests with 11° relief angle insert.

CHAPTER 7: CONCLUSIONS AND FUTURE WORK

7.1 Conclusions

In this research, an analytical stability solution was developed that considers process damping in milling and turning applications. Derivation of the model, which includes a single process damping coefficient, *C*, was presented for single and multi-degree of freedom systems and verification was completed using experiments.

Accurate stability prediction at low machining speeds is sensitive to the workpiece material, tool geometry, and frequency of surface vibrations during cutting. Process damping due to flank-workpiece interference serves to increase the stability at these low cutting speeds. The approach used to model the process damping effect included an equivalent viscous damping force. This process damping force depended proportionally on the chip width and cutter velocity and inversely proportionally on the cutting speed. In addition, the damping force was proportional to a process damping coefficient, which is analogous to the specific cutting force, K_s, approach used to model cutting force. Due to the chip width and cutting speed dependence of the process damping force, the new stability analysis followed an iterative, converging approach to produce the stability boundary. The limiting chip width values were observed to increase for individual stability lobes as spindle speeds decreased in the process damping regime.

For initial experiments, a single tooth indexable end mill was used to mill AISI 1018 steel workpieces secured to a single DOF parallelogram flexure. The stability limit was identified over a grid of stable/unstable axial depths of cut and spindle speeds. Cutting stability was identified in two ways: 1) the frequency content of an accelerometer secured to the flexure; and 2) qualitative analysis of the machined surface using a digital microscope. Using the experimental stability boundary, the process damping coefficient was determined in a best-fit manner. The effects of the cutting insert relief angle and tool wear were examined. The flexure dynamics were also adjusted to determine the sensitivity of the process damping coefficient to changes in the system dynamics.

For a 50% radial immersion up milling cut, the stability boundary was discovered to increase as the spindle speed decreased and a value for the process damping coefficient was obtained. Substituting the original 15° relief angle insert for an 11° relief angle insert and repeating the cutting tests revealed that the process damping coefficient increased by approximately 30%. This indicated that the decreased relief face angle increases process damping, as expected. Tests were also completed using both new and worn inserts. Under worn conditions, the process damping coefficient increased by approximately 15% compared to new conditions. Finally, the dynamic properties of the system were adjusted by increasing the mass fixed to the flexure. No appreciable change in the process damping coefficient was observed.

Repeat testing was performed in order to observe the variability in the process damping coefficient. A total of four stability grids were evaluated using the same experimental conditions and a confidence interval for the stability boundary was established. Results

indicated acceptable repeatability in the process damping coefficient identified using the experimental approach.

Process damping is particularly important for exotic metals, such as titanium, nickel super alloys, and hardened steels. With an established method to identify the process damping regime using a single coefficient, a database of process modeling coefficients was produced for selected hard-to-machine materials: AISI 1018 steel, 6Al-4V titanium, AISI 304 stainless steel, and Inconel 718. The reference tables were established to tabulate not only the process damping coefficient, but also the cutting force model coefficients, and Taylor tool-life model parameters. Process damping and cutting force parameters were reported for both low and moderate wear levels.

Stability testing was completed using the single DOF parallelogram flexure to identify the process damping behavior for low-speed milling. Two inserted cutting tools were used with relief angles of 11° and 15°; the rake and helix angles were zero for both single-insert cutters. It was demonstrated that a reduction in the relief angle and an increase in flank wear on the cutting edge resulted in an increased process damping effect for each of the materials tested.

The analytical MDOF turning model was validated as well using experimental testing. Orthogonal stability testing was completed using a custom parallelogram notch hinge flexible tool to cut a tubular workpiece. The cutting tool was designed to have two primary vibratory modes in the feed direction of the cutting process. Cutting vibration, cutting forces, and surface finish observation were used to distinguish stable and unstable cutting conditions for a defined grid of low spindle speed, chip width pairs. A process damping coefficient of $C = 2.6 \times 10^5$ N/m was calculated to best fit the grid of test points using a

residual sum squared minimization for 6061-T6 aluminum. The average specific cutting force was calculated at both 500 and 1000 rpm for b = 1 mm and feed rate of 0.13 mm/rev to be approximately K_s = 1343±32 N/mm^2 and β = 55.0°. The turning experiments described were performed using inserts with a 7° relief angle.

The MDOF milling model was evaluated using similar experimental testing. Stability experiments were performed using a custom double-parallelogram notch hinge flexure, upon which a finned 6061-T6 aluminum workpiece was mounted. The flexure was designed to have two primary vibratory modes along the feed direction of the cutting process. Vibration of the flexure/workpiece system was used to determine the stability of the cutting process at selected spindle speed and axial depth of cut combinations. A process damping coefficient of $C = 1.8\times10^5$ N/m was calculated using RSS minimization to best fit the stability boundary. At 1000 rpm and feedrates from 0.010 to 0.076 mm/tooth, the specific cutting force was identified as K_s = 1368 N/mm^2 with β = 50.7°. The MDOF milling experiments were performed with the 11° relief angle cutter described in the single DOF experiments. The decrease in process damping coefficient between milling and turning experiments could be explained as an artifact of the stability algorithm, whereby a truncation of the stability boundary occurs at low speeds.

7.2 Future Work

This work describes an analytical stability model that includes process damping for single and multiple DOF vibrating systems in turning and milling operations. This model includes contributions from the frequency response function of the vibratory system, as well as a process damping force, which is a function of the depth of cut, cutting surface speed, and an empirically-determined process damping coefficient, C. It was demonstrated

that the process damping coefficient and related process modeling coefficients can be readily and repeatedly identified using the detailed procedure. Next steps will include continuing the procedure for relating the C values identified here to a single-parameter exponential function that describes the low spindle speed stability boundary due to process damping (see Appendix B).

REFERENCES

[1] Tobias, S., and Fishwick, W. *Theory of regenerative machine tool chatter*. The Engineer 205 (1958).

[2] Tlusty, J. *Manufacturing Processes and Equipment*. Prentice Hall, Upper Saddle River, NJ, 2000.

[3] Merritt, H. Theory of self-excited machine tool chatter. *Journal of Engineering for Industry* 87 (1965), 447.

[4] Ezugwu, E.O., Z.M. Wang, and A.R. Machado. "The machinability of nickel-based alloys: a review." Journal of Materials Processing Technology 86.1 (1998): 1-16.

[5] Richards, N., and D. Aspinwall. "Use of ceramic tools for machining nickel based alloys." International Journal of Machine Tools and Manufacture 29.4 (1989): 575-588.

[6] Ezugwu, E. O., Z. M. Wang, and C. I. Okeke. "Tool life and surface integrity when machining Inconel 718 with PVD-and CVD-coated tools." Tribology transactions 42.2 (1999): 353-360.

[7] Khidhir, B.A., and B. Mohamed. "Study of cutting speed on surface roughness and chip formation when machining nickel-based alloy." Journal of mechanical science and technology 24.5 (2010): 1053-1059.

[8] Kadirgama, K., et al. "Tool life and wear mechanism when machining Hastelloy C-22HS." Wear 270.3 (2011): 258-268.

[9] T.R. Sisson, R.L. Kegg, An explanation of low-speed chatter effects, Journal of Engineering for Industry, 91 (1969) 951-958.

[10] P.W. Wallace, C. Andrew, Machining forces: Some effects of tool vibration, Journal of Mechanical Engineering Science, 7 (1965) 152-162.

[11] Tlusty, J., Ismail, F., Special Aspects of Chatter in Milling, ASME Trans., Journal of Vibration, Acoustics, Stress and Reliability in Design, Vol. 105 (1983) pp. 24 -32

[12] J. Tlusty, W. Zaton, F. Ismail, Stability lobes in milling, Annals of the CIRP, 32/1 (1983) 309-313.

[13] D.W. Wu, A new approach of formulating the transfer function for dynamic cutting processes, Journal of Engineering for Industry, 111 (1989) 37-47.

[14] B.Y. Lee, Y.S. Trang, S.C. Ma, Modeling of the process damping force in chatter vibration, International Journal of Machine Tools and Manufacture, 35 (1995) 951-962.

[15] M.A. Elbestawi, F. Ismail, R. Du, B.C. Ullagaddi, Modelling machining dynamics damping in the tool-workpiece interface, Journal of Engineering for Industry, 116 (1994) 435-439.

[16] Y.S. Chiou, E.S. Chung, S.Y. Liang, Analysis of tool wear effect on chatter stability in turning, International Journal of Mechanical Sciences, 37 (1995) 391-404.

[17] R.Y. Chiou, S.Y. Liang, Chatter stability of a slender cutting tool in turning with tool wear effect, International Journal of Machine Tools and Manufacture, 38 (1998) 315-327.

[18] Y. Altintas, M. Eynian, H. Onozuka, Identification of dynamic cutting force coefficients and chatter stability with process damping, Annals of the CIRP, 57/1 (2008) 371-374.

[19] Eynian, M., Altintas, Y., Analytical chatter stability of milling with rotating cutter dynamics at process damping speeds", ASME Journal of Manufacturing Science and Technology, 132 (2009) 354-361.

[20] C.Y. Huang, J.J. Wang, Mechanistic modeling of process damping in peripheral milling, Journal of Manufacturing Science and Engineering, 129 (2007) 12-20.

[21] E. Budak, L.T. Tunc, A new method for identification and modeling of process damping in machining, Journal of Manufacturing Science and Engineering, 131 (2009) 051019/1-10.

[22] L.T. Tunc, E. Budak, Effectof cutting conditions and tool geometry on process damping in machinng, Journal of Machine Tools and Manufacture, 57 (2012) 10-19.

[23] N.D. Sims, M.S. Turner, The influence of feed rate on process damping in milling modeling and experiments, Proceedings of the Institution of Mechanical Engineers, Part B: Journal of Engineering Manufacture, 225 (2011) 799-810.

[24] A.R. Yusoff, S. Turner, The role of tool geometry in process damped milling, International Journal of Advanced Manufacturing Technology, 50 (2010) 883

[25] T. Schmitz, S. Smith, Machining Dynamics: Frequency Response to Improved Productivity, Springer, New York, NY, 2009.

[26] J. Karandikar, A. Abbas, T. Schmitz, Tool life prediction using random walk Bayesian updating, Machining Science and Technology, 17/3 (2013) 410-442.

APPENDIX A: ANALYTICAL SOLUTION FOR RADIAL IMMERSION PROCESS DAMPING

This appendix describes a method to produce analytical radial depth of cut stability lobe diagrams that include process damping. The stability limit was defined using the radial, rather than axial, depth due to the path planning approach for many computer-aided manufacturing (CAM) programs, which remove material layer-by-layer with a varying radial immersion. Experimental validation of the predicted stability limits was performed and the results are presented for both the process damping (low cutting speed) range and higher cutting speeds.

A.1: Radial Depth Analytical Solution.

The analytical solution for developing constant radial depth of cut stability lobe boundaries for milling is described in Chapter 4. The spindle speed versus radial depth of cut stability lobe diagram is produced using the following sequence of steps.

1. Specify the system dynamics, tool geometry, and force model, including both the cutting force and process damping coefficients.

2. Select the desired spindle speed range and axial depth of cut.

3. Generate the spindle speed versus axial depth stability lobe diagram for the selected dynamic system using the smallest desired radial depth of cut.

4. Use the collection of stability lobes from step 3 to identify the limiting axial depth of cut as a function of spindle speed.

5. Determine the spindle speeds at which the limiting axial depth is equal to the desired axial depth from step 2. Store these {spindle speed, radial depth} pairs.

6. Increment the radial depth of cut to a larger value and repeat steps 3-5. Continue until the radial depth is increased to the tool diameter.

7. Collect all {spindle speed, radial depth} pairs from steps 3-6. The result is the limiting radial depth of cut as a function of spindle speed. Because the axial depth of cut stability analysis includes process damping, the final radial depth stability limit also incorporates process damping effects.

The procedure steps are demonstrated through an example and the corresponding figures. For the example, the selected spindle speed range is zero to 10000 rpm and the desired axial depth of cut is 3 mm. The spindle speed versus axial depth of cut stability lobe diagram for an up (conventional) milling radial depth of cut equal to 25% of the tool diameter (i.e., a 25% radial immersion) is displayed in Figure A.1. This represents the result from step 3. Figure A.2 shows the axial depth stability limit after step 4. The spindle speeds where the limiting axial depth is equal to the desired axial depth (b = 3 mm) for the final radial depth stability lobe diagram are identified in Figure A.3 (step 5). For comparison purposes, the step 5 result for a 50% radial immersion is shown in Figure A.4. It is observed that number of speeds is reduced with the increased radial depth because the axial depth stability limit is lowered. The final radial depth of cut stability lobe diagram (step 7) is displayed in Figure A.5. The corresponding diagram for a desired axial depth of 5 mm is provided in Figure A.6. As expected, the radial depth stability limit is lowered with the increased axial depth.

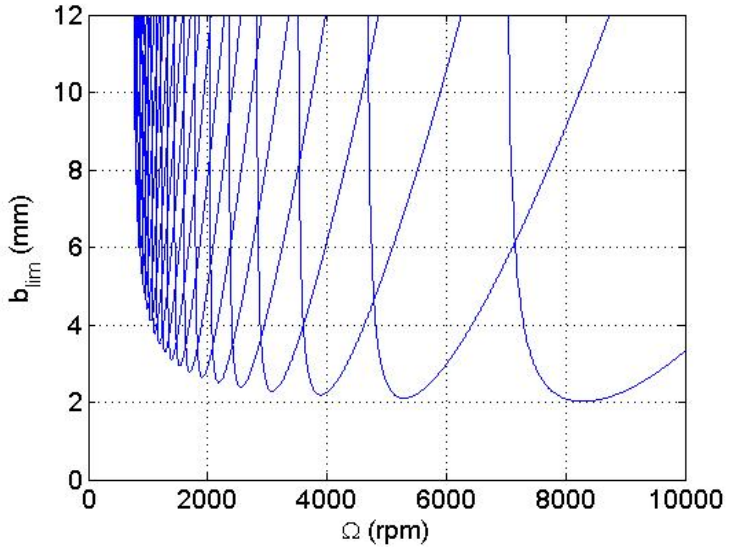

Figure A.1: Limiting axial depth of cut versus spindle speed for a 25% radial immersion.

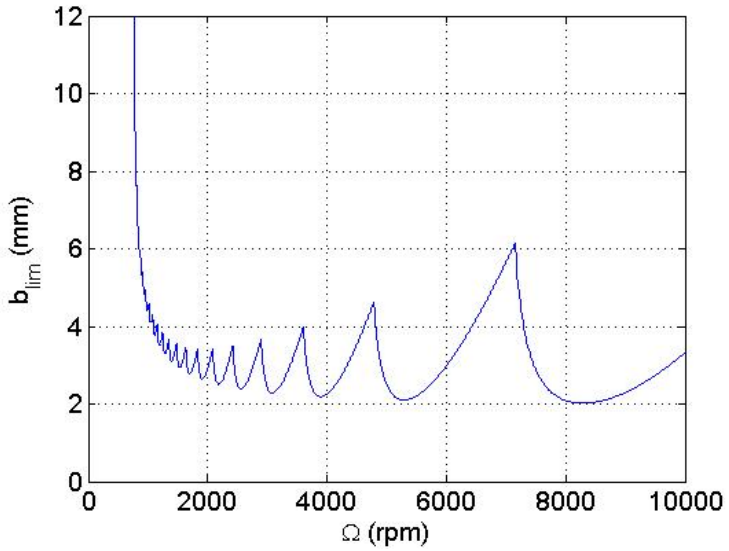

Figure A.2: Axial depth stability limit for a 25% radial immersion.

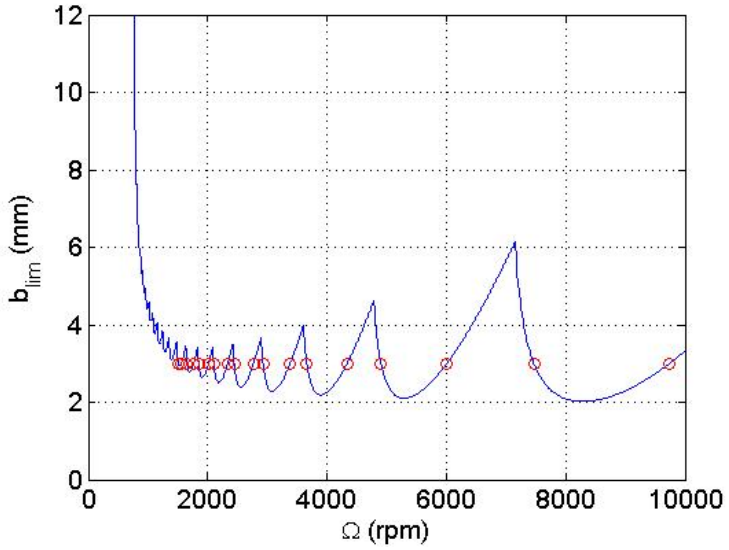

Figure A.3: Axial depth stability limit for a 25% radial immersion with the b = 3 mm spindle speeds identified (circles).

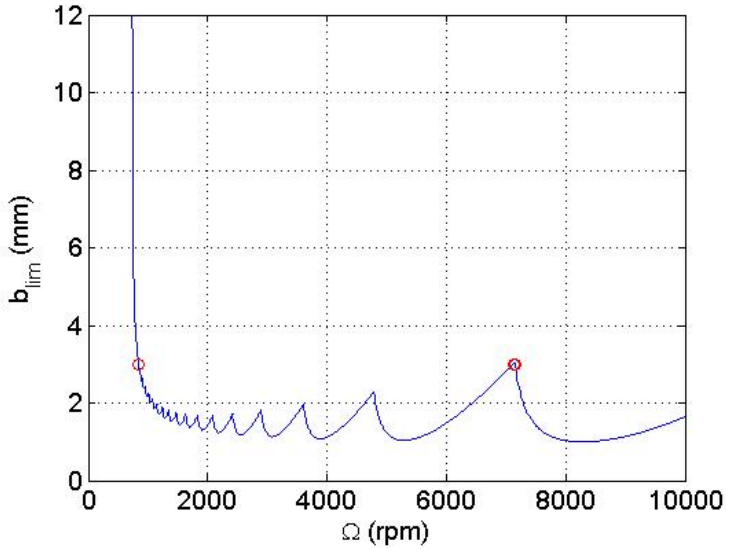

Figure A.4: Axial depth stability limit for a 50% radial immersion with the b = 3 mm spindle speeds identified (circles).

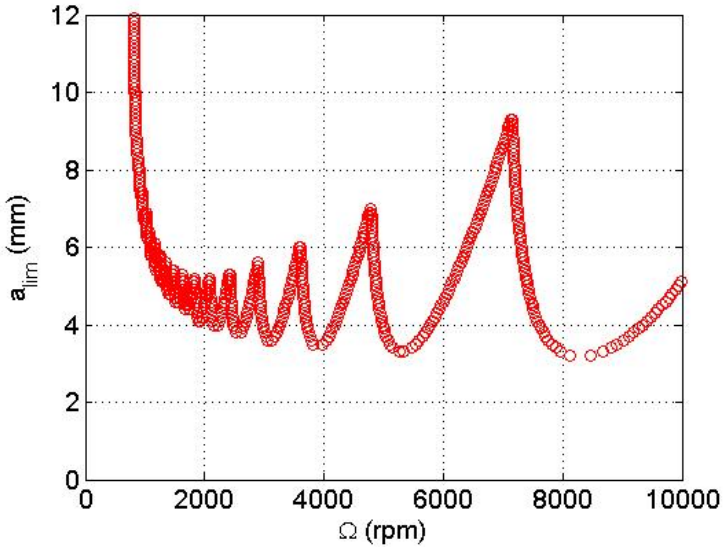

Figure A.5: Limiting radial depth of cut, a_{lim}, versus spindle speed for an axial depth of 3 mm.

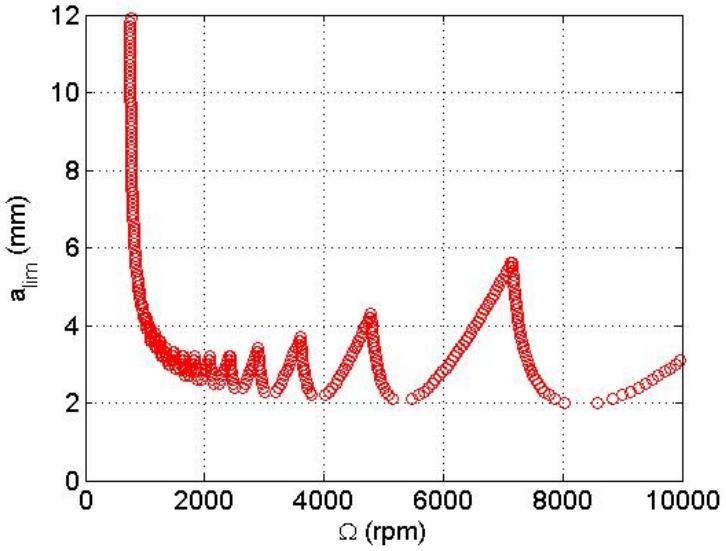

Figure A.6: Limiting radial depth of cut versus spindle speed for an axial depth of 5 mm.

A.2: Experimental Results for Radial Immersion Testing

Milling experiments were performed to observe the effects of varying the radial depth of cut while maintaining a constant axial depth. A single tooth, 19.05 mm diameter,

indexable end mill was used to machine AISI 1018 steel test coupons. The cutting inserts had a 0° rake angle and an 11° relief angle. The specific cutting force, K_s, and cutting force angle, β, were measured to be 2531.0 N/mm^2 and 62.0°, respectively, using a cutting force dynamometer (Kistler 9257B). A linear regression to the mean cutting force over a range of feed per tooth values was used to identify the force model values. A process damping coefficient of C = 1.65 x 10^5 N/m was determined using the procedure described in.

A parallelogram, leaf-type flexure was constructed to provide a flexible base for the test coupons; see Figure A.7. The compliance of the platform in its flexible direction was approximately 10 times greater than that of the most flexible mode for the cutting tool-holder-spindle-machine assembly. The modal parameters for the flexure are provided in Table A.1.

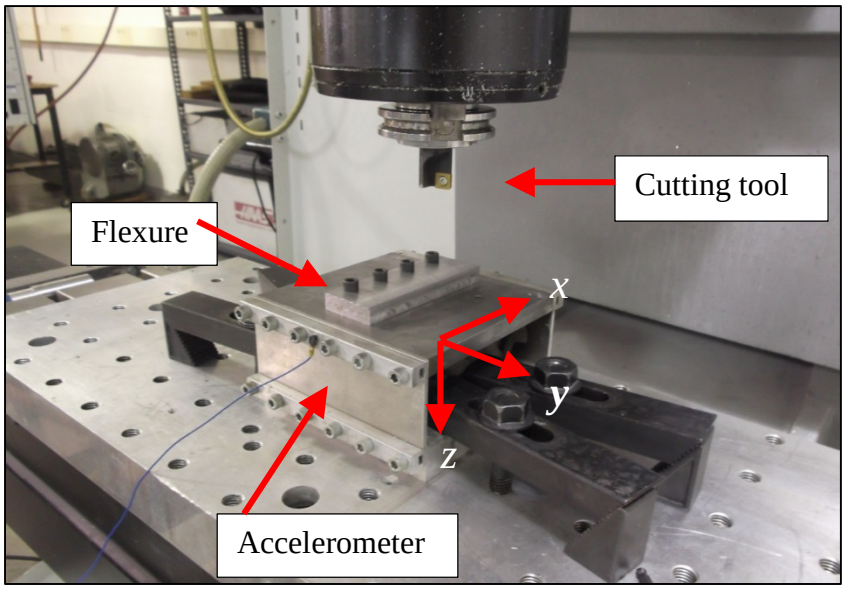

Figure A.7: Photograph of milling setup. The test coupon was bolted to the flexure. An accelerometer was used to measure the vibration during *x*-direction cutting and identify stable and unstable conditions.

Table A.1: Modal parameters for the SDOF flexure setup.

Direction	Modal stiffness (N/m)	Viscous damping ratio	Natural frequency (Hz)
x	6.60×10^6	2.1	247.2
y	338.0×10^6	1.5	1214

The flexure's modal parameters, the tool geometry, and the cutting force model were used to generate radial depth of cut stability lobe diagrams for selected axial depths as described previously. To verify the stability predictions, cuts were completed at multiple {spindle speed, radial depth} pairs. A piezoelectric accelerometer (PCB Piezotronics model 352B10) was used to measure the flexure vibration during cutting. The frequency content of the accelerometer signal and the machined surface finish were used to characterize the stability. Cuts that exhibited significant frequency content near to the flexure's natural frequency, rather than at the tooth passing frequency and its harmonics were considered unstable. A comparison of surfaces from unstable and stable cuts is provided in Figure A.8; the images were obtained using a portable digital microscope.

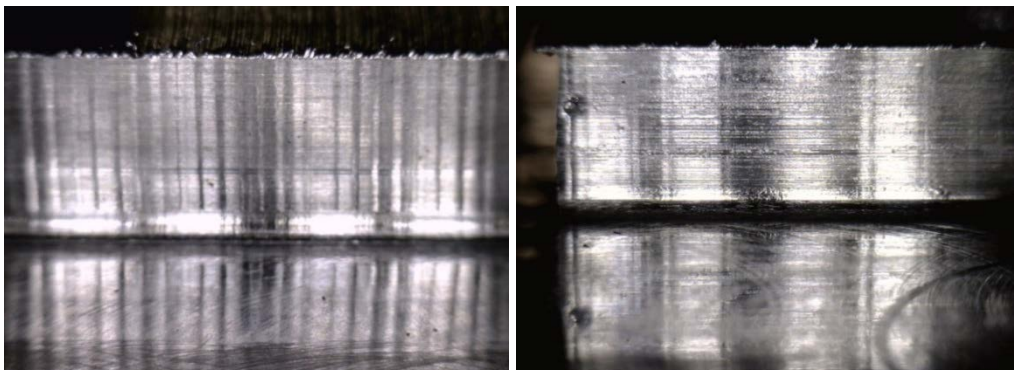

Figure A.8: Images of surfaces for unstable (left) and stable (right) cutting conditions.

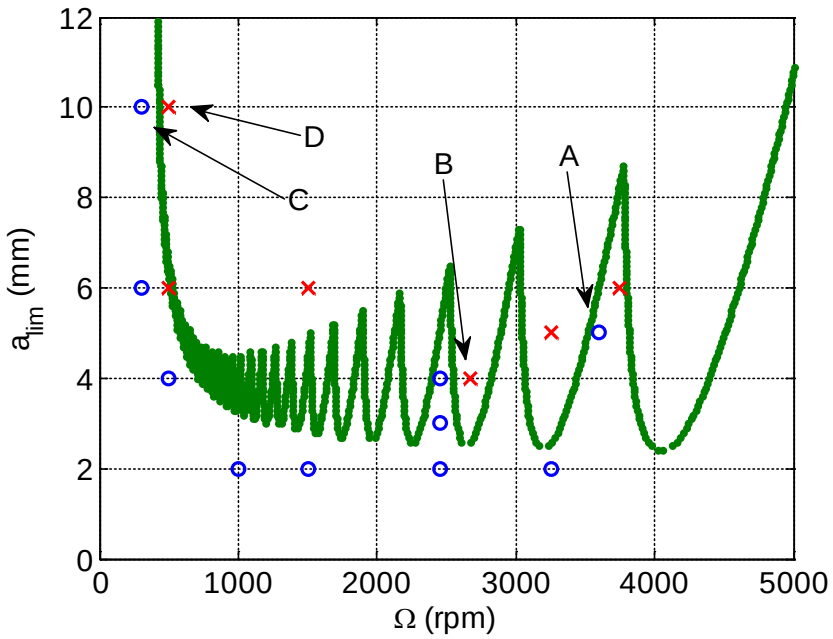

Figure A.9: Limiting radial depth of cut versus spindle speed for the flexure setup with a 3 mm axial depth.

Cutting tests were performed at two axial depths: 3 mm and 5 mm. In each case, a range of {spindle speed, radial depth} pairs were tested. Figure A.9 shows the predicted stability limit (•), as well as the stable (○) and unstable cuts (×). Good agreement between the predicted limit and experimental results is observed for both the process damping regime (<1000 rpm) and higher cutting speeds. Figures A.10–A.13 show the accelerometer frequency content at the test points labeled A through D in Figure A.9, respectively. Figure A.11 and A.13 demonstrate unstable cutting conditions (points B and D in Figure A.9); significant content is seen near the flexure's natural frequency of 247.2 Hz in addition to the tooth passing frequency and its harmonics. Figure A.10 and A.12 identify stable cuts with content at the tooth passing frequency and its harmonics only (points A and C).

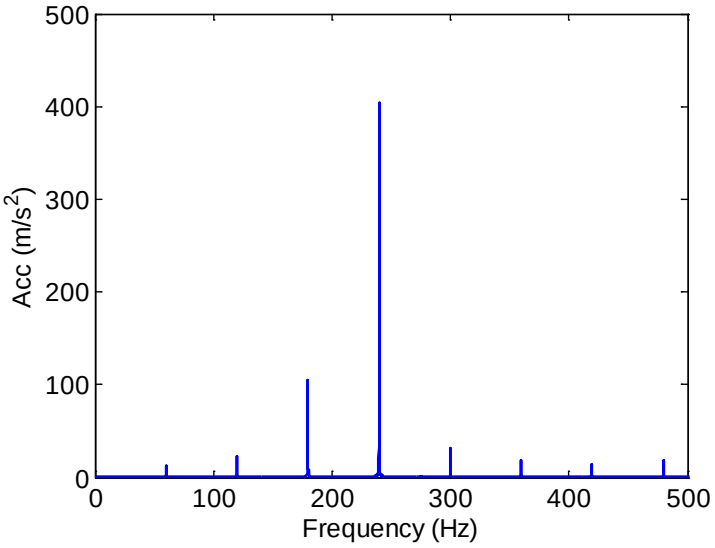

Figure A.10: Frequency content for a stable cut at a spindle speed of 3600 rpm, a radial depth of 5 mm, and an axial depth of 3 mm.

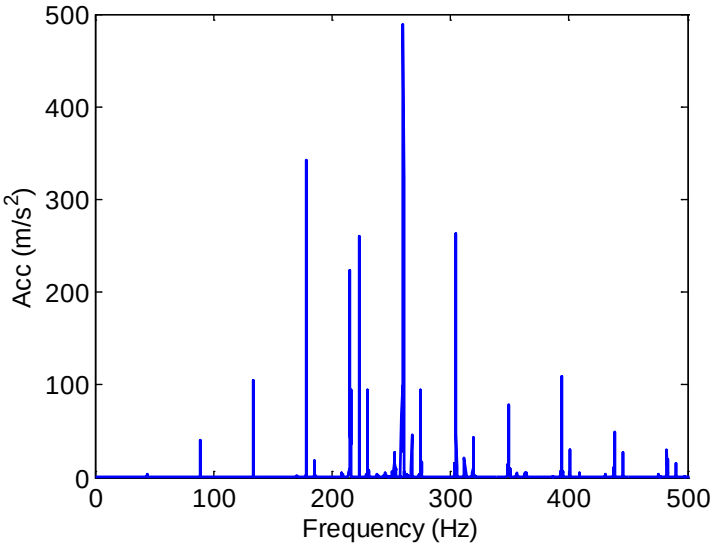

Figure A.11: Frequency content for an unstable cut at a spindle speed of 2675 rpm, a radial depth of 4 mm, and an axial depth of 3 mm.

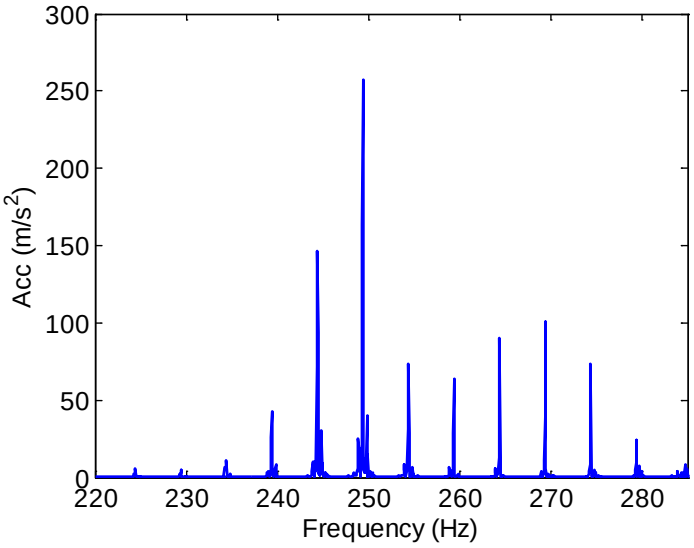

Figure A.12: Frequency content for a stable cut at a spindle speed of 300 rpm, a radial depth of 10 mm, and an axial depth of 3 mm.

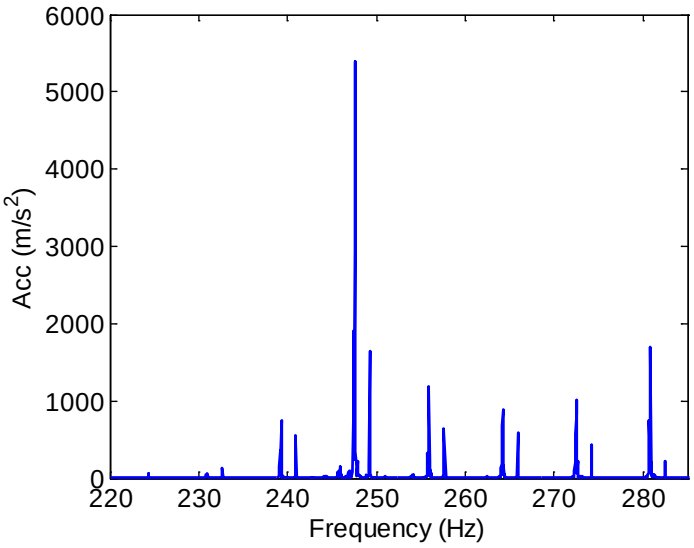

Figure A.13: Frequency content for an unstable cut at a spindle speed of 500 rpm, a radial depth of 10 mm, and an axial depth of 3 mm. Note the change in vertical scale relative to Figures A.10-A.12.

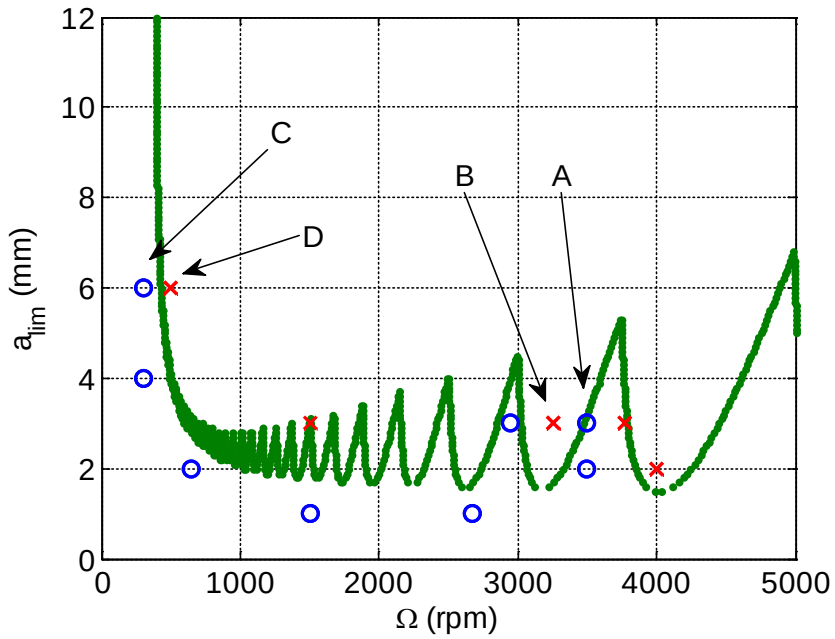

Figure A.14: Limiting radial depth of cut versus spindle speed for the flexure setup with a 5 mm axial depth.

Figure A.14 displays the predicted stability limit and experimental results for an axial depth of 5 mm. The increase in axial depth yields a decrease in the allowable radial depth relative to Figure A.9 (3 mm axial depth). Good agreement is again observed between the prediction and experimental results. Figures A.15 and A.18 show the frequency content for the points labeled A through D in Figure A.14. Points A and C (Figures A.15 and A.17) represent stable cuts, while points B and D (Figures A.16 and A.18) represent unstable cuts.

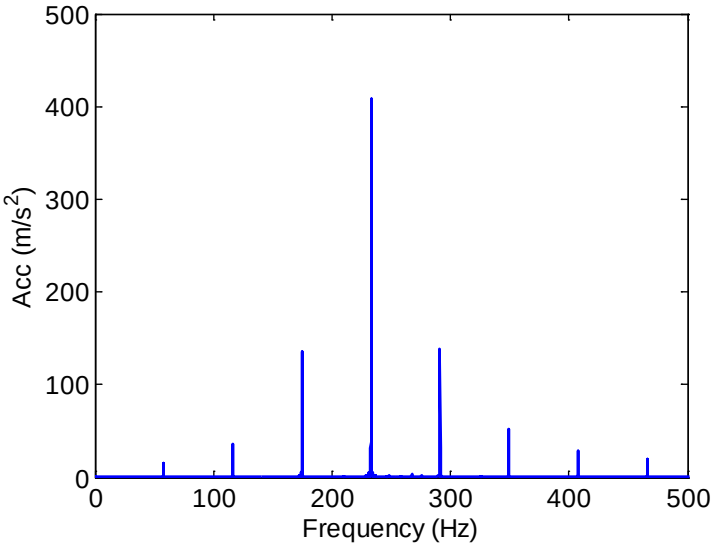

Figure A.15: Frequency content for a stable cut at a spindle speed of 3500 rpm, a radial depth of 3 mm, and an axial depth of 5 mm.

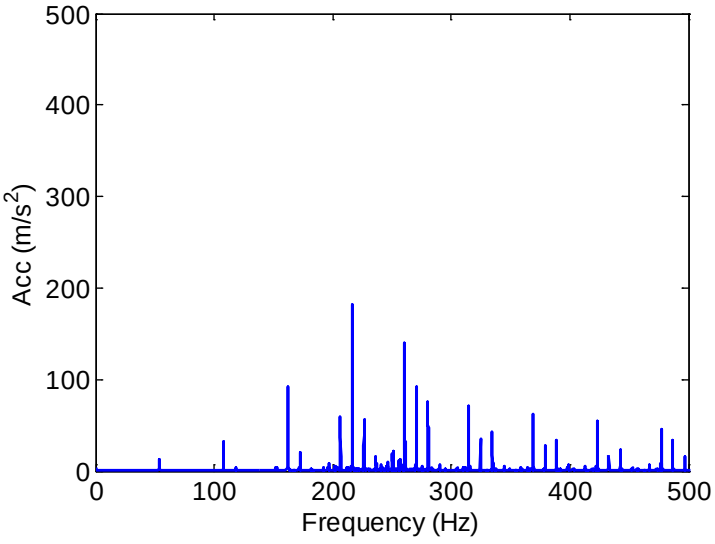

Figure A.16: Frequency content for an unstable cut at a spindle speed of 3250 rpm, a radial depth of 3 mm, and an axial depth of 3 mm.

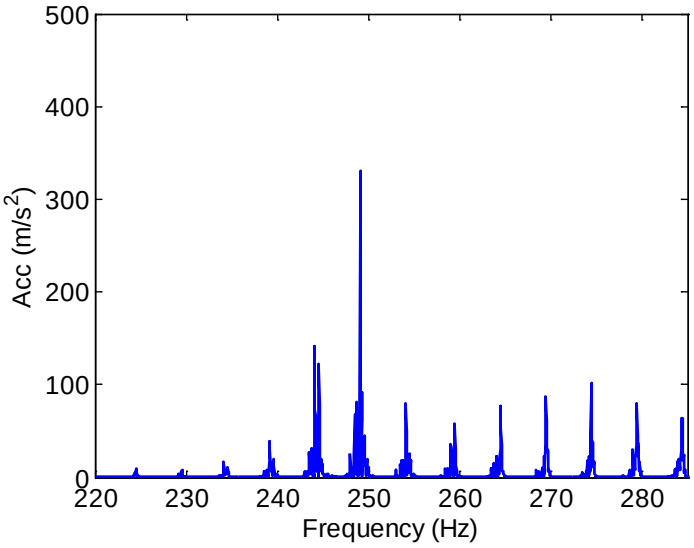

Figure A.17: Frequency content for a stable cut at a spindle speed of 300 rpm, a radial depth of 6 mm, and an axial depth of 5 mm.

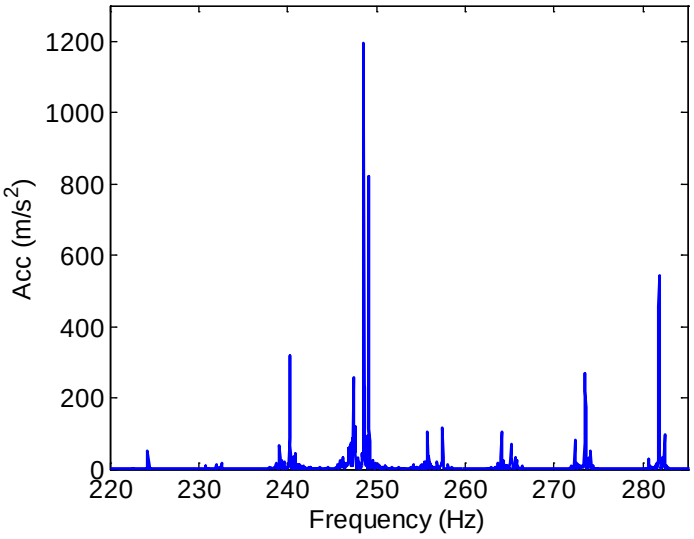

Figure A.18: Frequency content for an unstable cut at a spindle speed of 500 rpm, a radial depth of 6 mm, and an axial depth of 5 mm. Note the change in vertical scale relative to Figs. A.15-A.17.

A.3: Radial Immersion Tests Conclusions

Radial depth of cut stability lobe diagrams were produced and verified experimentally. The motivation for describing the stability limit as radial, rather than axial, depth is the format for many CAM programs, which remove material layer-by-layer with a varying radial immersion. The analytical milling stability solution applied to identify the stability lobe diagrams included process damping, where the process damping model relied on a single coefficient, C. This is analogous to the specific cutting force, K_s, approach to modeling cutting force. Process damping is particularly important for hard-to-machine materials, such as titanium, nickel super alloys, and hardened steels. In these instances, tool wear generally prohibits higher surface speeds and the use of the large stable zones available at high spindle speeds.

APPENDIX B: SUPPLEMENTARY PROCESS DAMPING MODEL

A supplementary parameter is proposed that enables the traditional analytical stability model to be augmented to incorporate the process damping stability increase observed at low cutting speeds.

As described previously, process damping can be described as an interference phenomenon between the relief face of the tool and the machined surface. As the wavelength of the surface undulations decreases for a fixed amplitude, the likelihood of energy dissipation through this interference increases. Therefore, the process damping phenomenon can be modeled as a function of a parameter which is analogous to the vibration wavelength, where a shorter 'wavelength' gives increased stability. In this study, the functional form:

$$\Lambda = b_{\mathrm{lim,cr}} e^{1/(\Omega\lambda)^2} \tag{75}$$

was selected, where Λ defines the process damping behavior, b_{cr} is the critical (asymptotic) stability limit from the traditional stability analysis, Ω, the spindle speed, is expressed in rpm, and λ is the supplementary process damping parameter (in m). Note that Λ takes the units of $b_{\mathrm{lim,cr}}$. Figure B.1 shows the process damping stability limit and Λ for 50% radial immersion, 15° relief angle, low wear up milling tests in 1018 steel ($C = 1.25\times10^5$ N/m, $\lambda = 2.2\times10^{-3}$ m). For the traditional stability analysis that does not include process damping, λ could be superimposed on the stability limit to identify the new, low cutting speed stability boundary. Each λ was selected based on the minimum residual sum of squares (RSS) between the $b_{\mathrm{lim,cr}}$ curve that includes process damping and Λ.

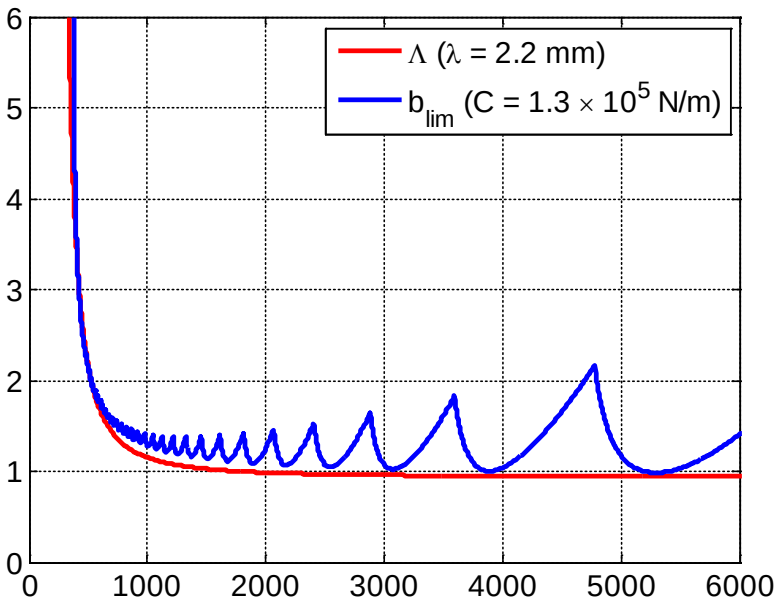

Figure B.1: Stability boundary for 50% radial immersion, 15° relief angle, low wear up milling tests in 1018 steel (C = 1.3×10^5 N/m) with multiplier, Λ (λ = 2.2×10^{-3} m).

An equivalent process damping parameter, λ, can be identified for each of the process damping coefficients identified in the process model database, as shown in Table B.1andTable B.2. It has been demonstrated that the process damping coefficient, C, is relatively insensitive to changes in dynamics. To ascertain whether this equivalent process damping parameter, λ, shares the same characteristics, a series of virtual experiments were conducted to observe any variability in λ as the dynamics of the cutting system are changed.

Table B.1: Process damping parameters, λ, for the 11° relief angle tool geometry.

	Process damping parameter, λ (mm)	
Material	Low insert wear (FWW < 0.100 μm)	Moderate insert wear (0.150 μm < FWW < 0.250 μm)
1018 Steel	1.8	1.5
Ti 6Al-4V	1.0	0.86
304 SS	0.47	0.44
Inconel 718	2.2	2.0
6061 Al	1.5	N/A

Table B.2: Process damping parameters, λ, for the 15° relief angle tool geometry.

	Process damping pavelength, λ (mm)	
Material	Low insert wear (FWW < 0.100 μm)	Moderate insert wear (0.150 μm < FWW < 0.250 μm)
1018 Steel	2.2	1.9
Ti 6Al-4V	1.5	1.0
304 SS	0.62	0.55
Inconel 718	2.5	2.2

The process begins with the modal and force parameters determined for cutting AISI 1018 steel on the parallel leaf-type flexure. The parameters for obtaining the stability boundary are provided in Table B. 3: Process parameters for determining process damping parameter, λ, sensitivity. Each study was performed using a single tooth ($N_t = 1$) and 50% radial immersion up milling operation.

Table B. 3: Process parameters for determining process damping parameter, λ, sensitivity.

k (N/m)	f_n (Hz)	ζ (%)	K_s (N/mm^2)	β (deg)	C (N/m)
2.77×10^6	229	6.3	2359.1	63.5	1.3×10^5

The sensitivity of the process damping parameter, λ, was evaluated by selectively changing one of the modal parameters over a range of values while the other remained unchanged. The variables and range over which they were changed are provided in Table

B.4. The following will discuss the trends and effects changing each modal parameter has on λ.

Table B.4: Range of modal parameters for λ sensitivity study.

Modal parameter	Minimum	Maximum	Step size
k (N/m)	1.0×10^6	4.0×10^6	0.1×10^6
f_n (Hz)	100	900	25
ζ (%)	1.5	7.0	0.5

While keeping all parameters constant, the value of λ was calculated while varying the modal stiffness, k, over the range of values specified in Table B.4 and the values of λ that which best fit the stability boundaries are plotted versus the modal stiffness. From Figure B.2, there is no apparent trend as the stiffness of the system is changed over a relatively large range of values.

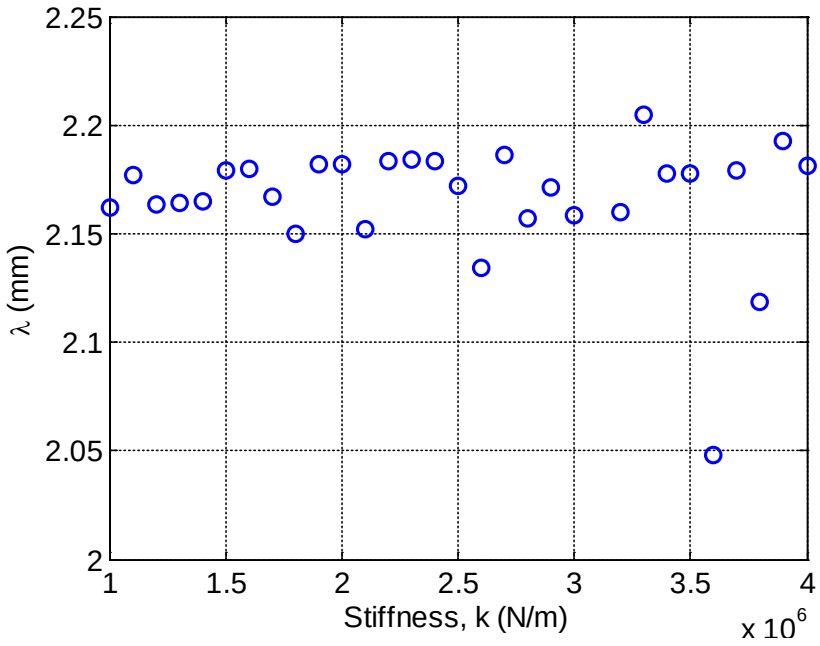

Figure B.2: Change in λ as a function of modal stiffness, k.

The process was repeated for the natural frequency (f_n) values specified in Table B.4. Here, a strong power law trend in λ is observed for increasing values of f_n as shown in Figure B.3. The trend follows the expression: $\lambda(f_n) = a(f_n)^b$, where a = 544 and b = -1.017 with R^2 = 0.99. To illustrate this effect, Figure B.4 and Figure B.5 represent the stability boundaries for the highest and lowest natural frequency values. It is observed that, as the system's natural frequency increases, the stability lobes shift toward the right and increasing spindle speed. With the same process damping coefficient, C, value, the process damping regime to the left of the stability boundary increases. This, in turn, leads to decreased values of λ which best fit the boundary.

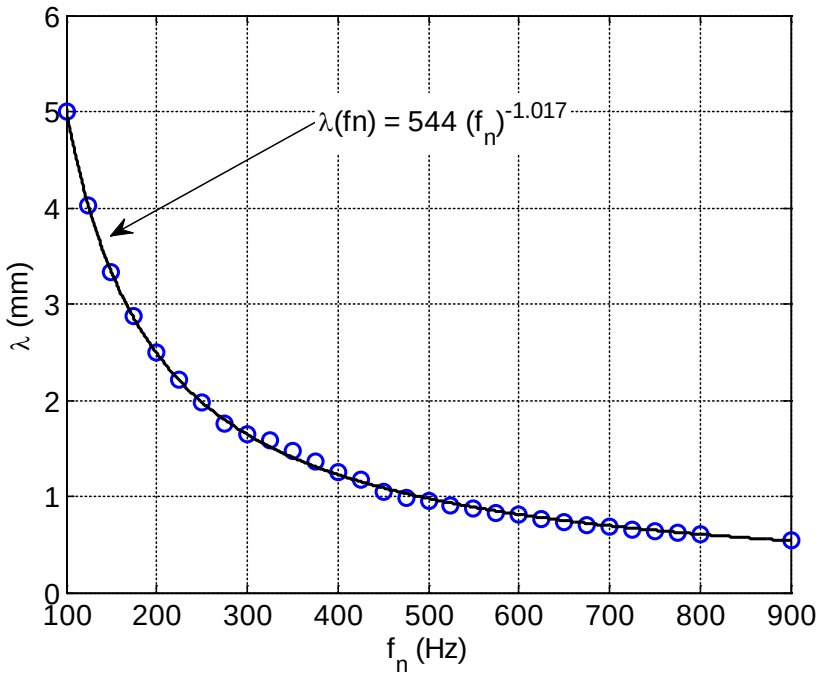

,

Figure B.3: Trend in λ as a function of natural frequency f_n.

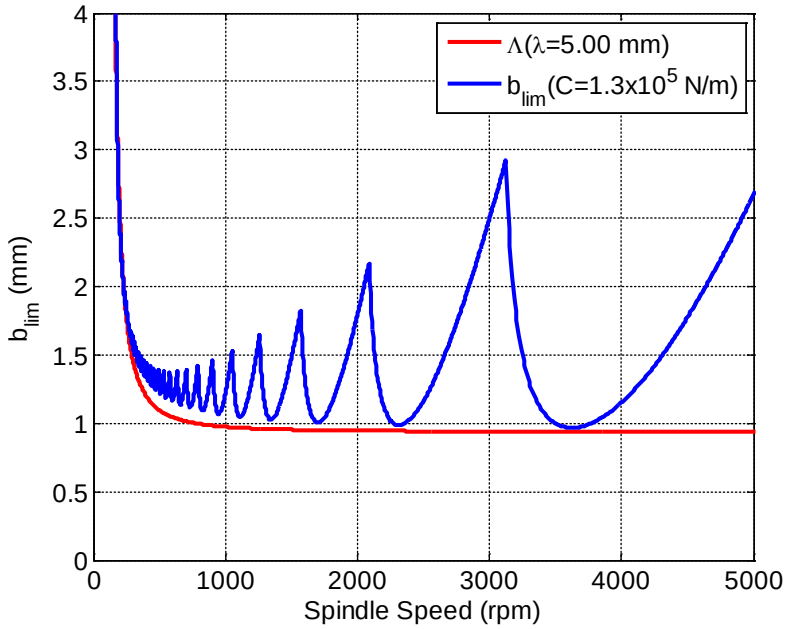

Figure B.4: Initial Stability boundary for 50% radial immersion, milling for 1018 steel (C = 1.3×10^5 N/m) with multiplier, Λ (λ = 5.00×10^{-3} m) and f_n = 100 Hz.

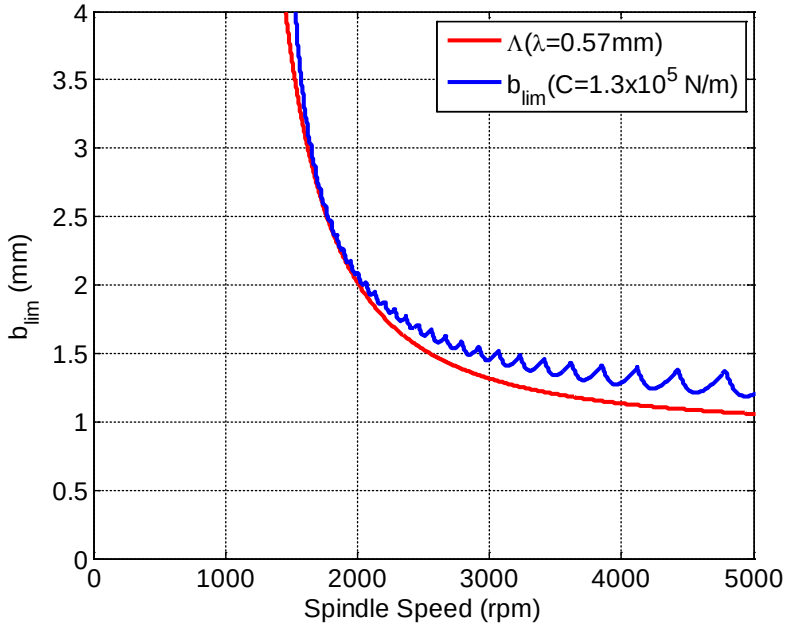

Figure B.5: Final Stability boundary for 50% radial immersion, milling for 1018 steel (C = 1.3×10^5 N/m) with multiplier, Λ (λ = 0.57×10^{-3} m) and f_n = 900 Hz.

In [2], Tlusty analyzes the process damping effect with a plot of b_{lim} versus cutting velocity for mild carbon steels for varying natural frequency systems. In Figure B.6, the process damping effect is shown to increase with increase in the system's natural frequency. As a comparison, the augmented Λ stability boundary is plotted versus the cutting velocity in Figure B.7 for the range of natural frequencies tested. In general, the trend of increasing process damping with increase in natural frequency is consistent. Recall, that each of the boundaries shown are captured with the same process damping coefficient, *C*.

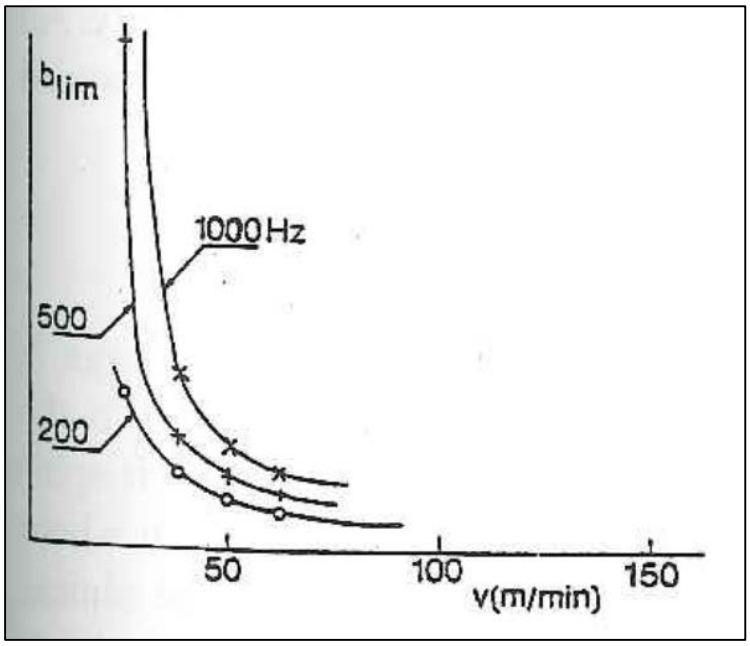

Figure B.6: Low cutting speed process damping effects with varying system natural frequency for mild steel, Tlusty [2].

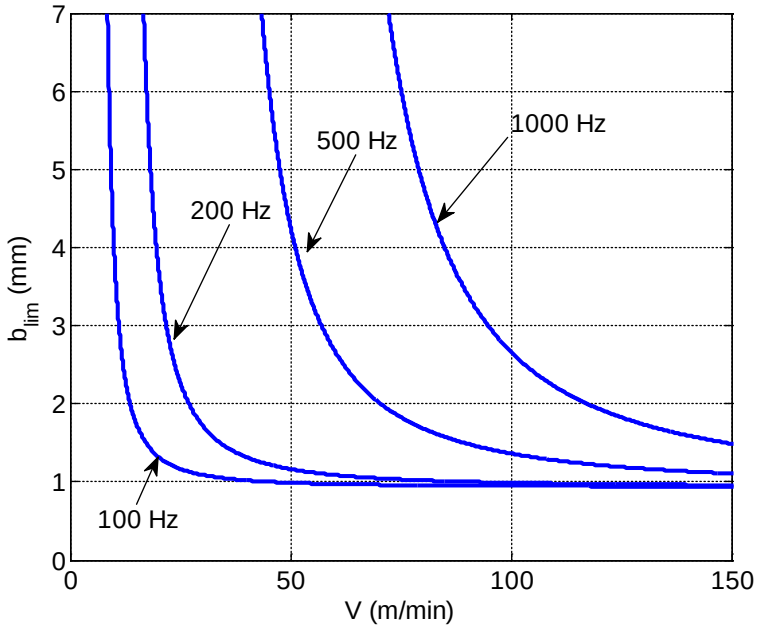

Figure B.7: Augmented stability boundary b_{lim} (mm) versus V (m/min) for f_n = 100, 200, 500, and 1000 Hz.

Finally, the damping ratio was varied while the modal stiffness and natural frequency were returned to the original values in Table B.3. As shown in Figure B.7, there is a strong linear decrease in λ as ζ is increased from 1% to 7%. The linear trend follows the expression: $\lambda(\zeta) = a\zeta + b$, where a = -6.61 (mm) and b = 2.59 (mm) with R^2 = 0.98. It should be noted that, when increasing the system's natural frequency, the decrease in λ was nearly 90% of the original value, while the percent change in λ that is observed when increasing the damping ratio is only approximately 15%. It may then be concluded that changes in the system's natural frequency have a predominant effect when determining the equivalent process damping parameter, λ.

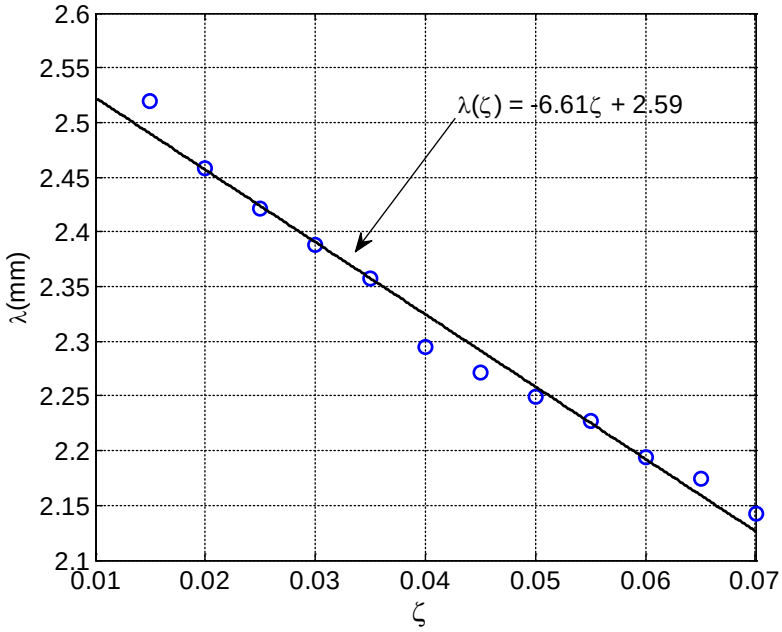

Figure B.8: Trend in λ as a function of damping ratio, ζ.